Simulations of an active-target TPC for a measurement of the proton charge radius

Fabian Metzger

Masterarbeit in Physik
angefertigt im Helmholtz-Institut für Strahlen- und Kernphysik

vorgelegt der
Mathematisch-Naturwissenschaftlichen Fakultät
der
Rheinischen Friedrich-Wilhelms-Universität
Bonn

November 2020

I hereby declare that this thesis was formulated by myself and that no sources or tools other than those cited were used.

Bonn, ...

Date Signature

1. Gutachter: Prof. Dr. Bernhard Ketzer
2. Gutachter: Prof. Dr. Sebastian Neubert

Acknowledgements

First and foremost, I would like to thank my supervisor Prof. Bernhard Ketzer that I was able to write this thesis. It was a great experience to work in an experimental environment like the COMPASS-experiment. He always supported and helped me to solve every problem that has occurred during that time. I really enjoyed the discussions during the regular group meetings. They always made sure that everything can progress. Thank you for your support concerning the BCGS and CERN's Gentner program.
Furthermore I would like to thank Prof. Sebastian Neubert that he took the time to do the second review of my thesis. The discussions about my thesis have been very helpful.
Special thanks to the whole AG Ketzer for the nice time, not only during my Master, but also during my Bachelor thesis. Thank you Philip for all your help concerning Garfield++, and thank you Philipp for being the Geant4-support and proofreading. Together with Karl, the times in the office have been great fun. Thank you Dima for your great support and for proofreading.
At this point I would like to say thank you to Martin who always helped me during that time. Thanks for all the fruitful discussions and your support. Every time there have been problems you helped me to solve them.
Finally, I would like to thank my whole family, my parents and siblings. I know that I can always count on you. You supported me, not only during my university studies, but also during my school time. I want to dedicate this work to all of you. I am really thankful for having you.

Contents

CHAPTER 1

Introduction

The world around us and we are made out of matter consisting of atoms and molecules. A fairly long time ago atoms were known as elementary particles. One assumed that they have no further substructure leading to the name atom (from the Greek work $\alpha\tau o\mu o\varsigma$; that means indivisible). At the end of the 19$^{\text{th}}$- and during the 20$^{\text{th}}$-century the level of knowledge and therefore the technologies constantly improved resulting in the discovery of constituents of the atom: electrons, neutrons and protons.

The proton was discovered by Ernest Rutherford in 1919 [1]. In his experiment he scattered α-particles on air, so mainly nitrogen and counted the number of scintillations depending on the distance. In a distance that is much bigger than the range of α-particles in air, he observed scintillations. Those could be traced back to the scattering on by hydrogen-nuclei, i.e. protons which are created in the reaction

$$^{14}\mathrm{N} + {}^{4}\mathrm{He} \rightarrow {}^{17}\mathrm{O} + \mathrm{p}\,.$$

The first evidence that even the proton is not a point-like particle was found in 1933 by Otto Frisch and Otto Stern [2]. If a particle is point-like and has spin $\frac{1}{2}$ it should have a g-factor (g is proportional to the magnetic moment) of $g \approx 2$. But they found out that a proton has a magnetic moment in the order of 2 to 3 nuclear magnetons what corresponds to a g-factor between 4 and 6.
Today it is known that the proton is made out of quarks which are bound by the strong force. These quarks are assumed to be fundamental meaning that they are point-like particles within the Standard Model of Particle Physics. In the quark-model the proton consists of two up-quarks and a down quark with charges $z_{\mathrm{u}} = \frac{2}{3}e$ and $z_{\mathrm{d}} = -\frac{1}{3}e$ respectively. All these findings lead to huge efforts initiated by Hofstadter et al. [3]. The size of the proton is of general interest itself as the it is a fundamental particle to describe atoms and their nuclei and the whole universe. But there are as well models using its size as input. One is able, for example, to probe the strong interaction in its non-perturbative energy regime. The size, i.e. the spatial extent of the proton, depends on the charge distribution inside of it and is called the **proton charge-radius**.

The proton charge-radius has been extracted by many experiments conducting elastic electron-proton

scattering. These lead to a 2014-CODATA-value of (0.8751 ± 0.0061) fm [4][1].
Another approach beside scattering is spectroscopy of hydrogen, muonic or ordinary, looking at the *Lamb*-shift. Experiments with electronic hydrogen yield a 2014-CODATA-result of (0.8759 ± 0.0077) fm [4] that is in good agreement with the results from electron-proton scattering. Instead of standard hydrogen one can also use spectroscopy with muonic hydrogen. Because of the higher mass of muons compared to electrons, muonic hydrogen is more sensitive to the finite size of the proton[2]. An experiment in 2010 by the CREMA collaboration resulted in a proton charge-radius of (0.84184 ± 0.00067) fm [6]. In 2013 they extracted a value of (0.84087 ± 0.00039) fm [5] with a new measurement. The huge discrepancy between for example the result from CREMA [6] and the values of spectroscopy of ordinary hydrogen and elastic electron scattering of about 5σ became famous and is nowadays known as the **proton radius puzzle**. The comparison of the proton charge-radius extracted from different experiments including both scattering and spectroscopy is shown in figure 1.1. At this point one needs to emphasize the theoretical work from the last years. The electron-proton scattering data can be analyzed with the help of dispersion relations using fundamental principles like unitarity and crossing. These analyses led to significantly smaller proton charge-radius of (0.840 ± 0.005) fm which is compatible with the results from the spectroscopy of muonic hydrogen [7, 8].

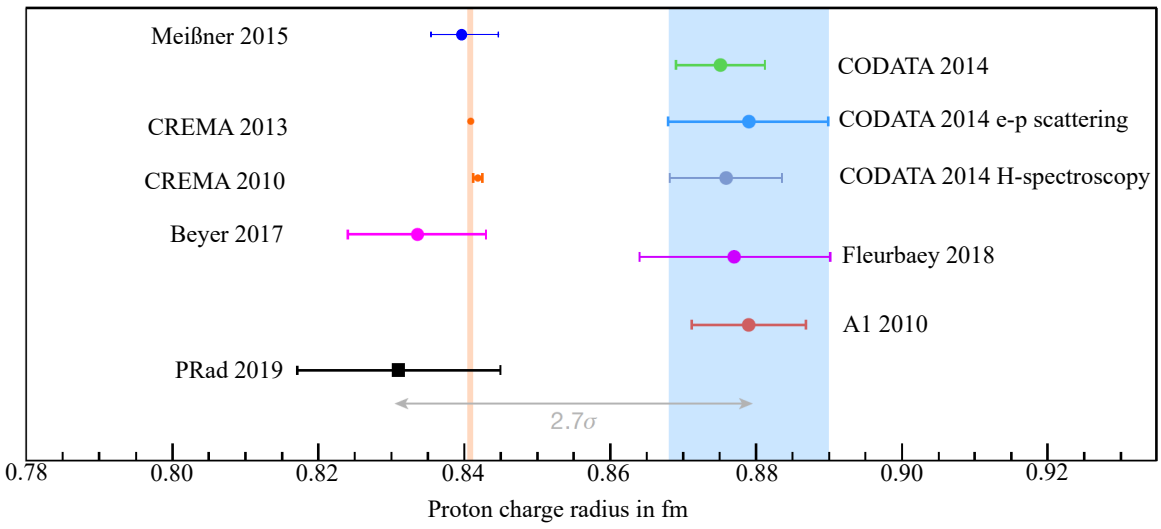

Figure 1.1: Results of different experiments for the proton charge-radius. Taken from [9], modified. The result of Meißner et al. is taken from [7].

The newest result from electron-proton scattering is from the PRad experiment at Jefferson Lab in the US. They collected data in 2016 and published a proton charge-radius of (0.831 ± 0.014) fm in 2019 [9][3]. They measured the scattering cross-section with an electron beam with energies of

[1] The way how the radius is extracted out of the data is explained in chapter 2.

[2] S-waves have a finite probability to be at the position of the atomic nucleus. This probability (the square of the wave-function) depends on the reduced mass of the system which is larger by a factor of approximately 186 in the case of muonic hydrogen. Therefore, the Bohr radius yielding the order of magnitude of the atomic size is smaller by this factor. Because of that the achieved precision with spectroscopy of muonic hydrogen is further improved compared to ordinary hydrogen [5].

[3] The stated systematic and statistical errors are added in quadrature.

1.1 GeV and 2.2 GeV down to momentum transfers[4] of $2 \times 10^{-4}\,\mathrm{GeV}^2\,c^{-2}$. Measuring down to such low momentum transfers and therefore such low scattering angles is possible because they made use of a windowless hydrogen gas flow-target and did not deploy a magnetic spectrometer [10].

The COMPASS++/AMBER-collaboration proposes a different ansatz of scattering experiments to challenge the proton radius puzzle. Up to now only electron-proton-scattering has been conducted. But the comparison between ordinary and muonic hydrogen has been done. Therefore, it is proposed to do elastic muon-proton-scattering in a low momentum-transfer region that is quite sensitive to the size of the proton in 2022/23 [11]. A pressurized hydrogen *Time Projection Chamber* (TPC) as active target to detect low energetic recoil protons will be used for elastic scattering of muons with momenta of $100\,\mathrm{GeV}\,c^{-1}$. The elastic scattering cross-section is planned to be measured in the negative squared momentum transfer range of 0.001 to $0.04\,\mathrm{GeV}^2\,c^{-2}$ with the possibility to extend it to larger values. By measuring the kinematics of the proton one is able to calculate the momentum transfer. For values lower than $0.02\,\mathrm{GeV}^2\,c^{-2}$ the recoil proton energy is directly measured by measuring the deposited energy in the gas (the protons are stopped in the gas at these energies). For larger energies with which the protons can escape the TPC one makes use of the energy calculation with the so-called $\frac{\mathrm{d}E}{\mathrm{d}x}$-method. A drawback of the ansatz with an active target and the muon beam is that the muons do not only scatter elastically with protons but they undergo also energy-loss processes leading to a large background in the TPC. This noise makes it difficult to detect low energetic protons especially as the muon beam is quite broad. With the COMPASS spectrometer the beam muons can be detected and the muon that has scattered on the proton can be identified and matched with it. Hence the scattering process can be compared to the results from the TPC. This is necessary to overconstrain the reaction. Using this, one can control the background and most importantly one can select elastic scattering events. It is aimed to determine the proton charge-radius with a statistical precision below 1 %.

A similar approach is foreseen by the A1-collaboration at MAMI [12] with a 720 MeV electron beam. One will use a comparable active-target TPC measuring the cross-section over the same momentum transfer range as at COMPASS++/AMBER. The advantage of the electron beam is that it is quite narrow having a small energy spread. Therefore the background generated by the beam itself is focused onto the central ring. The similarity to the COMPASS++/AMBER-approach will make it possible to use the energy-range-calibration of the Mainz experiment to extract the momentum transferred from the muon to the proton.
The Paul-Scherrer-Institute located in Switzerland proposes the scattering experiment MUSE [13]. They want to perform scattering of electrons, positrons, muons and anti-muons on protons with beam momenta in the range of 115 to $210\,\mathrm{MeV}\,c^{-1}$. With this experiment one can study the influence of the different leptons. One possible explanation of the proton radius puzzle is the violation of lepton universality[5]. This argument can be probed by comparing the electron-proton and muon-proton elastic scattering results. Compared to the proposed high-energy muon-proton scattering at COMPASS++/AMBER one needs to deal with different systematic uncertainties. At such low muon energies one has, for example, a large influence of multiple scattering leading to larger scattering

[4] The connection between momentum transfer, the elastic scattering cross-section and the proton charge-radius will be explained in chapter 2.

[5] Electrons, muons and tauons should all behave in the same way according to the Standard Model of Particle Physics. They only differ in their mass.

angles that can be resolved. In general, Coulomb-distortions created by the electric field of the target atoms need to be taken into account as well as the wave functions of the incoming and scattered particles are modified. In the case of the electron-proton scattering at PSI, but of course at MAMI as well, one has to deal with radiative corrections because of the low electron mass compared to muons. All these effects are of minor interest in the case of high-energy muon-proton scattering.

The main subject of this thesis is the simulation of the response of the TPC to optimize its read-out geometry in terms of energy resolution and proton reconstruction.
First, a brief introduction into the elastic scattering of muons and protons is given in chapter 2 defining the proton charge-radius as well as the basic concepts to extract it from measured data.
As the detector of interest for this work and the main one for the measurement is the TPC it is necessary to understand its principles. Energy deposition in the active material and the drift of the created charges generate the signals induced in the read-out electrodes. In section 3.1 the energy loss of charged particles in matter with focus on energy loss fluctuations is described. In the following part 3.2 the drift and diffusion of charges created by the energy loss of the traversing particle is discussed. After that the principle of signal induction and generation is introduced in section 3.3 by means of the *Shockley-Ramo*-theorem and *weighting field*.
In chapter 4 the experimental environment as it will be at CERN in 2022/23 is described with focus on the main detector components of the setup.
The basic principles of the TPC are discussed in chapter 5. The layout of the proposed detector is described and the main parameters like electron drift velocity and diffusion are determined. These are used as an input for further simulations.
The basis for simulations of a detector like a TPC is the energy loss by particles traversing it. In chapter 6 special attention is payed to the *photo-absorption-ionization*-model to described the energy loss. This is then compared to the implemented energy loss processes that are used in the following.
Another input needed for the simulation of the detector response is the response pad read-out of the TPC itself. In chapter 7 the calculation of the electric and weighting fields is explained in terms of a finite-element method that is implemented in the framework of ANSYS ®. To extract the pad responses a framework based on GARFIELD++ is developed. The outcome of this framework is used then for the simulations of the whole TPC as described in chapter 8. Here, at first the simulation chain is explained (cf. section 8.1). In addition to the above described background originated by the broad muon beam, the read-out electronics themselves are sources of noise as well. This electronic noise is extracted based on data taken during a test run in 2018. The signal generation from charge creation over electron drift to signal induction inside the TPC is then simulated. Therefore different anode geometries with their response functions are implemented within the GEANT4-based framework TGEANT that has detector elements of the COMPASS++/AMBER-setup implemented. For different momentum transfers the output of the TPC including the broad muon background and the elastically scattered protons is analyzed in terms of energy resolution and track reconstruction.
In chapter 9 the results from the simulations described in chapter 8 are analyzed. The behaviour of the pad planes is determined for the most important criteria, which are on the one hand the energy resolution and on the other hand the angular resolution.

CHAPTER 2

Measurement of the proton charge-radius

There are two ways to extract the charge-radius of the proton: scattering on and spectroscopy of hydrogen. In a scattering experiment one only considers elastic scattering, so that the proton is not in an excited state. The advantage of elastic scattering is that the experimentalist only needs to know one kinetic variable as for example the scattering angle. From this, one is able to calculate the whole kinematics. In the experiment itself one needs to measure the cross-section of the elastic scattering process to extract the proton charge-radius. For further information refer to [14].

The relativistic invariant cross-section for scattering of fermions on a target without spin is the so-called Mott cross-section (2.1) [15],

$$\left(\frac{\mathrm{d}\sigma}{\mathrm{d}\Omega}\right)_{\mathrm{Mott}} = \left(\frac{2E'\alpha\hbar c}{q^2c^2}\right)^2 \frac{E'}{E}\left(1-\beta^2\sin^2\left(\frac{\theta}{2}\right)\right), \tag{2.1}$$

where E is the energy of the incoming and E' the energy of the outgoing fermions, $q^2 = (p_\mathrm{f} - p_{\mathrm{f}'})^2$ denotes the squared four-momentum transfer of the reaction (p_f and $p_{\mathrm{f}'}$ are the four-momentum vectors of the incoming and outgoing fermions) and θ represents the scattering angle between the incoming and outgoing fermion (cf. figure 2.1). The factor $\frac{E'}{E}$ takes care of the target recoil. α is the electromagnetic fine-structure constant, $\hbar$ the reduced Planck's constant, c the speed of light and β the velocity of the projectile in units of c.
Since the target consists of protons which are half-spin particles one needs to take the spin of $\frac{1}{2}$ into account leading to the Rosenbluth cross-section (2.2) [16],

$$\left(\frac{\mathrm{d}\sigma}{\mathrm{d}\Omega}\right)_{\mathrm{Rosenbluth}} = \left(\frac{\mathrm{d}\sigma}{\mathrm{d}\Omega}\right)_{\mathrm{Mott}}\left(\frac{G_\mathrm{E}^2\left(Q^2\right)+\tau G_\mathrm{M}^2\left(Q^2\right)}{1+\tau} + 2\tau G_\mathrm{M}^2\left(Q^2\right)\tan^2\left(\frac{\theta}{2}\right)\right), \tag{2.2}$$

with $Q^2 = -q^2$ and $\tau = \frac{Q^2}{4m_\mathrm{p}^2c^2}$ with m_p being the mass of the proton. G_E and G_M denote the electric and magnetic form-factors of the proton respectively.
To extract the charge-radius of the proton the dependence of the electric form factor G_E on the momentum transfer Q^2 as shown in equation (2.4) is required.
Measurements from scattering experiments imply that the form-factors of the proton follow a dipole-like

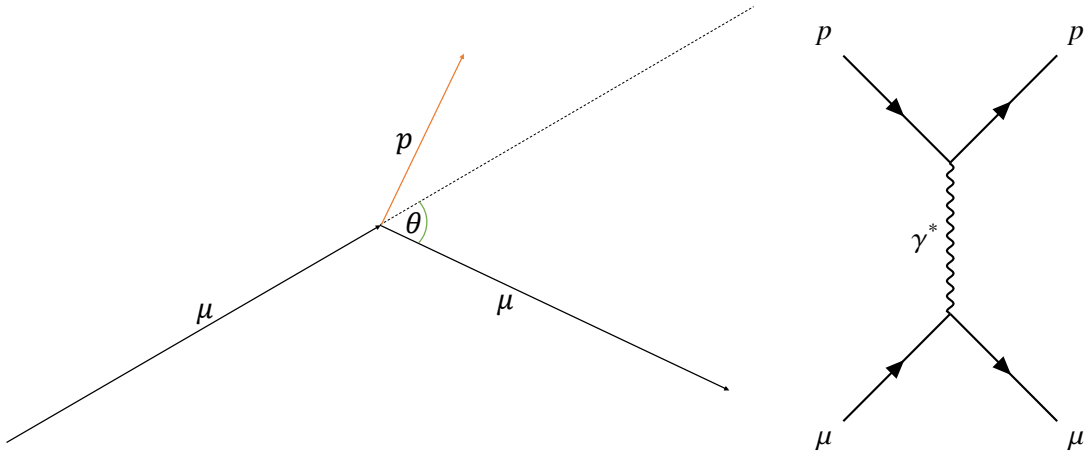

(a) Definition of the scattering angle θ. The angles are not representative for high-energetic muons.

(b) Feynman diagram of the scattering process.

Figure 2.1: Scattering of a muon and a proton.

shape as in equation (2.3) with the parameter a.

$$G^{p}_{\mathrm{E,\,M}}\left(Q^2\right) = G^{p}_{\mathrm{E,\,M}}\left(0\right)\left(1+\frac{Q^2}{a^2}\right)^{-2} \tag{2.3}$$

Such a dipole-like form-factor indicates an exponentially decreasing charge distribution inside the proton. The mean-square charge-radius can then be written as stated in equation (2.4),

$$\left\langle r_{\mathrm{p}}^2\right\rangle = -6\hbar^2\left.\frac{\mathrm{d}G_{\mathrm{E}}\left(Q^2\right)}{\mathrm{d}Q^2}\right|_{Q^2=0} \overset{\text{dipole}}{=} \frac{12\hbar^2}{a^2}\,. \tag{2.4}$$

The left-hand side of equation (2.4) results directly from the definition of the charge-radius. The right equality of (2.4) is only valid under the assumption of a dipole-like form-factor. For a typical value of $a^2 = 0.71\,\mathrm{GeV}^2\,c^{-2}$ one can deduce a radius of 0.811 fm.

The COMPASS++/AMBER-collaboration will follow an ansatz different from the typically used Rosenbluth-separation. The proton radius will be extracted directly from a fit of $\frac{\mathrm{d}\sigma}{\mathrm{d}Q^2}$ with the model-dependent form-factors [11, p. 12]. In the proposed Q^2-range of 0.001 to $0.04\,\mathrm{GeV}^2\,c^{-2}$ the influence of terms with the magnetic form-factor G_{M} is rather small coming from small values of τ in the order of 3 ‰. Because of this the electric form-factor G_{E} represents the main contribution of the elastic scattering cross-section. Different models for the form-factors will be examined to extract the proton charge-radius.

CHAPTER 3

Theoretical background

A particle that traverses a material can be detected by its interactions with it. By these interactions, the particle loses some amount of its energy and if this deposited energy is high enough the atoms in the material become ionized or displaced. The energy loss will be discussed in section 3.1.
The liberated charges can now move freely through the material and interact with the surrounding atoms and molecules. In the case of a particle detector, usually, there is mostly an electric field applied that defines the overall direction of the particle movement. Related to this, particle drift and diffusion are discussed in section 3.2.
To detect the moving charges, and therefore the particle itself, it is necessary to readout the signals induced by the free charges. The basic principle of signal creation is not the charge collection by some electrode itself, but the movement of charges relative to the electrode. By this movement an electric current is induced in the electrode. In section 3.3 it is described how the electric signal is generated with the help of the *Shockley-Ramo-theorem*.

3.1 Energy loss in matter

One topic of this thesis is the comparison of the energy loss of charged particles in matter simulated by different computer codes. The standard tool for the interactions of particles with matter is GEANT4 (**Ge**ometry **an**d **t**racking) [17]. It allows to choose different models that describe the interactions of the chosen particles with the implemented materials. One model that will be analyzed is the so-called PAI-model (**P**hoto-**A**bsorption-**I**onization-model) [18]. Another toolkit for the simulation of the energy loss of particles in matter, especially gases, is GARFIELD++ [19]. Here, one has an interface to HEED++ (**H**igh **E**nergy **E**lectro-**D**ynamics) [20] which is an implementation of the PAI-model.

3.1.1 Mean energy loss

If particles (in the following it is always assumed that they are charged) penetrate a medium, they interact with this medium. The most relevant interactions are excitation and ionization. In these and other processes, like bremsstrahlung, these particles transfer some amount of their energy to the atoms of the material they traverse. Both excitation and ionization are based on the electromagnetic interaction between the particle and target atom. In the case where the energy transfer is below the ionization threshold of the atom, it could still produce an excited state which will

de-excite afterwards, mostly through the emission of a photon. If the particle transfers enough energy to the atomic electrons, the atom will be ionized and ejects at least one shell electron. The electron(s) and the ion can then free further electrons from other atoms in the material. The first interaction is called primary ionization, while all the following ones are referred to as secondary ionizations.

To calculate the average energy loss one needs to know the differential cross-section of the interactions. In the given context, these interactions are mostly electromagnetic, such that one can use the Rutherford cross-section, or more precisely, the Mott cross-section in order to take the spins of the atomic electrons into account. The energy dependent form is given by

$$\frac{\mathrm{d}\sigma}{\mathrm{d}T} = \frac{2\pi}{m_\mathrm{e}} \left(\frac{z\alpha\hbar}{\beta T} \right)^2 \left(1 - \beta^2 \frac{T}{T_\mathrm{max}} \right) , \tag{3.1}$$

where z is the charge of the projectile in units of the elementary charge e, β its velocity in units of c, T the kinetic energy of the electron after the collision, m_e the electron mass and T_max the maximal kinetic energy that can be transferred to an shell electron in a single collision [21].
The mean energy loss can then be calculated by integrating the product of the differential cross-section (3.1) and the energy along the energy-axis. The mathematics can be found in [21]. The outcome is the so-called *linear-stopping-power*, better known as the Bethe-Bloch-equation (3.2) [22] shown in figures 3.1 and 3.2,

$$\left\langle -\frac{\mathrm{d}E}{\mathrm{d}x} \right\rangle = K z^2 \frac{Z}{A} \rho \frac{1}{\beta^2} \left[\frac{1}{2} \ln \left(\frac{2 m_\mathrm{e} c^2 \beta^2 \gamma^2 W_\mathrm{max}}{I^2} \right) - \beta^2 - \frac{\delta\left(\beta\gamma\right)}{2} \right] . \tag{3.2}$$

$K = 4\pi N_A r_\mathrm{e}^2 m_\mathrm{e} c^2 = 307.075\,\mathrm{keV\,mol^{-1}\,cm^2}$

$N_A = 6.022 \times 10^{23}\,\mathrm{mol^{-1}}$: Avogadro's number

$r_\mathrm{e} = \dfrac{e^2}{4\pi\epsilon_0 m_\mathrm{e} c^2} = 2.818\,\mathrm{fm}$: Classical electron radius

$m_\mathrm{e} = 510.999\,\mathrm{keV}\,c^{-2}$: Electron mass

$c = 299\,792\,458\,\mathrm{m\,s^{-1}}$: Speed of light

$\epsilon_0 = 8.854\,\mathrm{pF\,m^{-1}}$: Permittivity of free space

z : Charge of the incident particle

Z : Atomic number of the traversed medium

A : Mass number of the traversed medium

ρ : Density of the traversed medium

β : Velocity of the incident particle in units of c

γ : Lorentz factor of the incident particle

W_max : Maximal energy that can be transferred in a single collision

I : Mean excitation energy

$\delta\left(\beta\gamma\right)$: Density effect correction to ionization energy loss

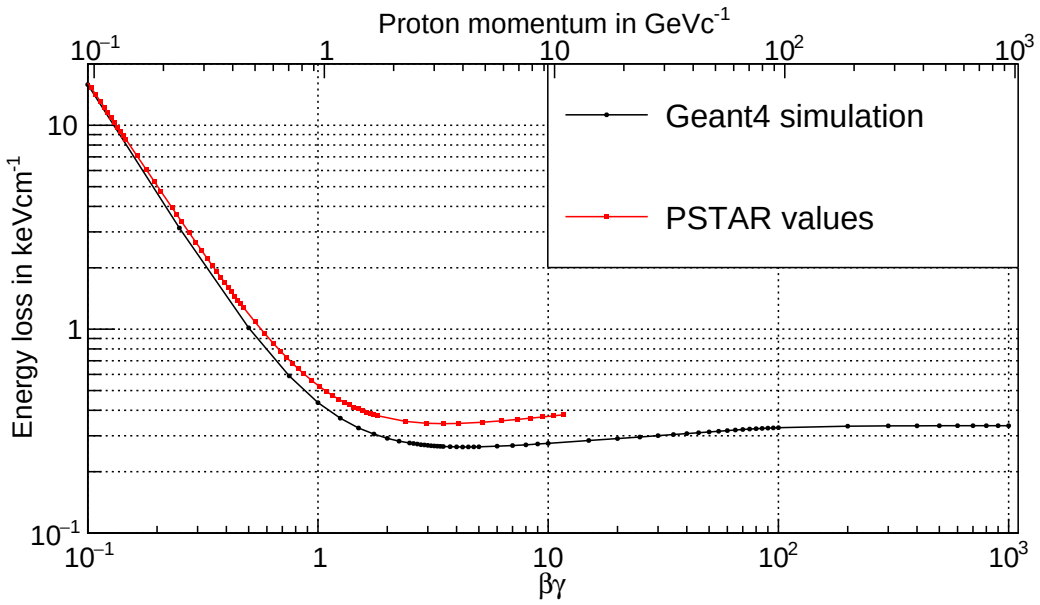

Figure 3.1: Average energy loss of protons in hydrogen gas at 1 bar. For the simulation in GEANT4 the *Livermore*-model has been used. The implemented sensitive material has a thickness of 2 cm. The PSTAR-values are taken from [23]. This is the $\beta\gamma$-range where the BETHE-BLOCH-equation is valid. The data points are connected by splines. The PSTAR-values are scaled with a density of $8.3748 \times 10^{-5}\,\mathrm{g\,cm^{-3}}$ [24]. PSTAR is a database describing the mean energy loss of protons in various media. The disagreement will be discussed in chapter 6.

The average energy loss calculated with (3.2) is valid for values of $\beta\gamma$ between 0.1 to 1 000. For higher momenta one needs to take radiation losses like bremsstrahlung into account. For lower momenta one reaches velocities of the atomic electrons. In this region one needs to do quantummechanical calculations taking into account the wave functions of the electrons. The BETHE-BLOCH-equation is also not valid for electron projectiles as they are indistinguishable from the target electrons and their energy loss is rather soon dominated by radiation losses because of their low mass. But in the regime, where one can apply (3.2), the amount of deposited energy per unit length is only determined by $\beta\gamma$, the charge of the traversing particle z and the medium itself.
For low energies, the energy loss is mostly dominated by the $\frac{1}{\beta^2}$-term[1], until it reaches a minimum at

$$\beta\gamma \approx 3\,.$$

A particle that fulfills this property is called *minimum ionizing particle*, or short MIP. The minimum is followed by the so-called relativistic rise. On the one hand this rise can be explained by the increase of the maximal energy transfer in a single collision, and on the other hand by an increase of the transverse electric field of the projectile caused by the relativistic length contraction. Because of the electric field, the material becomes polarized that will stop the increase of the energy loss at a certain point. This is taken into account by the density correction.

[1] The energy loss increases with decreasing velocity as the time, in which the projectile and target atom can interact, effectively increases.

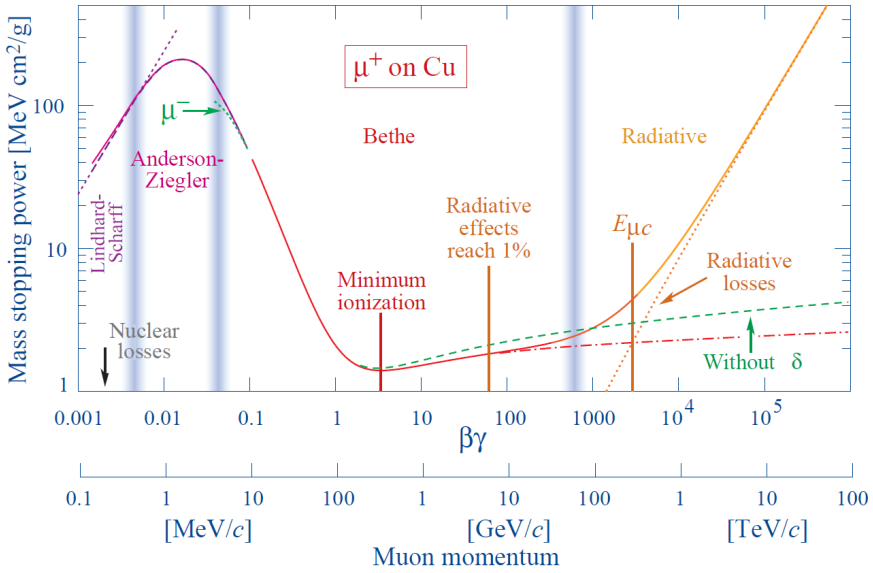

Figure 3.2: *Mass-stopping-power* of anti-muons in copper. Here, a larger range of $\beta\gamma$ is plotted, not only the BETHE-BLOCH-region. The plot is taken from [22, p. 447].

3.1.2 Energy-loss fluctuations

The BETHE-BLOCH-equation only gives rise to the average energy loss. But the energy loss of charged particles is a statistical quantity as the underlying physical processes have a discrete nature. Because of that, one observes different energy losses even though the incident particles are of the same species and have the same energy. Therefore, one has to deal with the underlying probability density function PDF better known as the *straggling function*.
The *straggling function* is a very asymmetric distribution (cf. figure 3.3) and can be approximated to first order by a LANDAU distribution[2]. The asymmetric behaviour has its origin in collisions in which a large amount of energy is transferred to the target atoms and so-called δ-electrons (or high-energetic knock-on electrons; their kinetic energy is typically in the order of keV) are liberated. Because of the disagreement in the high-energy regime it is more meaningful to deal with the maximum of the PDF than regarding the average value. This value is called *most probable value*, in the following referred to as the MPV. In addition to the MPV, the width of the distribution, typically the so-called *full-width at half maximum* FWHM is used to describe the *straggling function*.
A model that is widely used to describe energy loss and straggling is the previously mentioned PAI-model developed by Allison and Cobb [18]. This model uses measurements of the photo-absorption cross-section in various polarizable materials (with electron density n_e and Z electrons). From the measured cross-sections one is able to determine the complex part of the dielectric function ϵ depending on the photon-energy $\hbar\omega$ for real photons as it is shown in equation (3.3) [26],

$$\sigma_\gamma(\omega) \approx \frac{Z\omega}{n_e c}\mathrm{Im}\left(\epsilon(\omega)\right) . \tag{3.3}$$

The real part of ϵ can then be derived from the imaginary part with the help of the KRAMERS-KRONIG

[2] The LANDAU distribution underestimates the fluctuations, while giving a good hint on the maximum of the PDF.

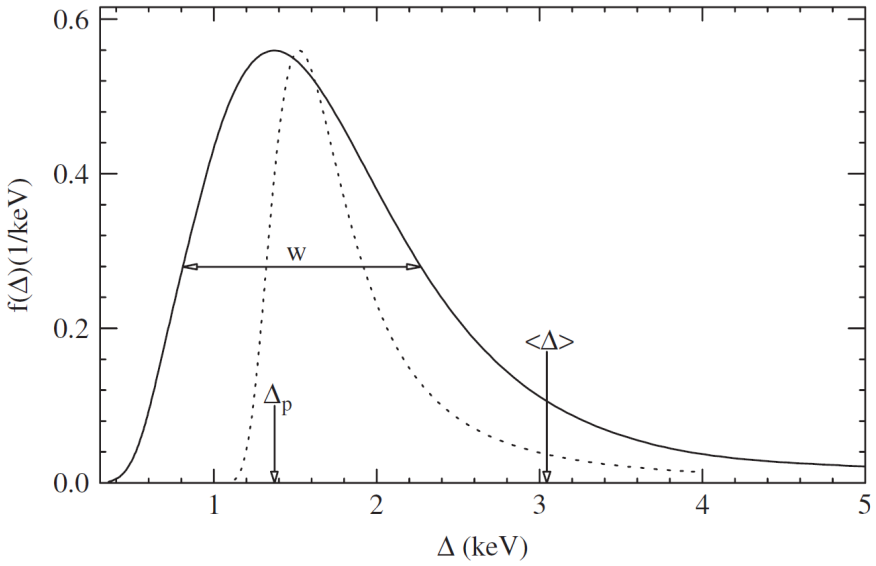

Figure 3.3: *Straggling function* of particles with $\beta\gamma = 3.6$ in 1.2 cm of argon gas compared to the LANDAU fluctuations that are indicated by the dotted line. The MPV is at 1.371 keV and the FWHM amounts to 1.463 keV. The plot is taken from [25].

relation. In a quantum-field-theory picture, the interaction between a charged particle that traverses the medium and the target atoms, is done via the exchange of virtual photons. So, to use the photo-absorption cross-section to describe the energy loss of charged particles, one needs to know the cross-section for off-shell photons. In the model of Allison and Cobb, the dielectric function is characterized also for virtual photons. Their work results in the differential cross-section shown in equation (3.4),

$$\frac{\mathrm{d}\sigma}{\mathrm{d}E} = \frac{\alpha}{\beta^2\pi}\left[\frac{\arg\left(1-\beta^2\epsilon^*\right)}{n_\mathrm{e}\hbar c}\left(\beta^2 - \frac{\mathrm{Re}\,(\epsilon)}{|\epsilon|^2}\right) + \frac{1}{E^2 Z}\int_0^E \sigma_\gamma\left(E'\right)\mathrm{d}E' \right.$$
$$\left. + \frac{\sigma_\gamma\left(E\right)}{EZ}\ln\left(\frac{2m_\mathrm{e}c^2\beta^2}{E\sqrt{\left(1-\beta^2\mathrm{Re}\,(\epsilon)\right)^2 + \beta^4\mathrm{Im}^2\,(\epsilon)}}\right)\right], \tag{3.4}$$

where α is the fine-structure constant. The first term accounts for *Čerenkov* radiation, and the last two terms take into account the energy loss due to ionization and the creation of δ-electrons. This cross-section is then the input to calculate the mean energy loss, but is also used to determine energy loss distributions.

3.2 Drift and diffusion

In the following section the movement of free charges in the detector in the presence of electric and magnetic fields will be discussed. This is necessary to determine important properties of the TPC as described in section 5.2.2. The theoretical concepts are based on [21, 26].

Free charges that are created, for example by an ionising event, move randomly in the gas in the absence of any field. Some electron-ion-pairs recombine and other charges collide with the gas molecules and loose all their kinetic energy up to some thermal energy. This thermal energy causes the diffusion of the charge. The situation looks different if external electric and/or magnetic fields are present. These fields lead to a different motion which is represented by the equation of motion (3.5)

$$m \frac{\mathrm{d}\mathbf{v}(t)}{\mathrm{d}t} = q\left(\mathbf{E} + \mathbf{v}(t) \times \mathbf{B}\right) , \tag{3.5}$$

where m represents the mass and q the charge of the moving particle, $\mathbf{v}$ its velocity, $\mathbf{E}$ and $\mathbf{B}$ the external electric and magnetic field. The right-hand-side of equation (3.5) is known as the Lorentz-force. During their movement, the charges will collide with the gas atoms (or molecules, depending on the gas) which causes some reversing force, comparable to a frictional force, that is especially velocity-dependent. If one adds this additional force to the right-hand-side of equation (3.5), one gets (3.6)

$$m \frac{\mathrm{d}\mathbf{v}(t)}{\mathrm{d}t} = q\left(\mathbf{E} + \mathbf{v}(t) \times \mathbf{B}\right) - K\mathbf{v}(t) , \tag{3.6}$$

where K denotes some proportionality factor. For a certain velocity $\mathbf{v}_{\text{drift}}$ the Lorentz-force and frictional force cancel each other, i.e. the system is in a steady-state. If this is the case, the velocity gets time-independent and one can write down the so-called Langevin-equation (3.7)

$$q\mathbf{E} = K\mathbf{v}_{\text{drift}} - q\mathbf{v}_{\text{drift}} \times \mathbf{B} . \tag{3.7}$$

This equilibrium is reached after a much longer time than some typical time $\tau = \frac{m}{K}$ that one can identify as the mean time between two collisions. With the cyclotron frequency $\omega = \frac{qB}{m}$ one can write down the drift velocity dependent on the electric and magnetic field. In equation (3.8) $\hat{\mathbf{E}}$ and $\hat{\mathbf{B}}$ denote unit vectors in the direction of the electric and magnetic field

$$\mathbf{v}_{\text{drift}} = \frac{q\tau E}{m} \frac{1}{1 + (\omega\tau)^2} \left[\hat{\mathbf{E}} + \omega\tau\left(\hat{\mathbf{E}} \times \hat{\mathbf{B}}\right) + (\omega\tau)^2 \left(\hat{\mathbf{E}} \cdot \hat{\mathbf{B}}\right)\hat{\mathbf{B}}\right] . \tag{3.8}$$

From the solution (3.8) one can deduce several drift velocities depending on the electric and magnetic field and their position relative to each other. The typical situation in a *time projection chamber* is that $\mathbf{E}$ and $\mathbf{B}$ are parallel which leads to a vanishing $\hat{\mathbf{E}} \times \hat{\mathbf{B}}$-term. But already small field inhomogeneities cause a finite contribution of this term. These $\mathbf{E} \times \mathbf{B}$-effects need to be taken into account in the track reconstruction.
In the case of the COMPASS++/AMBER proton charge-radius experiment one is dealing with a TPC without a magnetic field. That implies $\omega = 0$ and $\mathbf{v}_{\text{drift}} = \frac{q\tau}{m}\mathbf{E}$.

Another important aspect of the drift of free charges is the diffusion. If an ionizing particle liberates

a certain amount of electrons and ions one has a concentration gradient of the charge density ρ. This gradient is responsible for some resulting movements represented by the flux $\mathbf{j}$ that fulfills the continuity equation (3.9)

$$\frac{\partial \rho\left(\mathbf{x},\, t\right)}{\partial t} + \nabla \mathbf{j}\left(\mathbf{x},\, t\right) = 0\,. \tag{3.9}$$

Together with Fick's first law $\mathbf{j} = -D\nabla\rho$ with D being the diffusion coefficient one can rewrite the continuity equation (3.9) to the diffusion equation (3.10)

$$\frac{\partial \rho\left(\mathbf{x},\, t\right)}{\partial t} = D\nabla^2 \rho\left(\mathbf{x},\, t\right)\,. \tag{3.10}$$

The diffusion equation (3.10) is solved by a Gaussian distribution

$$\rho\left(\mathbf{x},\, t\right) = \frac{N}{\left(4\pi D t\right)^{1.5}} \exp\left(-\frac{\mathbf{x}^2}{4Dt}\right)\,, \tag{3.11}$$

with N being the number of diffusing charge carriers. From the solution one can deduce that the charge cloud is represented by a sharp peak for $t = 0$. For the isotropic case where the charge-movement has no preferential direction one has $\sigma = \sqrt{6Dt}$, where σ denotes the standard deviation of the Gaussian distribution (in the one-dimensional case it is simply $\sigma = \sqrt{2Dt}$). The time evolution of a charge cloud is depicted in figure 3.4.

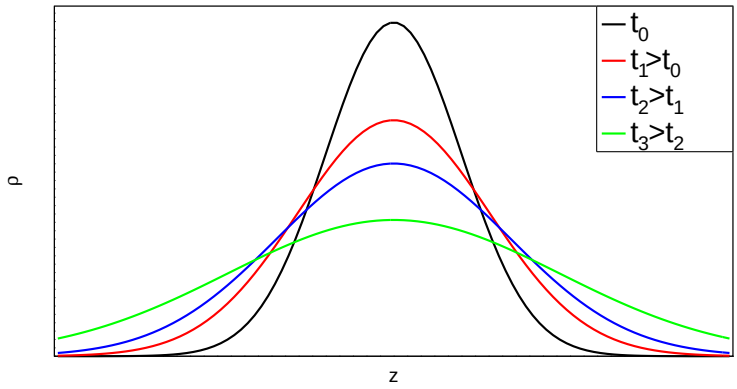

Figure 3.4: The time evolution of a charge cloud. As depicted in the legend, the following condition holds: $t_0 < t_1 < t_2 < t_3$.

In Garfield++ one can extract the so-called reduced diffusion coefficient $\tilde{D}$. This parameter takes the drift velocity into account, so that one can calculate the width σ of a charge distribution directly from the drift distance s, i.e.

$$\sigma = \tilde{D}\sqrt{s}\,. \tag{3.12}$$

3.3 Induced signals

One part of this thesis is the simulation of the electric signals of the pad read-out of the TPC. For the calculation of the induced current it is necessary to introduce the principle of the *weighting field* that is used in the so-called *Shockley-Ramo-theorem* to connect the drift of the charge created in the detector with the induced current. The presented concepts are based on [21, 27, 28].

The electrical signal that is created in the detector and read out by the following electronics is the current that is induced by the drift of the charges and is not the total number of charges collected by the electrodes. So in other words: the basic principle of signal creation is the movement of charges relative to the electrodes that are read out and not the charge collection itself. One consequence of this is that the signal already starts when the charges start to drift and not only if they arrive at the readout-electrode.

With the help of the *Shockley-Ramo-theorem* one is able to calculate the currents induced in all detector electrodes for arbitrary geometries. It is only based on energy conservation and can therefore be derived from first principles. For the derivation, it is referred to the original papers from Shockley [27] and Ramo [28].

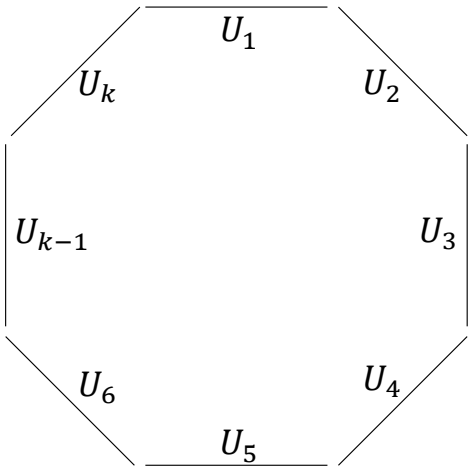

Figure 3.5: Picture of an arbitrary system with k-electrodes.

A basic principle in the theorem is the *weighting field* $\mathbf{E}_{\mathrm{w},\,i}$ of an electrode i that is part of the read-out of the detector consisting of several electrodes. The overall potential inside the detector volume can be calculated by the sum of every single-electrode potential, where the electrode of interest is set to U_i all others are set to ground potential. For a k-electrode system as it is depicted in figure 3.5 this leads to

$$\phi_0\left(\mathbf{r}\right) = \sum_{i=1}^{k} \phi_i\left(\mathbf{r}\right) \qquad \text{and} \qquad \mathbf{E}_0\left(\mathbf{r}\right) = \nabla\phi_0\left(\mathbf{r}\right) \,,$$

where the single potentials ϕ_i fulfill the two conditions

$$\phi_i(\mathbf{r}_i) = U_i \qquad \text{and} \qquad \phi_i(\mathbf{r}_j) = 0 \qquad \text{for} \qquad i \neq j \,.$$

Here, $\mathbf{r}_i$ is the location of electrode i and $\mathbf{r}_j$ the locations of all others. The electric field $\mathbf{E}_0$ is given as the gradient of the potential ϕ_0. The so-called *weighting potential* $\phi_{\mathrm{w},\,i}$ and *weighting field* $\mathbf{E}_{\mathrm{w},\,i}$ of electrode i are defined as

$$\phi_{\mathrm{w},\,i}\,(\mathbf{r}) = \frac{\phi_i\,(\mathbf{r})}{U_i} \qquad \text{and} \qquad \mathbf{E}_{\mathrm{w},\,i}\,(\mathbf{r}) = \nabla\phi_{\mathrm{w},\,i}\,(\mathbf{r}) \,.$$

The *weighting field* can be understood as that field, where all moving charges are removed, the electrode of interest is set to 1 V and all others are grounded. The conservation of energy then leads to the fact that some amount of charge needs to be induced in electrode i. This is known as the *Shockley-Ramo-theorem* (3.13),

$$\mathrm{d}Q_{\mathrm{ind},\,i}\,(t) = -q\mathbf{E}_{\mathrm{w},\,i}\left(\mathbf{x}\,(t)\right) \cdot \mathrm{d}\mathbf{x}\,(t) \,. \tag{3.13}$$

Taking the time derivative of equation (3.13) (the weighting field needs to be calculated at the position of the drifting charge but it is a constant quantity with respect to the time t; therefore one only needs to differentiate the position vector of the charge) one gets the induced current in electrode i as shown in (3.14),

$$I_{\mathrm{ind},\,i}\,(t) = q\mathbf{E}_{\mathrm{w},\,i}\left(\mathbf{x}\,(t)\right) \cdot \mathbf{v}\left(\mathbf{x}\,(t)\right) \,, \tag{3.14}$$

where $\mathbf{v}\left(\mathbf{x}\,(t)\right)$ can be identified with the macroscopic drift velocity. From the presented concepts one can deduce that the electric signal is defined by the weighting field and therefore the overall geometry. It also does not directly depend on the real electric field inside the detector or the applied voltage. This only influences the drift velocity of the charges.

As in a TPC the drift velocity is mainly in the direction of the cylinder-axis, i.e. the z-axis, and constant (cf. section 5.1) equation (3.14) reduces to

$$I_{\mathrm{ind},\,i}\,(t) = qv_{\mathrm{drift}}E_{\mathrm{w},\,i,\,z}\left(\mathbf{x}\,(t)\right) \,. \tag{3.15}$$

Equation (3.15) indicates that the shape of the induced current in the TPC corresponds to the shape of the z-coordinate of the weighting field along the drift line of the charge. So the total induced charge can be calculated by integrating the z-component of the weighting field along the drift line.

CHAPTER 4

The COMPASS++/AMBER experiment

In this chapter, the key components of the foreseen COMPASS++/AMBER-experiment are presented. Further details can be found in [11].
COMPASS++/AMBER (**CO**mmon **M**uon **P**roton **A**pparatus for **S**tructure and **S**pectroscopy++; **A**pparatus for **M**eson and **B**aryon **E**xperimental **R**esearch) is a fixed target experiment located at the M2 beam line of the CERN SPS (**S**uper **P**roton **S**ynchroton). The proton beam coming from the SPS is shot on a production target creating secondary and/or tertiary beams. From this target a muon or hadron beam (for example kaons or pions) is guided towards the actual target of the experiment.
A picture of the whole, approximately 60 m long setup can be seen in figure 4.1. A 2D picture with an overall length scale is depicted in figure 4.2.

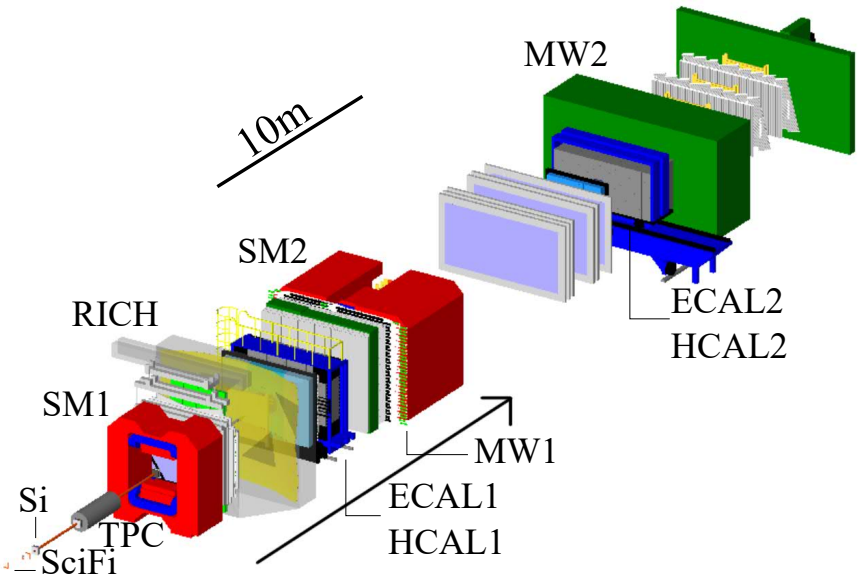

Figure 4.1: 3D-picture of the COMPASS++/AMBER-experiment as it is foreseen for the proton charge radius run. The small gray vessel on the down-left side is the active-target TPC. The arrow represents the direction of the beam. Taken from [29]; modified.

The high-intensity muon beam is coming from the bottom-left corner in figure 4.1. The target of

the proton charge radius run is an active-target hydrogen TPC operated in ionization mode mainly at 20 bar, but also at 4 bar. Its working principle is described in section 5.1.

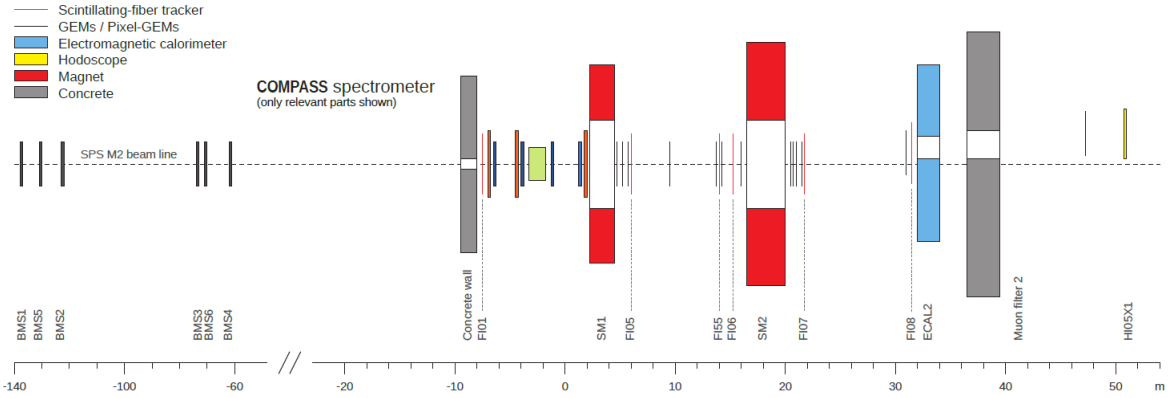

Figure 4.2: 2D-picture of the COMPASS++/AMBER-experiment as it is foreseen for the proton charge radius run. The muon beam is coming from the left. The TPC is marked in green. Taken from [11].

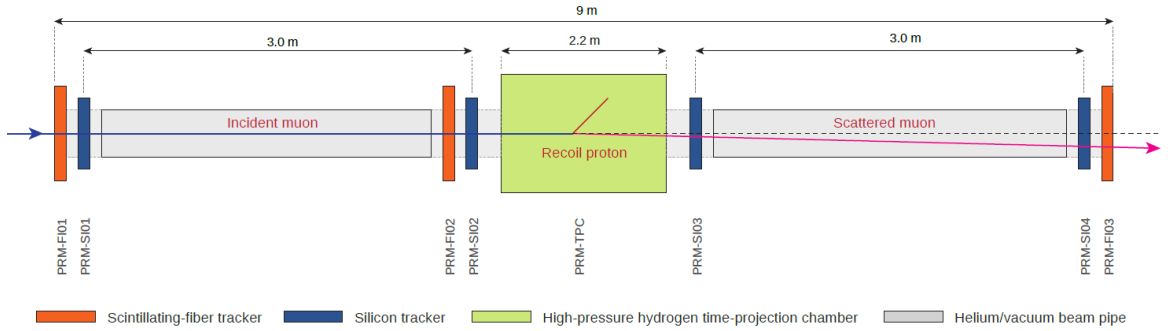

Figure 4.3: This is a zoomed version of figure 4.2, with the main detector components for the proton charge radius measurement; i.e. the scintillating fibers, the silicon telescopes and the TPC. Taken from [11].

Besides the active-target TPC the main detector components for the proton charge-radius measurements are three scintillating fibers and four silicon detectors used as telescopes. The scintillating fibers are used to get a precise time information and are considered for triggering purposes. With the silicon telescopes up- and downstream of the target tracking of the muons is feasible.
Besides the components the existing COMPASS spectrometer will be used to extract further information of the scattered particles. Its main features are the measurement of the beam momentum and the scattered muon identification. One has a two-stage spectrometer measuring large (with trackers around SM1 and calorimeters) and small (with trackers around SM2 and calorimeters) scattering angles together with tracking detectors like the large-area Pixel-GEM detectors [30]. For the proton charge-radius measurement the upstream magnet, that is near one to the TPC, will not be used. Otherwise one would have magnetic field components in the TPC.
The electromagnetic calorimeters will be used to detect photons that are created within higher order processes, i.e. radiative corrections. With the detection one can control such systematics.

CHAPTER 5

The Time Projection Chamber

In the COMPASS++/AMBER proton charge-radius experiment it is foreseen to extract the cross-section for elastic scattering of muons momenta of 100 GeV c^{-1} on protons in a squared momentum-transfer range

$$0.001\,\mathrm{GeV}^2\,c^{-2} < Q^2 < 0.04\,\mathrm{GeV}^2\,c^{-2}\,,$$

corresponding to kinetic energies of the proton in the order of 0.5 to 20 MeV. The measurement of such low momentum transfers and scattering angles of about lead to the need of an active target to track the scattered protons. This active target will be a *time projection chamber* (TPC). The idea of the TPC is described in section 5.1, while the design and parameters are discussed in sections 5.2.

5.1 Working principle of a TPC

As mentioned previously, the active target of the COMPASS++/AMBER proton charge-radius measurement is a *Time Projection Chamber*. Its basic principle has been introduced by David R. Nygren in 1976 [31] and is shown in figure 5.1.
A TPC is a gas-based detector. It comes mostly in the form of a cylinder with an anode and cathode at its end caps. With it one is able to reconstruct the three-dimensional track of an ionising particle. Additionally, one can measure the energy lost by the traversing particle to extract further information. The principle is based on the ionisation of the gas along the track of the traversing particle. A homogeneous, electric field between anode and cathode is responsible for the separation of the charges. Typically, the anode is on ground potential and the positive high-voltage is applied on the cathode. Therefore, the electrons drift towards the anode where the read-out is done and the ions drift to the cathode. The three coordinates of a track point are reconstructed as follows:
The electrons created at a certain point in the gas volume induce a signal on the read-out plane. When reading out the actual position of this signal one gets the x- and y-coordinates of that point[1]. To reconstruct the correct transverse coordinates it is necessary to have a quite homogeneous electric field in the TPC. Otherwise so-called field-distortions would lead to wrong reconstructed track points. Another important reason for a homogeneous field is that the drift velocity of the electrons need to be constant as the z-coordinate is reconstructed with the help of the drift time. By measuring the time

[1] With a pad read-out one can extract the coordinates of the point in terms of pad coordinates.

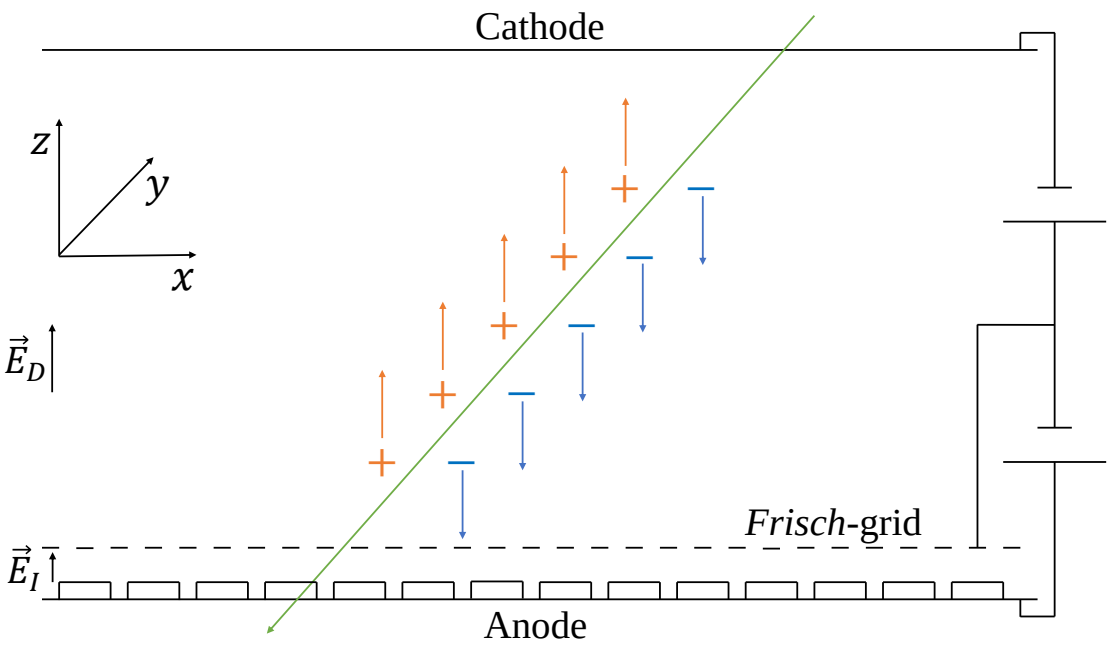

Figure 5.1: Working principle of a TPC with a *Frisch*-grid above the read-out anodes (all elements of the grid are connected to the same potential as it is indicated by the second right element). An ionising particle traverses the sensitive medium which is in the most cases a gas. On its way through the detector the particle liberates electron-ion pairs that drift in the applied electric field towards the corresponding electrodes. The electrons induce a signal on the anodes as soon as they pass the grid. The picture is not to scale.

when the particle passes the detector and when the signal occurs at the read-out one gets the drift time of the electrons. By knowing the drift velocity one can then calculate the drift distance and therefore the z-coordinate of the track point.
Another parameter of the particle that can be measured is the energy loss. This is done by summing up all single signals that belong to the particle of interest. The number N of created electron-ion-pairs is proportional to the deposited energy ΔE, i.e.

$$N = \frac{\Delta E}{W},$$

where W denotes the work function of the material [32]. The work function describes the amount of energy that is needed to create on average one electron-ion-pair.

5.2 The hydrogen-based TPC at COMPASS++/AMBER

5.2.1 The design

The design of the TPC that will be used in the experiment is shown in figure 5.2. It is quite similar to that deployed in the Mainz-experiment [12] leading to a similar energy-range calibration. The TPC consists of four cells. Two of these volumes each share one cathode while all have their own read-out anode. Every cell consists of a drift and induction zone. The drift length is 40 cm and the induction

gap has a length of 1 cm. The drift and induction gaps are separated by a *Frisch*-grid. This grid is used on the one hand to electrically decouple the drift and induction zones. On the other hand it has a huge influence on the signals that are induced in the anodes. In a simple parallel plate capacitor the signal depends on the point in the detector where the charges are created. Because of the electrical separation the signal induction in the anodes does not start directly after the charge creation, but when the electrons reach the grid. This leads to a signal that is independent of the z-position as long as the charges are created within the drift region which means between cathode and *Frisch*-grid [33]. Another point is that one does not have an ion-component of the signal what would typically be the slow part of the signal.

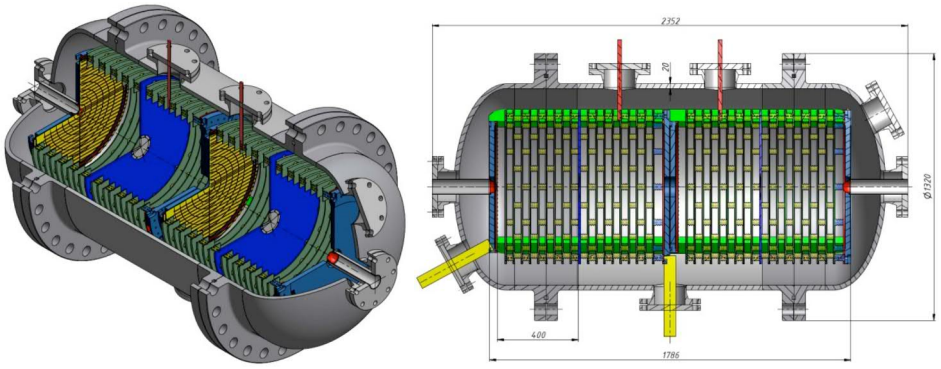

(a) 3D-model of the planned TPC. (b) Cut-through of the planned TPC.

Figure 5.2: Design of the TPC that will be used in the experiment. Taken from [11].

The TPC is operated in ionization mode, meaning that there is no amplification of the electric signal in front of the read-out. The TPC is operated mainly at 20 bar, where one has a drift field of 2.32 kV cm^{-1} and an induction field of 10 kV cm^{-1}. The usage of such a high pressure has different origins:

- The probability for elastic scattering of muons on protons needs to be high enough. Otherwise one needs to have fairly long beam times to collect enough statistics.
- The energy loss of the scattered proton needs to be high enough to be detectable.
- The protons need to be stopped in the TPC to detect the total energy.

But there will be runs at 4 bar too studying systematic effects like two-photon exchange [11]. At the low pressure setting there will be also low Q^2-data collected. At 4 bar the field configurations are as follows: The drift field is 464 V cm^{-1} and the induction field is 2 kV cm^{-1}. The values for the induction fields are slightly higher [34] than given in the proposal [11] (cf. table 5.1). The electric field in the drift zone is not only defined by the cathode and grid potential, but it is also formed by field correction rings (small yellow elements at the outer part of the TPC in the right figure 5.2). These are used to reduce field distortions and to have then a more homogeneous field (as discussed in section 5.1).
The TPC will be connected to a gas circulation and purification system to guarantee a level of impurities $\leq$ 1 ppm. These impurities can lead to attachment and therefore a loss of drifting electrons and finally the signal.

5.2.2 Determination of drift parameters

For further studies it is necessary to know the drift and diffusion parameters of electrons in the TPC at the given pressure and electric field settings. To extract these information a simple Garfield++-program was written. In Garfield++ one has an interface to Magboltz by Stephen Biagi [35]. It deals with transport parameters for electrons in various gases and gas mixtures. These transport properties depend on a few parameters like the cross-section for a certain process. Magboltz has an immense internal database where these cross-sections are tabulated. With this it is possible to do electron tracking on a microscopic basis. Garfield++ together with Magboltz is able to simulate various electron and ion properties in gases.

To run Magboltz one has to define the detector gas, its temperature and pressure. All of this and the interface is done with the class MediumMagboltz. The implementation is shown in the appendix G. The results are depicted in table 5.1.

Region	E in kV cm^{-1}	p in bar	v_{drift} in cm ms^{-1}	$\tilde{D}_{\text{T}}$ in µm cm$^{-0.5}$	$\tilde{D}_{\text{L}}$ in µm cm$^{-0.5}$
Drift	0.464	4.0	417.1 ± 0.4	158.7 ± 2.2	125.5 ± 1.3
	2.32	20.0	417.0 ± 0.4	70.6 ± 0.8	57.6 ± 1.4
Induction	2.0	4.0	841.6 ± 0.7	131.6 ± 1.9	87.8 ± 1.6
	10.0	20.0	841.8 ± 0.7	58.7 ± 0.8	38.5 ± 0.8

Table 5.1: Simulated drift and diffusion parameters for a hydrogen-based parallel plate capacitor for the given pressure and electric field settings.

The drift gap of the TPC will be $s = 40\,\text{cm}$ long. This implies a maximal width of a charge cloud of

$$\sigma_{\text{T}} = (1.004 \pm 0.014)\,\text{mm} \qquad \text{and} \qquad \sigma_{\text{L}} = (0.794 \pm 0.008)\,\text{mm}$$

for a pressure of 4 bar and

$$\sigma_{\text{T}} = (0.446 \pm 0.005)\,\text{mm} \qquad \text{and} \qquad \sigma_{\text{L}} = (0.365 \pm 0.009)\,\text{mm}$$

of 20 bar.

The diffusion in the induction gap can be neglected as the drift distance is only 1 cm which would lead to widths in the order of 100 µm at pad sizes in the order of several cm.

The drift velocity of electrons in hydrogen at reduced fields of 116 V cm^{-1} bar^{-1} and 500 V cm^{-1} bar^{-1} are stated with values of about 400 cm ms^{-1} and 850 to 900 cm ms^{-1} [36, 37]. These are in good agreement with the data extracted from Magboltz stating that its linear pressure scaling is applicable.

CHAPTER 6

Comparison of energy-loss models

The basic principle of a tracking detector like a TPC, as described in section 5.1 is the ionization of the used sensitive medium by an ionizing particle that deposits some amount of energy there, and the detection of the created charges. In a **M**onte-**C**arlo simulation the energy-loss process is described by certain models which will be compared to each other. But one needs to point out that such a model cannot be accurate in every energy regime, for every particle and interaction. This motivates the comparison of different models. A widely used one is the PAI-model. It can be used to describe the energy loss of charged particles in the GEANT4- and GARFIELD++-frameworks. Both approaches will be compared to each other in terms of mean and most probable energy loss as well as in terms of width of the distributions. Finally, the energy-loss models implemented in TGEANT will be presented.

6.1 Comparison of the PAI-model in GEANT4 and GARFIELD++

The **P**hoto-**A**bsorption-**I**onisation-model is a widely known model to describe the energy loss of charged particles. It is typically used to calculate the energy loss in thin absorbers like silicon or gaseous detectors. It is also implemented in the GEANT4-framework and within HEED++ that is used via an interface from GARFIELD++ for simulation purposes.

6.1.1 Implementation

In GARFIELD++ one can make use of the TRACKHEED-class after one has defined all detector components (the implementation of a parallel-plate-capacitor as a detector is shown in the appendix G) [38]. To simulate the energy loss one needs to define some further things:

```
TrackHeed *track = new TrackHeed();
track->SetParticle("particle");
track->SetMomentum(p);
```

One can choose out of a list of predefined particles like muons, protons or electrons, but one can also define own particle properties. Then the energy or momentum of the particle needs to be set. Energies are given in eV and momenta in eV c^{-1}. The energy-loss simulation is started via

```
track->NewTrack(x0, y0, z0, t0, dx0, dy0, dz0);
```

where the starting position $(x_0,\ y_0,\ z_0)$ and time t_0 of the particle needs to be handed over as well as its initial direction $(\mathrm{d}x_0,\ \mathrm{d}y_0,\ \mathrm{d}z_0)$. Then the track of the particle through the medium is calculated

with its excitation and ionization points. The information of all created clusters[1] (mainly the deposited energy in all collisions) can be retrieved via

```
track->GetCluster(x, y, z, t, ne, eloss, info)
```

where *ne* describes the number of electrons in a cluster and *eloss* the energy that is lost. The variable *info* is only used for debugging purposes. Here, the position of the ionization (x, y, z) as well as its time t relative to the starting time of the track can be retrieved. To get finally a histogram like it is shown in figure 6.1 one needs to simulate various tracks.

In GEANT4 it is rather simple to activate the PAI-model when defining the physics list[2]. Here, one just needs to add the PAI-model to list of electromagnetic parameters by defining the particles for which and the volumes where it should be used as the model to simulate the energy loss.

```
G4EmParameters::Instance()->AddPAIModel("particles", "region", "pai");
```

The detector components are implemented via the so-called G4VUSERDETECTORCONSTRUCTION-class. There, a world volume needs to be defined containing all necessary sub-volumes where the interactions are simulated. Typically, the world volume consists of a very low-density material called G4_GALACTIC as no interactions should happen in there. The actual detector, a 12 mm-thick hydrogen-based parallel plate capacitor at 20 bar (like in GARFIELD++) is placed at the center of the world volume. The maximal size of a simulation step needs to be defined here as well. It is chosen to be 0.75 mm. This value has nothing to do with something like the mean free path in the material but in GEANT4 it has a clear motivation. The cross-section for a certain interaction depends on the energy of the particle. In a step it is assumed that the cross-section stays constant. To ensure this the steps needs to be small. But with small steps the computing time increases as more steps need to be performed. The actual length of the step is randomly chosen based on the energy and the interaction cross-section [39].
From the G4USERSTEPPINGACTION-class one can retrieve the information of a simulated step. These are for example the deposited energy of the length of the performed step.
Within the G4VUSERPRIMARYGENERATORACTION-class the beam particles, their energy or momentum and initial direction can be defined. One can also randomize the energy and the direction if needed. The simulation itself is started by activating the beam by defining the number of events that should be simulated and is then done on an event-by-event basis. For each event the primary particle is tracked through the medium. If secondary particles are created, for example δ-electrons their interactions with the sensitive medium are simulated as well. If a particle has deposited all its kinetic energy, i.e. it is stopped in the detector, its simulation is stopped. The simulation is stopped as well if the particle has left the volume.

[1] In GARFIELD++ a simulated interaction point is called a cluster. It contains information about the position and time of the collision, the deposited energy and the number of created electron-ion pairs.

[2] In the physics list all interactions processes like ionization, bremsstrahlung or multiple scattering that should be taken into account in the simulation are defined. Here one can also set various energy ranges where the processes are valid, as well as range cuts. These cuts are considered for example for the creation of δ-electrons. If the electrons do not have the energy corresponding to a range larger than the cut then they will not be created (this is implemented just because of computing time purposes).

6.1.2 Results

The first straggling functions that are compared are that of 100 GeV c^{-1} muons in 12 mm hydrogen gas[3] at 20 bar as shown in figure 6.1. Muons with such a momentum are highly relativistic but these are the energies that will be used at the planned COMPASS++/AMBER proton charge-radius experiment. A value of $\beta\gamma \approx 950$ is also still in the applicable range of the BETHE-BLOCH-equation. Therefore the PAI-model should also be still valid but high energy corrections like bremsstrahlung or pair production are already modifying the overall energy loss.

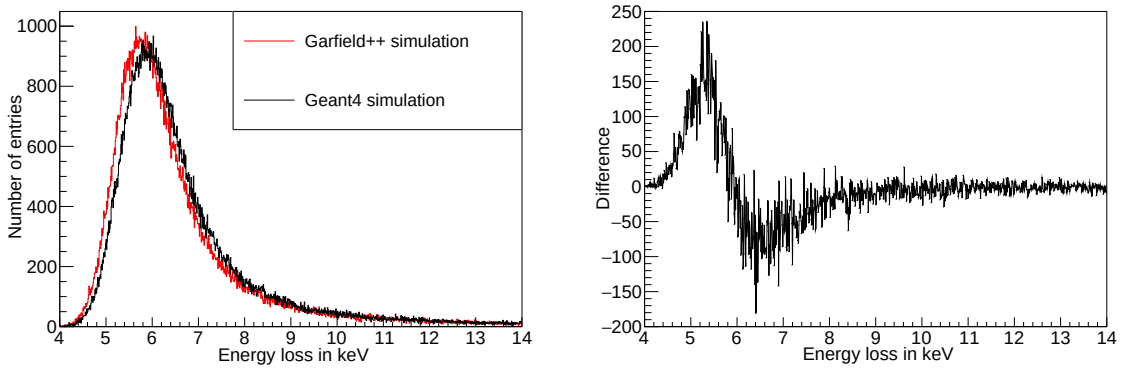

(a) The red curve shows the distribution coming from the PAI-model implemented in GARFIELD++; the black one represents the PAI-model in GEANT4.

(b) Difference of the distributions shown on the left.

Figure 6.1: Energy-loss distribution of 100 GeV c^{-1} muons in a 12 mm-thick hydrogen gas target at 20 bar as well as the difference between GARFIELD++ and GEANT4.

In figure 6.1 one can see differences in the simulated straggling up to values of 9 keV between GARFIELD++ and GEANT4. There are clear distinctions on the rising and falling edges of the energy-loss distributions leading to a small shift of the most probable energy loss of about 0.2 keV. These differences have a clear origin. The model used for excitation and ionization is in both cases the PAI-model. But in GEANT4 bremsstrahlung and pair production are implemented in addition. Bremsstarhlung especially as a radiative correction to the BETHE-BLOCH-equation has a non-negligible contribution to the energy loss for highly relativistic particles. These additional implemented processes lead to a small shift of the most probable energy loss as well as the mean but they have no influence on the width of the distribution. It does not decrease or increase the width of the straggling function as the bremsstrahlung and pair production processes are implemented without fluctuation models within GEANT4.
The mean energy loss can be extracted to be about 6.5 keV coming from GARFIELD++ and 6.7 keV simulated in GEANT4[4]. These values are too small compared to a value of approximately 8.4 keV from [40] when doing a linear pressure scaling and assuming a density of 8.3748×10^{-5} g cm^{-3} [24]. The

[3] Bichsel uses mostly a thickness of 12 mm in his calculations in [25]. Therefore this value was chosen.

[4] The most probable and mean values are based on a fit of a convolution of a *Landau*- and a *Gauss*-distribution as shown in appendix E.

value it is refereed to is taken under the assumption that muons with momenta of 100 GeV c^{-1} are minimum ionizing.

Following these discussions the straggling function for MIPs should be the same in both frameworks as radiative corrections do not play a role at such energies. The distributions for 5 GeV-proton ($\beta\gamma \approx 6.2$) are depicted in figure 6.2.

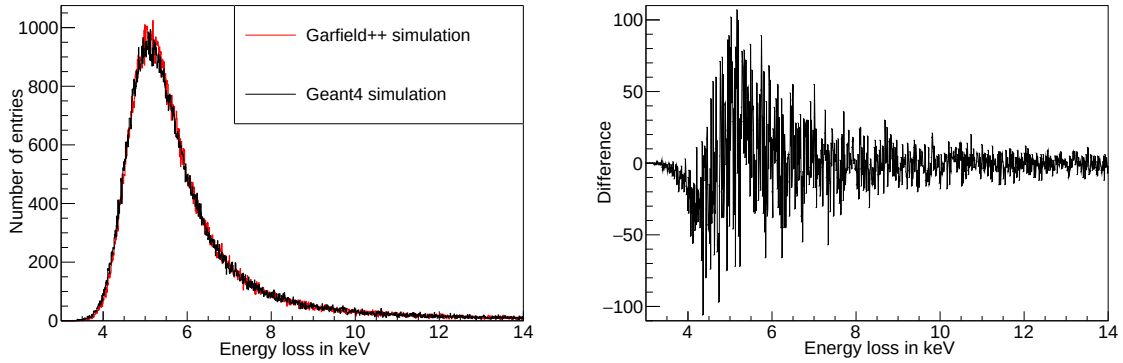

(a) The red curve shows the distribution coming from the PAI-model implemented in GARFIELD++; the black one represents the PAI-model in GEANT4.

(b) Difference of the distributions shown on the left.

Figure 6.2: Energy-loss distribution of 5 GeV protons in a 12 mm-thick hydrogen gas target at 20 bar as well as the difference between GARFIELD++ and GEANT4.

Both straggling functions in figure 6.2 mostly coincide but show deviations again on the leading and falling edges of the distributions of up to 10 %. Both have the same most probable value of 5.2 keV and mean value of 5.9 keV. Compared to the PSTAR-value of 8.5 keV the extracted mean energy loss is too small.

The energy-loss distributions in the low-energy regime are shown in figure 6.3 for 10 MeV protons ($\beta\gamma \approx 0.15$). These are energies on the low end of the applicable range for the BETHE-BLOCH-equation where the energy loss is vastly dominated by the β^{-2}-term.
In this energy range the energy-loss distributions coincide with maximal deviations of about 5 to 10 %. From both a mean of 196 keV can be extracted. In these energy regimes the stopping of particles becomes relevant, i.e. the region of the *Bragg*-peak. At such energies the energy loss calculated by BETHE-BLOCH is not accurate anymore as the traversing particles have velocities in the order of these of the shell electrons. Here one needs to do a quantummechanical calculation which is not part of the calculations of the PAI-model. In simulation frameworks like GEANT4 the energy loss is then based on experimental data to describe it accurately. Such a simulation in which a part, i.e. the *Bragg*-model in table 6.1, is based on experimental data is shown in figure 6.4.
Here the straggling simulated with the *Livermore*-model [39] implemented in GEANT4 is depicted. There one can see a clear difference to the PAI-model leading to a too small mean energy loss of 195 keV. The PSTAR-value at 10 MeV is stated with 204.8 keV which is in good agreement with the result from the *Livermore*-model.

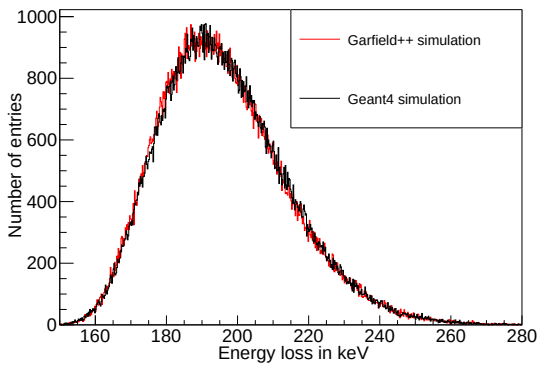

(a) The red curve shows the distribution coming from the PAI-model implemented in GARFIELD++; the black one represents the PAI-model in GEANT4.

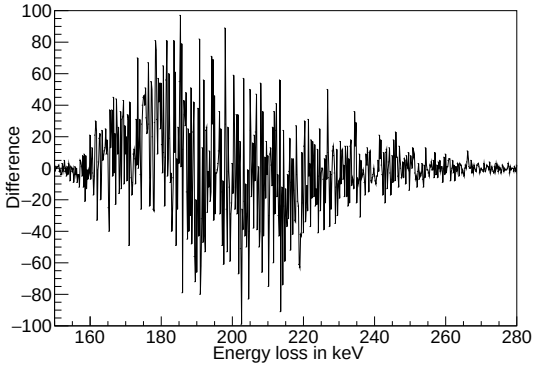

(b) Difference of the distributions shown on the left.

Figure 6.3: Energy-loss distribution of 10 MeV protons in a 12 mm-thick hydrogen gas target at 20 bar as well as the difference between GARFIELD++ and GEANT4.

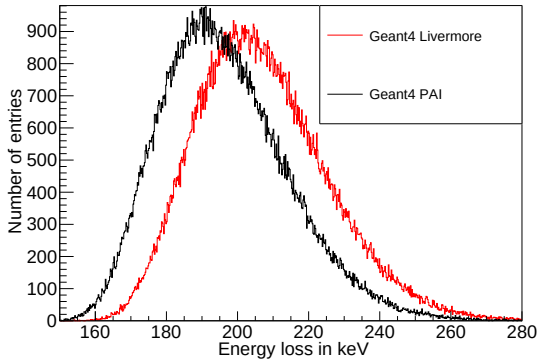

(a) The red curve shows the distribution coming from the *Livermore*-model [39] and the black one represents the PAI-model in GEANT4.

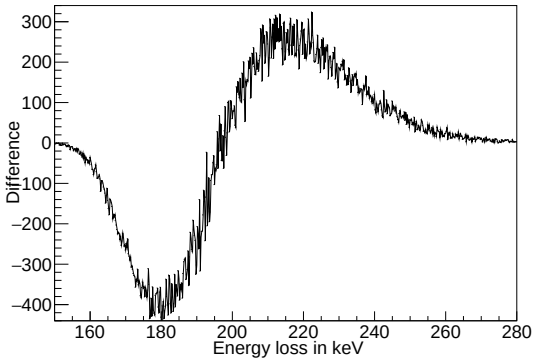

(b) Difference of the distributions shown on the left.

Figure 6.4: Energy-loss distribution of 10 MeV protons in a 12 mm-thick hydrogen gas target at 20 bar as well as the difference between the *Livermore*- and PAI-model.

Following the discussions up to now the PAI-models in both GARFIELD++/HEED++ and GEANT4 underestimate the mean energy loss per unit length in all energy ranges it has been looked at. The *Livermore*-model in GEANT4 simulates a too small mean value as well when analyzing momenta $\beta\gamma \gtrsim 0.5$. Below that the results coincide with the PSTAR-database [23] (cf. figure 3.1) as it is based on experimental data in this energy regime. Here one has to state that the referenced data is just scaled by the length of the simulated detector, i.e. 12 mm. But the energy loss itself depends on the particle's energy and therefore on the length of the traversed medium. A linear scaling has therefore only limited applicability. Instead one needs to integrate the differential energy loss along the particle track. When

looking at the TPC that will be deployed in the experiment, the mean energy loss of high-energetic muons coincide with the literature. This is not the case for the small detector of 12 mm. This finding underlines that the calculation of the mean energy per unit length depends itself on the detector length as the fluctuations depend on the thickness of the detector.

Up to now the widths of the distributions simulated with the PAI-models have not been compared to measurement or calculations. H. Bichsel calculated the straggling of simply charged particles with a momentum of $\beta\gamma = 3.6$ [25]. A calculated energy-loss distribution in argon is depicted in figure 6.5 together with simulation result from GEANT4 and GARFIELD++.

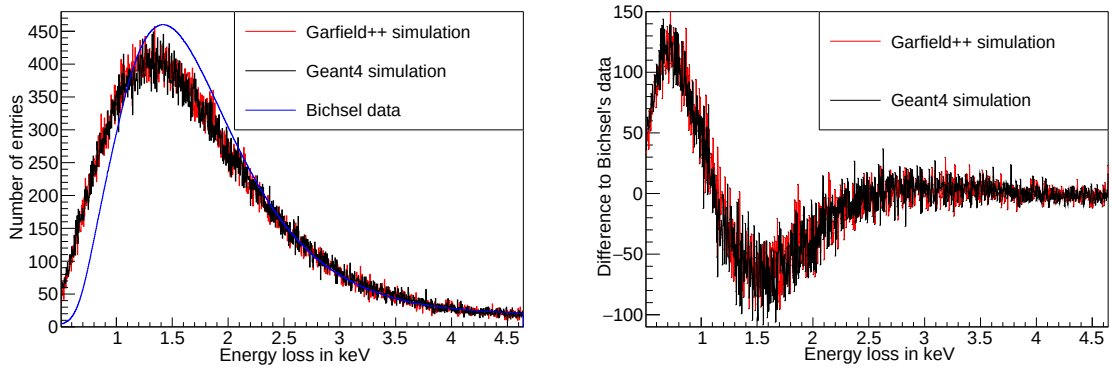

(a) The red curve shows the distribution coming from the PAI-model implemented in GARFIELD++; the black one represents the PAI-model in GEANT4 and the blue is calculated by H. Bichsel [25].

(b) Difference of the distributions shown on the left with respect to the Bichsel data.

Figure 6.5: Energy-loss distribution of protons with $\beta\gamma = 3.6$ in 12 mm argon gas at 1 bar as well as the difference between the simulations and the results calculated by H. Bichsel [25].

The simulation results coincide in a way like it is shown in figure 6.2 as in both cases it has been dealt with minimum-ionizing protons. The straggling function calculated by Bichsel is starting at energy losses of 0.5 keV whereas the PAI-models already have a finite probability for energy losses down to 0.3 keV what is not shown in 6.5. Therefore, one can observe a sharper rise of the calculated distribution. At around 2.5 keV at the falling edge of the distributions the simulations and calculation nicely overlap. The estimated width from Bichsel is 1.463 keV and from the simulations one can extract 1.5 keV. Even though the distributions only coincide for energy losses larger than 2.5 keV the same FWHM can be explained by a sharper increases and decreases in the case of the calculated data from Bichsel. The results from GEANT4 and GARFIELD++ increase and decrease slower compared to Bichsel's estimations leading to a comparable width of both simulations and calculation. The most probable value is therefore shifted to slightly higher energy losses, i.e. 1.371 keV from Bichsel compared to 1.25 keV from the PAI-model in both GARFIELD++ and GEANT4.

Following these discussions one can say that the PAI-models implemented in GEANT4 and GARFIELD++ coincide with deviations of up to 10 % in some cases and not in comparison to measured data. These deviations are limited to the leading and falling edges of the energy-loss distributions. The mean and

most probable values extracted from both frameworks are the same as well as the estimated widths. Compared to literature and databases the mean energy losses are too small with deviations up to 20 %. For high-energetic particles the PAI-model itself is loosing accuracy as it does not describe radiative losses like bremsstrahlung. Therefore, other models need to be taken into account as well. At the low energy side of the Bethe-Bloch-curve it is only applicable with larger deviations especially in terms of mean and most probable energy loss. In such an energy range one needs to take the stopping of the particle into account, i.e. the *Bragg*-peak at the end of the trajectory of the particle. Therefore, one can make use of experimental data described in Geant4 which should be used at such low energies. The widths of the simulated distributions are comparable to the calculations from Bichsel for minimum-ionizing particles. From this one can deduce that the PAI-model is definitely accurate for simulations of energy resolutions as the widths and long tails of such straggling distributions are crucial for the performance of a particle detector.

6.2 Energy-loss model in TGeant

The particles of special interest are high-energetic muons and low-energetic protons. The used models in the TGeant physics list are the ones depicted in table 6.1.

Particle	Model	T_{min}	T_{max}
Proton	Bragg	0	2 MeV
	BetheBloch	2 MeV	100 TeV
	hBrem	0	100 TeV
	hPairProd	0	100 TeV
Muon	Bragg	0	200 keV
	BetheBloch	200 keV	1 GeV
	MuBetheBloch	1 GeV	100 TeV
	MuBrem	0	100 TeV
	MuPairProd	0	100 TeV

Table 6.1: The different models used in TGeant for muons and protons with the low kinetic-energy limit T_{min} and the high energy limit T_{max} of the model.

For muons the first two models do not play any role as the energy of the muon beam is 100 GeV. For the low energy protons (E_{kin} is in the order of 1 MeV) one can expect the main contribution to the energy loss coming from the Bragg-model. All these models beside the ones describing bremsstrahlung and pair production make use of fluctuation models that describe the energy-dependent straggling of the particle.
For muons in the energy regime of interest the common model to describe the straggling is the so-called G4UniversalFluctuation-model [39, p. 70 ff]. In this model it is assumed that the atoms of the traversed material have two energy levels with binding energies E_1 and E_2. Beside that the atom has an ionisation threshold of E_0. With the corresponding interaction cross sections one is able to calculate the mean energy loss in a step with length Δx. The actual energy loss in this step is then sampled in the following way:
The excitation energy loss (represented by E_1 and E_2) is calculated by

$$\Delta E_{\text{exc}} = n_1 E_1 + n_2 E_2 \,,$$

where n_1 and n_2 are the number of excitations drawn from Poisson distributions that depend on the cross section for the interactions with these energy levels. The ionizing energy loss is calculated by

$$\Delta E_{\text{ion}} = \sum_{j=1}^{n_3} \frac{E_0}{1 - u_j \frac{T_{\text{up}} - E_0}{T_{\text{up}}}} \,.$$

n_3 represents the number of ionizations again sampled from a Poisson distribution, u_j is uniformly distributed in the interval 0 to 1 and T_{up} describes the maximum energy transfer.
The full energy loss is then the sum of the excitation and ionization parts, i.e.

$$\Delta E = \Delta E_{\text{exc}} + \Delta E_{\text{ion}} \,,$$

where the fluctuations originate from sampling the number of excitations and ionizations, as well as from drawing the actual energy loss in a single ionizing collision.

For protons one has the same fluctuation model as for muons for energies higher than 2 MeV. For energies below that threshold the G4IonFluctuations-model is applied. In the energy regimes of interest for protons they are stopped anyhow in the TPC as visible in figure 6.6. The specific energy loss of protons will be used as described in the introduction 1 to determine the proton energy in a momentum transfer range $\geq 0.015\,\text{GeV}^2\,c^{-2}$ as this corresponds to the energy for which the protons can leave the TPC (cf. figure 6.6). If they leave the TPC it is not possible anymore to reconstruct their full energy; but their specific energy loss is a useful criterion to determine the kinetic energy of the proton.

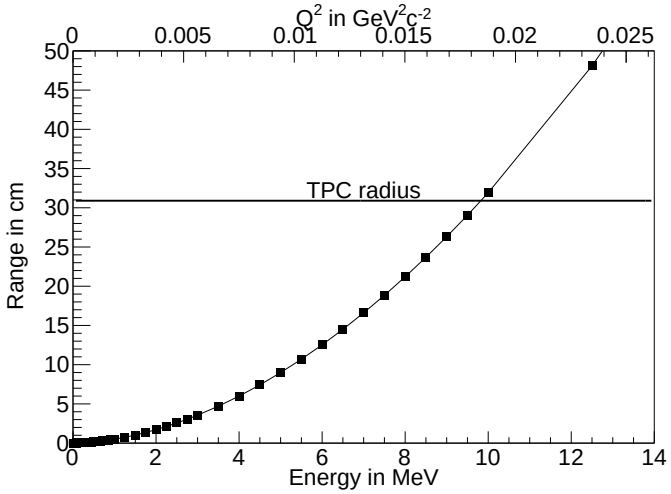

Figure 6.6: Range of protons in 20 bar hydrogen. The PSTAR-data is taken from [23] just scaled by a density of $8.3748 \times 10^{-5}\,\text{g cm}^{-3}$ [24] and the pressure.

In figure 6.7 the energy loss of muons with 100 GeV c^{-1} is depicted simulated by TGeant based on the

models described in table 6.1. It is the energy lost in a single sensitive volume, i.e. 40 cm, at 20 bar.

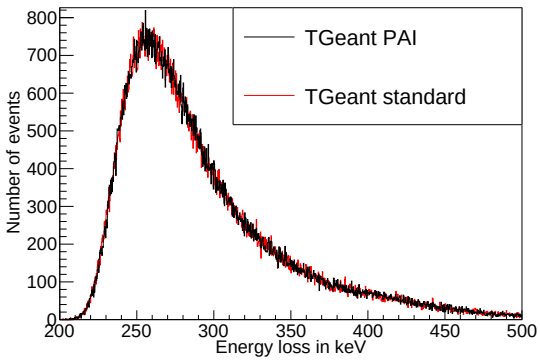

(a) The red curve shows the distribution coming from the models presented in table 6.1 for the energy loss of muons; the black curve is simulated by replacing the *Bragg*- and *Bethe-Bloch*-models from table 6.1 by the PAI-model.

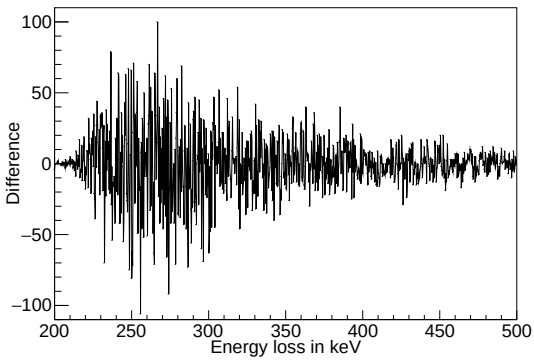

(b) Difference of the distributions shown on the left.

Figure 6.7: Energy-loss fluctuations of muons in a single TPC-volume, i.e. 40 cm, filled with hydrogen gas at 20 bar.

This energy lost by the muons will be background measured by the read-out of the TPC[5]. It will be distributed over the anode plane following the beam profile shown in figure 8.1 in chapter 8.
As both energy-loss simulations coincide following figure 6.7 one can deduce that the background created by muons is accurately simulated within the TGeant-framework when taking into account the results from section 6.1.2 in addition.
In TGeant protons are simulated wit energies up to approximately 10 MeV. Therefore they are stopped inside the TPC. The energy-loss models used in TGeant are the same as the ones used in the *Livermore*-model. As it describes the mean energy loss accurately as shown in section 6.1.2 the proton range will coincide with the PSTAR-database as well and the energy-loss simulation will be in good agreement with experimental data.

[5] A single muon will loose on average 290 keV in a single sensitive volume which is in agreement with 280 keV from [40]. As described in chapter 5 the beam rate in the experiment is planned to be 2 MHz. This will lead to a high energy deposition from the beam inside the TPC.

CHAPTER 7

Pad response functions

The TPC employed in the COMPASS++/AMBER proton charge-radius experiment will be equipped with a segmented pad read-out at the anodes. To optimize their geometry one needs to know their reaction to the drift of charges, in our case to electrons. In GARFIELD++ one can simulate the electron drift in the TPC and import weighting fields to calculate the induced currents. These currents correspond to the pad response functions and can be used to analyze the behaviour of the anode structure in the full simulation of the real experiment as it is done in chapter 8.

7.1 Implementation in ANSYS ®

To extract the pad response with the help of GARFIELD++ one first needs to hand over the real electric field in the detector as well as the weighting fields for the read-out electrodes one is interested in. The software package ANSYS ® (**AN**alysis **SYS**tem) [41] is suitable for the solution of static, electromagnetic problems like this. ANSYS ® can be used and controlled via a graphical user interface or from the command line with its "**A**NSYS **P**arametric **D**esign **L**anguage" APDL [42]. The weighting fields and real electric field will be extracted only for the induction zone, as the charges only start to induce the signals when they cross the *Frisch*-grid that separates the drift from the induction zone.
First of all, one needs to define the electric properties of the used materials, like conductivity and resistance. In the next step, one defines the overall geometry in form of single volumes representing all necessary components. In the case of the induction zone of the TPC, like it is done here, the *Frisch*-grid is replaced by a copper plate. This is done because the distance between the single wires is small. With the real *Frisch*-grid the computation time of the fields is quite high. In a distance of 1 cm to the metal plate the anode is placed which is made out of copper pads. These pads have a distance of 1 mm from each other [34]. Between the anode and the grid there is the hydrogen gas. The overall radius of the pad plane is 30.9 cm. The proposed anode geometry is shown in figure 7.1.
After the geometry implementation the single volumes are connected to the first defined media to define their electric behaviour. Then one can define the potentials that are applied to the different elements to form the weighting and real electric fields.
In our case that anode has a 90°-rotational symmetry. Therefore, only a quarter of the TPC is implemented and with the help of symmetry commands extended to the full TPC.
After the implementation, the single volumes are meshed to define single nodes where later on the potentials are calculated during the numerical solution in ANSYS ®. The solutions from ANSYS ®

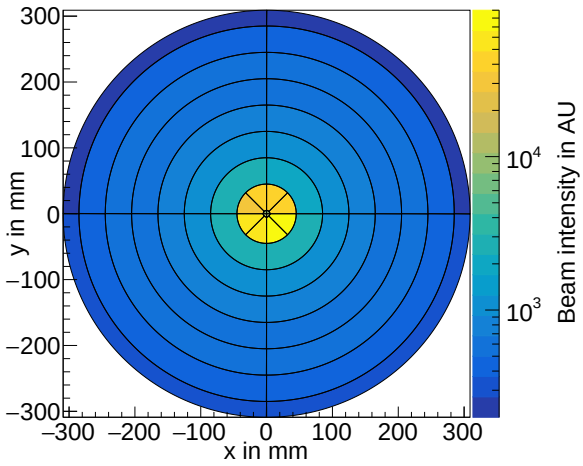

Figure 7.1: This is the anode structure as stated in the proposal [11]. The colour scale indicates the beam intensity as it is given in figure 8.1; the beam profile is projected onto the pad plane. The circular form is motivated one the one hand by the fact that the protons fly radially out of the center, and on the other hand by the similarity to the Mainz-experiment. Because of this similarity various calibrations can be adopted. In the Mainz-experiment the read-out of the TPC can be calibrated with a sharp pencil beam.

can be exported into four different files that are later read by GARFIELD++. One file has the definitions of the electric characteristics of the different materials in it, one defines the positions of the different nodes, one saves the voltages at these positions and the last defines the materials that are at the different nodes.

An example of such an ANSYS ® script is given in the appendix H.

7.2 Pad response simulation in GARFIELD++

To simulate a realistic response of the TPC to charged particles it is necessary to know the response for a given detector geometry to an electron. Here one can also make use of GARFIELD++ with its electron drift classes as well as its possibility to simulate signal induction.

To do so, one first needs to define the detector gas and its properties as shown in the appendix G. The field maps created with ANSYS ® can be imported in GARFIELD++ via the COMPONENTANSYS123-class as shown in the following:

```
ComponentAnsys123 *field = new ComponentAnsys123();
std::string elist = "ELIST.lis";
std::string nlist = "NLIST.lis";
std::string mplist = "MPLIST.lis";
std::string prnsol = "PRNSOL.lis";
std::string unit = "cm";
field->Initialise(elist, nlist, mplist, prnsol, unit);
field->EnableMirrorPeriodicityX();
field->EnableMirrorPeriodicityY();
```

The variables here are the four previously defined output files generated in ANSYS ®. As there are mirror symmetries used to describe the whole read-out zone of the TPC, one needs to activate the symmetries here as well. GARFIELD++ now calculates the electric fields from the potentials at the given nodes and their distances to each other.

To define a sensitive medium it is necessary to define which material in ANSYS ® is the one where the electrons are drifting.
The SENSOR-class takes care of the electric field in the detector as well as the weighting fields of the electrodes that are are going to be read out. The weighting fields are also solutions generated by ANSYS ® and are loaded in the following way:

```
Sensor *sensor = new Sensor();
sensor->AddComponent(field);
std::string electrode = "PRNSOL_Electrode.lis";
field->SetWeightingField(electrode, "electrode");
sensor->AddElectrode(field, "electrode");
sensor->SetTimeWindow(0, 0.5, 2600);
```

With the SETTIMEWINDOW-command one can define in which time interval and with which step size the signals are going to be read out. To extract the pad response the start time is set to 0, the time step size to 0.5 ns and the number of time bins to 2 600 so that the whole drift for the given pressure and electric field settings is contained. At this point one can define a shaping function to describe the following electronics. Here, no shaping function is used to extract the raw pad response functions without the influence of electronics. With this option one is able to further study the impact of different electronics.

Now every part to describe the detector is set up and one can start the electron drift with the AVALANCHEMICROSCOPIC-class that does the microscopic tracking of electrons with the help of MAGBOLTZ. As the pad plane consists of different pads one needs to do different simulations. But the only difference is the starting position in transverse direction of the drifting electron that needs to be above the pad of interest. The z-coordinate needs to be the longitudinal position of the *Frisch*-grid so that the whole induced signal is generated.

For every pad the average of 100 electrons is used as output. For a given electrode in a certain time bin one can retrieve the signal from the SENSOR via

```
sensor->GetSignal("electrode", time_bin);
```

The unit of the output is in standard GARFIELD++ units, i.e. $\mathrm{fC\,ns^{-1}} = \mu\mathrm{A}$ [38].

The starting positions of the electrons in transverse direction are uniformly distributed over the pad area. This is done to reduce the simulation time in the main simulations in TGEANT. The correct ansatz would be to import the weighting fields into TGEANT and to calculate the signals along the drift lines of the electrons for every single electron. An advantage of this way is that one can also calculate the signals of electrodes that are not hit by a drifting charge. But as this effect is quite small (cf. figure 7.3 and 7.4) already for the neighbouring electrodes (and will be even smaller for electrodes that are further apart), this would only lead to negligible corrections.
Instead of importing weighting fields and calculating signals in TGEANT the resulting pad response is included there (cf. chapter 8).

A summary of the workflow in ANSYS ® and GARFIELD++ is depicted in figure 7.2.

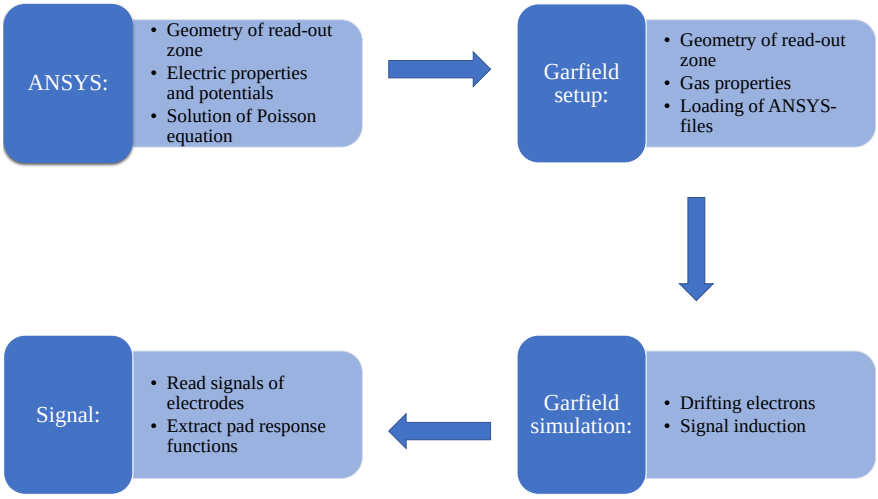

Figure 7.2: Summary of the workflow as it is done in ANSYS ® and GARFIELD++.

7.2.1 Electric and weighting fields from ANSYS ®

The basis of the simulations are the electric and weighting fields calculated by ANSYS ®. These are looked at in the following. In the figures 7.3 to 7.5 different components of the calculated weighting field are shown; the $E_{\mathrm{W},x}$-, $E_{\mathrm{W},y}$- and $E_{\mathrm{W},z}$-components above a pad of the second ring at $z = -4.5\,\mathrm{mm}$ in the TPC, as well as the z-dependence of the weighting field at a fixed transverse position. The figures 7.3 and 7.4 make use of the same color scale. One can clearly see that the weighting field is quite homogeneous above the pad the weighting field belongs to. It has only transverse components at the borders of a pad. But as the electric field in the TPC is along its symmetry axis, i.e. the z-axis, the $E_{\mathrm{W},z}$-component is the relevant one to calculate the induced signal. From figure 7.4 one can deduce that it is also very homogeneous above the pad (with $E_{\mathrm{W},z}\,(z = -4.5\,\mathrm{mm}) \approx 1\,\mathrm{V\,cm^{-1}}$), and is only varying at the edges. The weighting field also decreases quite fast if one has a look at the neighbouring pads. This leads to the fact that the signal induced in other pads is rather small.
In figure 7.5 the shape of the weighting field along the TPC symmetry axis at the center of a pad of the second ring is shown. One can see intervals in which $E_{\mathrm{W},z}$ is continuous but there are small steps in between these intervals. These steps are originated by the finite element method to solve the *Poisson* equation to calculate the electric field. To do so, ANSYS ® is meshing the whole setup and creating different elements and nodes on which the potentials are calculated. As these elements have different sizes the nodes have varying distances to each other leading to varying electric and weighting fields.

The calculated electric field for a pressure of 4 bar is shown in figures 7.6 and 7.7 for different coordinates above a certain anode again at $z = -4.5\,\mathrm{mm}$. The dependence of the E_z-component along the TPC-axis is depicted in figure 7.8 (the difference to the nominal value of $2\,\mathrm{kV\,cm^{-1}}$ is plotted; cf. table 5.1). The following discussions also hold for the electric field at 20 bar as it is only scaled by a factor of 5 coming from the two different pressures.

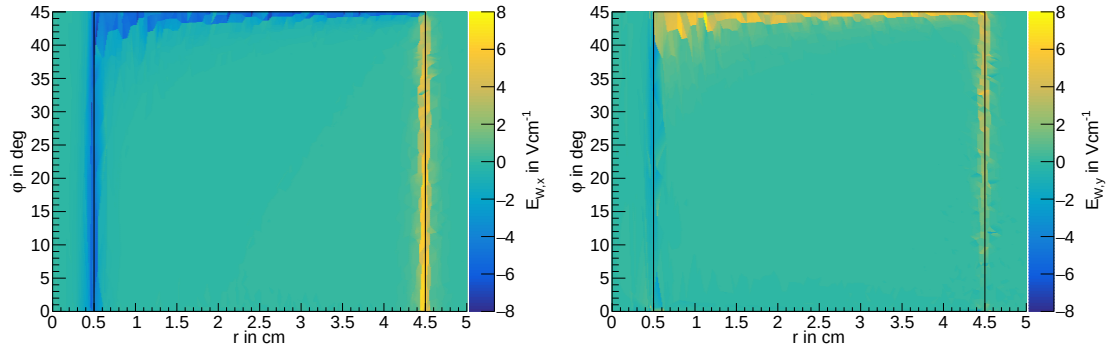

(a) $E_{\mathrm{W},\,x}$. (b) $E_{\mathrm{W},\,y}$.

Figure 7.3: $E_{\mathrm{W},\,x}$- and $E_{\mathrm{W},\,y}$-components of the weighting field of a pad of the second ring plotted in polar coordinates at $z = -4.5\,\mathrm{mm}$. The black lines indicate the borders of the pad. The colour scale is the same as in figure 7.4. The weighting field has no transverse components along the pad. At the boundaries it has a contribution because of the neighbouring pads.

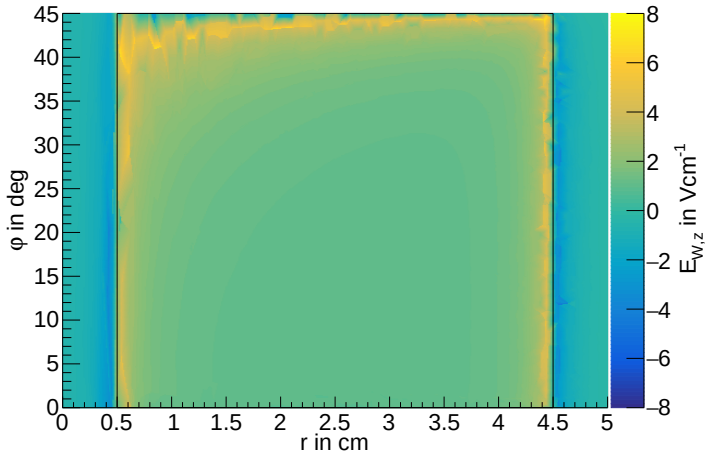

Figure 7.4: $E_{\mathrm{W},\,z}$-component of the weighting field of a pad of the second ring plotted in polar coordinates at $z = -4.5\,\mathrm{mm}$. The black lines indicate the borders of the pad. The colour scale is the same as in figure 7.3. The weighting field is very homogeneous over the pad. At the boundaries one has edge effects.

One can deduce that the electric field has only a component along the TPC-axis as the transverse components are compatible with 0 as long as one is looking at coordinates above an anode channel. Again, at the edges one has $E_{x,\,y} \neq 0$ because of the gaps between the different pads. Along the rotational-symmetry axis of the TPC the E_z-component is also quite constant. In figure 7.8 the difference of the electric field to the nominal value of $2\,\mathrm{kV\,cm^{-1}}$ is plotted. The variations are in the order of $0.1\,\mathrm{V\,cm^{-1}}$ corresponding to differences of about $0.1\,‰$. But here one can again observe discontinuities coming from the method to solve the *Poisson* equation to determine the electric field as described already for the weighting field when analyzing figure 7.5.

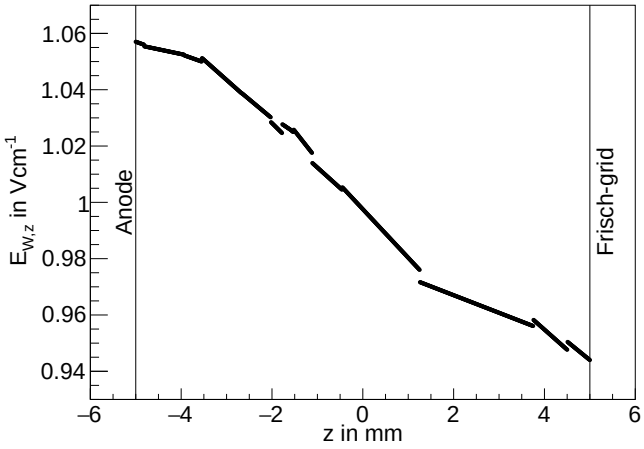

Figure 7.5: $E_{\mathrm{W},z}$-component of the weighting field along the TPC-axis at the center of a pad of the second ring, i.e. $r = 25\,\mathrm{mm}$ and $\varphi = 22.5°$.

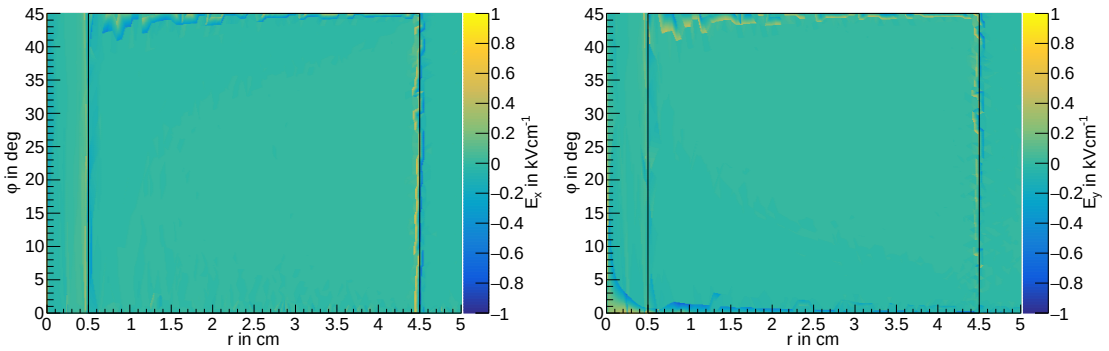

(a) E_x. (b) E_y.

Figure 7.6: E_x- and E_y-components of the electric field inside the TPC above a pad of the second ring plotted in polar coordinates at $z = -4.5\,\mathrm{mm}$ and 4 bar. The black lines indicate the borders of the pad. The colour scale is not the same as in figure 7.7 as E_x and E_y are around 0, while E_z corresponds to the nominal absolute value of $2\,\mathrm{kV\,cm^{-1}}$. The electric field has no transverse components along the pad. At the boundaries it has a non-zero contribution because of the gaps between the pads.

From the discussions up to now one can already conclude a few points:

- The drift velocity is the same for both pressure settings (cf. table 5.1 in section 5.2.2). As the weighting fields only depend on the overall geometry the pad response functions should be the same for both proposed pressure settings.
- The signals induced in neighbouring pads that are not hit by the drifting charge are negligible as the weighting field drops already for small distances away from the pad.

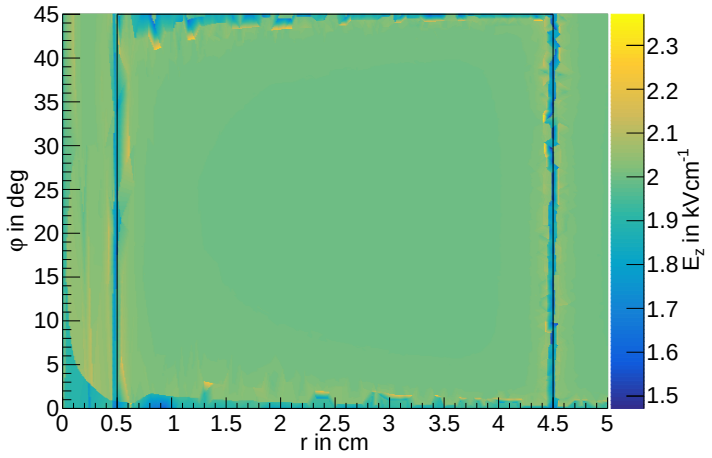

Figure 7.7: E_z-component of the electric field inside the TPC above a pad of the second ring plotted in polar coordinates at $z = -4.5$ mm and 4 bar. The black lines indicate the borders of the pad. The colour scale is not the same as in figure 7.6. The electric field is very homogeneous over the pad. At the boundaries one has edge effects.

- Based on the rotational symmetry of the read-out shown in figure 7.1 implies that every pad in a ring has the same response function.
- Generally one would expect different shapes of the pad response originating from the geometry of a certain pad.
  - The pads of the first ring, i.e. the most inner pads, are quarters of a circle with a radius of 5 mm.
  - All other rings consist of angular segments with a radius of 4 cm except the last ring which has 2.4 cm. Another difference is that the second ring is divided into eight pads but all others only into four.

7.2.2 Pad response for the proposed geometry

In figure 7.1 the initially proposed anode geometry is shown. For this case the induced signals for all rings are extracted at 20 bar. These are shown in figure 7.9 to 7.13. Here, the error bars represent the statistical error from averaging the 100 drifting electrons. The induced currents are plotted against the time. The data will be the basis for following simulations of the complete TPC response. The first (most inner) ring 7.9 is fitted with a polynomial, i.e.

$$I_{\text{ind}}(t) = \left(I_0 + at + bt^2 + ct^3 + dt^4 + et^5 + ft^6\right) \Theta\left(t_0 - t\right) ,$$

with the *Heaviside*-function Θ that is used to take into account the drift time t_0. After the charges reach the anode the induced current goes back to 0. All other rings are fitted by a simple parabola (again, with the *Heaviside*-function), i.e.

$$I_{\text{ind}}(t) = \left(at^2 + I_0\right) \Theta\left(t_0 - t\right) .$$

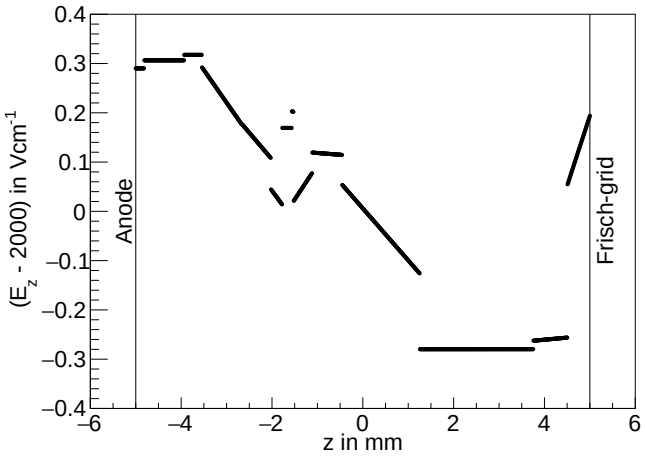

Figure 7.8: E_z-component of the electric field along the TPC-axis at the center of a pad of the second ring, i.e. $r = 25\,\text{mm}$ and $\varphi = 22.5°$. The difference to the nominal value of $2\,\text{kV}\,\text{cm}^{-1}$ at 4 bar is plotted. One can see that the differences are in the order of $0.1\,‰$. The discontinuities originate from the finite element method in ANSYS ® to solve the *Poisson* equation to determine the electric potential and field.

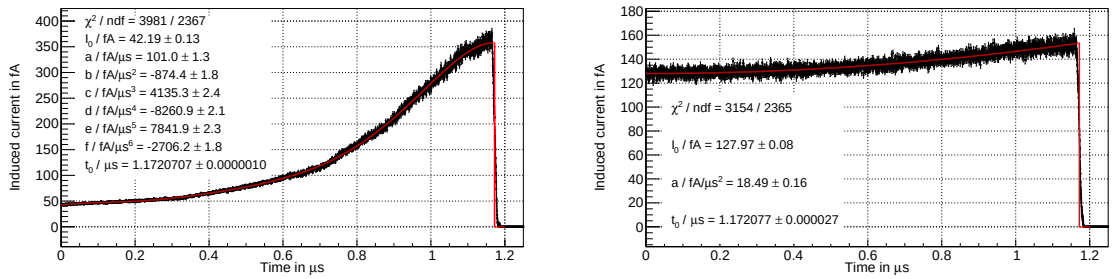

(a) Ring 1.

(b) Ring 3.

Figure 7.9: Pad response of the pads from the first (left) and third (right) ring.

These pad response functions do not have any physical motivation. They are just empirical parameterizations to describe the data for further studies of the overall TPC performance as done in chapter 8.

The extracted drift time is in all cases the same within 1 ns for values of 1.172 µs. Comparing this to $(1.1879 \pm 0.0010)\,\mu\text{s}$ coming from the drift velocity of $(841.8 \pm 0.7)\,\text{cm}\,\text{ms}^{-1}$ in table 5.1 (that are calculations from MAGBOLTZ) and a drift distance of 1 cm one can calculate a difference of 1.4 %. No signals have the sharp drop at the end as assumed by the *Heaviside*-function. The step is smeared out by the longitudinal diffusion that amounts to 4.6 ns at 20 bar for a drift distance of 1 cm.

With the chosen binning of 0.5 ns in the simulation one can clearly see the single collisions and therefore the stop and go motion of the electrons by the variation of the induced current in consecutive time bins.
Integrating the depicted signals over the whole drift time should yield the overall induced charge, in

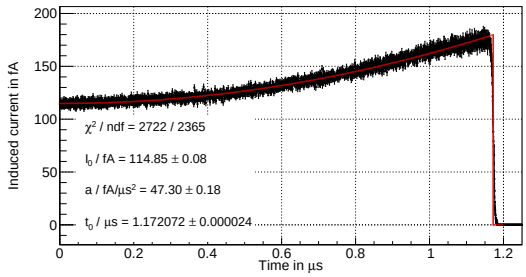

(a) Ring 2 pad 1.

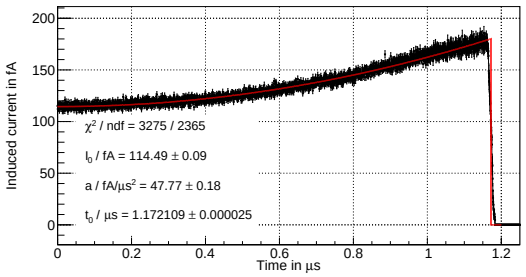

(b) Ring 2 pad 2.

Figure 7.10: Pad response of the pads from the second ring.

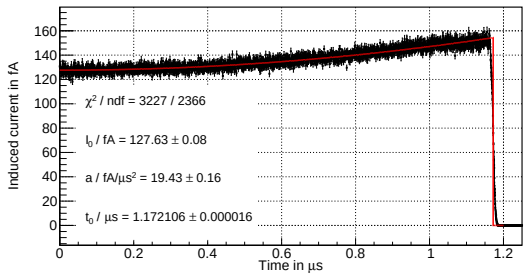

(a) Ring 4.

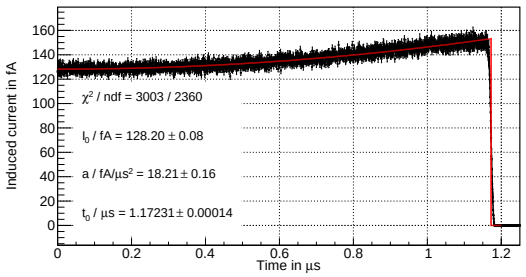

(b) Ring 5.

Figure 7.11: Pad response of the pads from the fourth (left) and fifth (right) ring.

our case the elementary charge e. This criterion can be used to judge the pad response functions as well as the fits. The integral results are shown in table 7.1. All are in agreement with e having deviations in the order of 1 ‰.

The signals for the third to the most outer ring are looking the same evaluating the fit parameters. This can be explained by the pad geometry as shown in section 7.2.1. All pads are quarters of a circle segment with a radius of 4 cm which is much larger than the gap between the pads of 1 mm. Therefore, the most field lines of the weighting fields of the different electrodes connect the pads with the *Frisch*-grid. Only the outer parts of the pads are connected with their neighbours. This is the reason why the pad response function of the ninth ring is also comparable to the others although its radius is smaller with 2.4 cm.

The pad response of the second ring is depicted in figure 7.10 exemplary for two different pads. With these one can judge about the rotational symmetry of the pad plane leading to the fact that all pads of a ring should have the same response.
Looking at the fits the results differ by 3 ‰ for the y-intercept I_0 and by 8 ‰ for the parameter a. From these one can conclude that the rotational symmetry is provided. As described in the beginning of this chapter the pad response functions will be used as input for simulations of the whole detector behaviour. This rotational symmetry will make the simulations faster as one only needs to know the

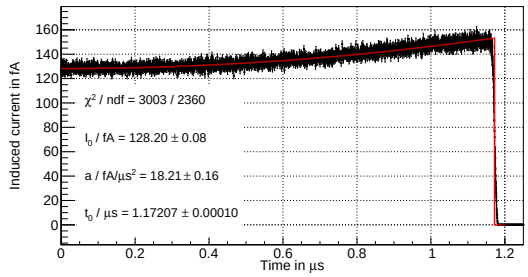

(a) Ring 6.

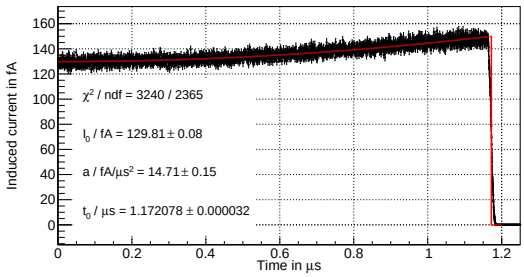

(b) Ring 7.

Figure 7.12: Pad response of the pads from the sixth (left) and seventh (right) ring.

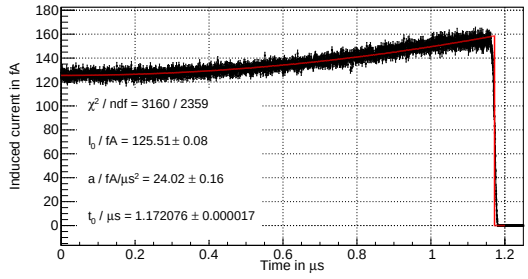

(a) Ring 8.

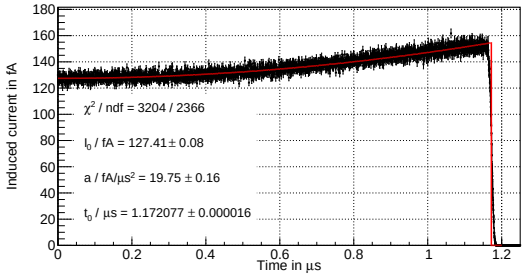

(b) Ring 9.

Figure 7.13: Pad response of the pads from the eighth (left) and ninth (right) ring.

actual ring to evaluate the pad response.

Very different from the results so far is the pad response of the most inner ring. Coming from its different geometry and being rather small compared to the pads of the other rings ($0.8\,\mathrm{cm}^2$ vs. $\geq 7.9\,\mathrm{cm}^2$) one can say that the majority of the signal is induced at the end of it, i.e. 25 % of the charge is induced approximately in the last 100 ns.

The example of an induced signal of a pad that is not hit during a simulation is shown in figure 7.14, i.e. the signal of a pad of the fourth ring. But here, the electrons drift down towards its neighbouring pad of the third ring. As one can deduce from the *Shockley-Ramo*-theorem (cf. section 3.3) the signal of an electrode that does not collect the drifting charge has a bipolar form.

Already for the pad next to the one that is hit, the signal is at least an order of magnitude smaller and drops even further for pads that are further away. Because of that the signals of pads that are not hit by any electron will not be taken into account in the TGeant-simulation (cf. chapter 8).

Ring	Q_{ind} in e
1	0.997 ± 0.014
2	0.99868 ± 0.00033
3	0.9982 ± 0.0004
4	0.9988 ± 0.0004
5	0.9985 ± 0.0004
6	0.9989 ± 0.0004
7	0.9989 ± 0.0004
8	0.9987 ± 0.0004
9	0.9983 ± 0.0004

Table 7.1: Results of the integration of the pad response functions over the drift time between *Frisch*-grid and anode that correspond to the overall collected charge in units of the elementary charge e. The result for the second ring is the mean value of the integrations of both figures in 7.10.

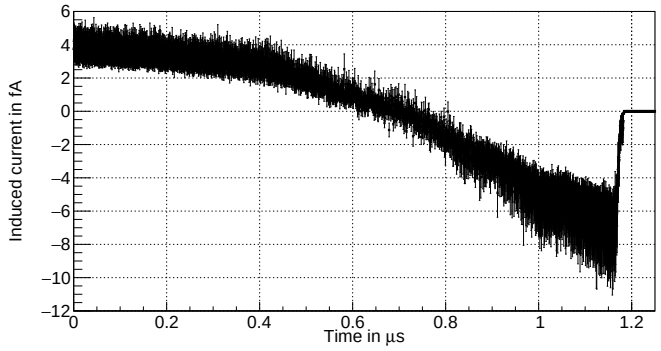

Figure 7.14: Induced signal of a pad of the fourth ring. The electrons drift down towards the neighbouring pad at the third ring. As one can see the signal is an order of magnitude smaller compared to the case where a pad is hit.

7.2.3 Comparison between 4 bar and 20 bar

There will be beam time and measurements at a hydrogen pressure of 4 bar to cover a low Q^2-range of the elastic scattering cross-section as well as to study systematic effects. Therefore, it is necessary to study the dependence of the pad response functions on the pressure and electric field settings.
As the drift velocity is the same for 4 bar and 20 bar (because of the constant reduced electric field) and the weighting field does not depend on the real electric field, the induced signals should look the same for both pressure settings. The induced signal for the 4 bar-case is shown in figure 7.15; for 20 bar it is depicted on right-hand side of 7.10.
The fit parameters are not the same in both cases but the overall difference is within 2 fA or 1 %. This different fit results but small deviations can be explained by the high correlation between the parameters a and I_0 of −0.69.
The main difference for both pressure settings is the longitudinal and transverse diffusion. As both are higher for 4 bar the whole signal is smeared out compared to the 20 bar signal. The step at the end is also not as clear as for 20 bar. These higher fluctuations originated from the diffusion are visible in

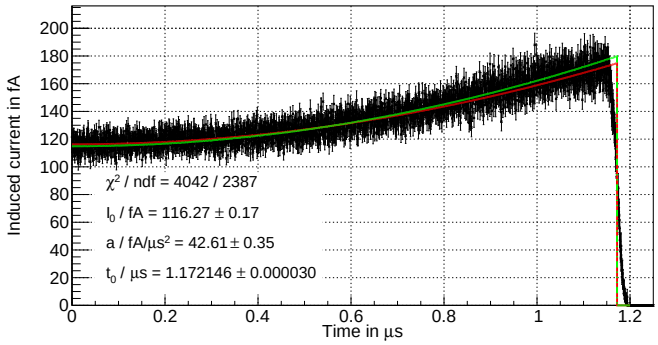

Figure 7.15: Pad response of a pad of the second ring at 4 bar. The green dashed-dotted line shows the fit of the second ring in figure 7.10 at 20 bar.

figure 7.15 through the larger error bars compared to the right-hand side of 7.10. The larger error bars lead to a less constrained fit. Because of that and the high correlation one can explain the difference between the signals at 4 bar and 20 bar.

7.2.4 Dividing a ring into more angular segments

A first step in having a look at different pad plane geometry options would be to divide a ring into more segments. This will lead to a better azimuthal resolution. Additionally, one can assume that the influence of the beam per pad of a ring decreases as the same amount of beam muons is distributed over more pads leading to less background and therefore to a better energy resolution of the TPC. Here, we are looking at the third ring. In the initially proposed geometry it is divided into four pads. Now it will be divided into eight as shown in figure B.2 in the appendix B. As long as the pads are still big enough (in terms of pad area) so that the transition to the neighbouring pads still plays no major role having more angular segments should not influence the pad response function. The case for a finer angular segmentation of the third ring is depicted in figure 7.16. It needs to be compared to the right-hand side of figure 7.9.

Here, one has again a high correlation between the parameters I_0 and a of -0.72 explaining the small difference of both fits. Figure 7.16 shows that the induced signal does not depend one the number of angular segments. But this has to be taken with a grain of salt as the number of angular segments has only been increased from four to eight reducing the pad size from 40.85 to 20.42 cm^2. Dividing it into more pads might influence the pad response at least if the size is in the order of the gap of the pads which is 1 mm. But this has not been studied as the number of read-out channels has been limited.

7.2.5 Changing the radial size of a ring

The next point to look at is the changing of the radius of the pads. As the TPC will be used as an active target one will have noise that is induced by the beam. This component critically depends on the pad size. By increasing the pad area the beam noise increases as well. It would be therefore feasible to look at smaller pad sizes in the central region of the TPC-read-out as here the influence of the beam is the largest (cf. figure 7.1). But one should keep in mind that the signal induced in a pad by the proton

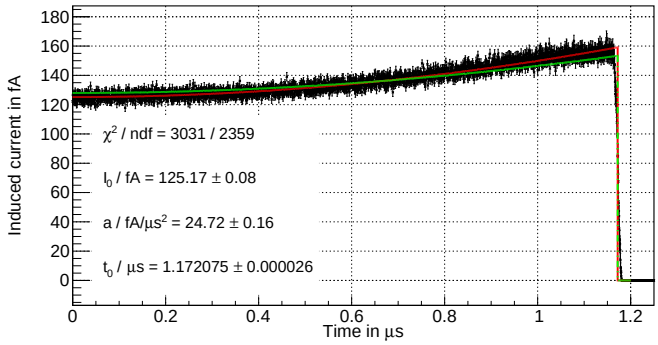

Figure 7.16: Pad response of a pad of the third ring at 20 bar. In comparison to the standard geometry the ring is segmented into eight segments as shown in figure B.2 in the appendix B. The green dashed-dotted line shows the fit of the third ring in figure 7.9 at 20 bar.

also decreases by dealing with smaller pads. In the outer region of the read-out (the beam is focused up to the second ring) the pad size will not influence the induced beam noise.
In figure 7.17 a signal of a pad from the third ring from pad plane B.4 at 20 bar is shown. The radii of the second to fourth ring are 2 cm compared to 4 cm in the initially proposed geometry 7.1.

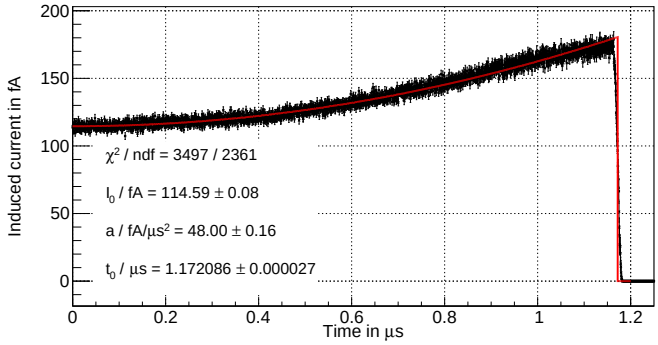

Figure 7.17: Pad response of a pad of the third ring at 20 bar. In comparison to the standard geometry the ring has a radius of 2 cm as shown in figure B.4 in the appendix B.

For such a geometry a change of the pad response is expected. The second and third ring are now at the radial position of the second ring in figure 7.1. There one has already a difference in the pad response between both rings. Therefore, it is expected that the induced signal changes. This change can be seen in figure 7.17 compared to the right-hand side of figure 7.9. The parameter a of the fit has especially increased by a factor of three. When looking at the induced signal for the second ring such an increase can be expected as the position of the third ring corresponds here to the outer half of the second ring in figure 7.1.

7.2.6 Rotation of a ring

In the initially proposed geometry the pads of the rings of the pad plane are aligned covering all the same angular range. The angular resolution could be improved using misaligned rings which will therefore be studied. For such a pad plane the azimuthal angular resolution should be improved compared to the aligned pad planes.
In terms of pad response functions the rotation of a ring with respect to the others should have a rather low influence. As it has been described already (cf. section 7.2.1), the components of the weighting field of an anode are very homogeneous above the pad (figures 7.3 and 7.4). This together with the fact that the transverse components of the weighting field are compatible with 0 implies that the most of the field lines of the weighting field connect the pad of interest with the *Frisch*-grid. Because of that a rotation of any ring should only lead to other edge effects at the pad corners. But it should have no influence on the weighting field lines going from the *Frisch*-grid to the anode which are responsible for the overall signal and therefore the response function of the pad.
In figure 7.18 the induced signal is shown for the fifth ring at 4 bar. Compared to figure 7.1 the rings are rotated by 20° with respect to each other.

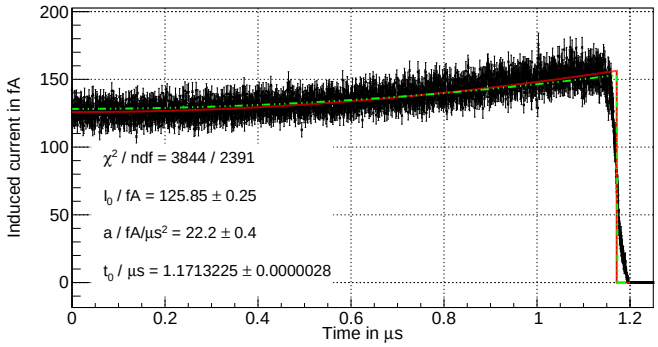

Figure 7.18: Pad response of a pad of the fifth ring at 4 bar. In comparison to the standard geometry all rings but the first two are rotated by 20° with respect to each other. The green dashed-dotted line shows the fit of the fifth ring in figure 7.11 at 20 bar.

As one can deduce from figure 7.18 the rotation of a ring does not influence the signal as it does not change the weighting field lines that connect the *Frisch*-grid with the pad one is looking at because of the rotational symmetry of the read-out geometry when looking at a certain ring.

CHAPTER 8

Simulation in TGEANT

The main simulation work to optimize the anode geometry of the TPC is done in the TGEANT-framework. The setup of the COMPASS++/AMBER proton charge-radius experiment has been implemented already including the TPC, the silicon tracker telescopes and scintillating fibers. The structure of the TPC is described in section 5.2. This description is the basis of the TPC-implementation. For the geometrical construction in TGEANT all necessary elements, like the gas vessel, the beam windows, the anodes, cathodes and *Frisch*-grids including all material descriptions, are used. But the whole project had to be extended by objects taking care of, for example, the electron drift or the signal induction inside the TPC. The different steps of the simulation chain and its output will be described in the following sections.

8.1 Simulation chain

As described already TGEANT is a GEANT4-based framework. Here the whole COMPASS-setup with its target and detectors is implemented. After the construction of the experimental setup the beam is initialized. Therefore TGEANT loads a so-called beam-file. This file is based on a simulation of the SPS beam group [43] and matches the real beam characteristics. There are the following properties listed:

- Particle ID; to discriminate beam particles from halo
- Position, i.e. x-, y- and z-coordinates
- Beam divergence, i.e. $\frac{\mathrm{d}x}{\mathrm{d}z}$ and $\frac{\mathrm{d}y}{\mathrm{d}z}$, as z is the nominal momentum direction of the beam
- Absolute value of the beam momentum

The beam distribution at $z = 1.3\,\mathrm{m}$ of the COMPASS coordinate system including halo is plotted in figure 8.1. There one can see that one works with a broad, asymmetric muon beam. The points far away from the center in 8.1 originate from beam halo. It is also visible as the low-momentum tail in figure 8.2. The actual properties of the beam particle in the TGEANT-simulation are drawn from the real beam characteristics.
With a defined beam GEANT4 starts to shoot particles in the direction of the target. Later on only events that have an interaction in the target are written out. Inside the TPC the muons loose energy

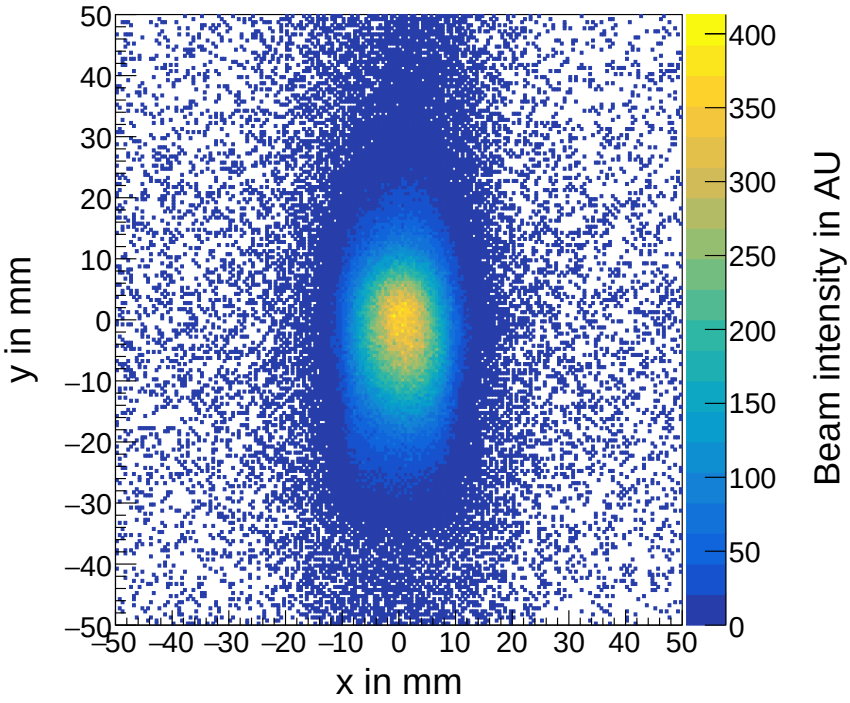

Figure 8.1: The distribution of the beam in the $x - y$-plane at $z = 1.3$ m in the COMPASS coordinate system.

due to processes described in section 6.2. This energy is either saved as deposited energy or new secondary particles are created.
The deposited energy along each step is used to create electron-ion-pairs. The electron drift is implemented as a separate class in TGeant. It is based on the parameters stated in table 5.1 in section 5.2.2.
First of all, the electron-ion-pairs are created inside the drift class. There the energy deposited in the Geant4-step is taken and divided by the work function W of hydrogen which yields the average number of electron-ion-pairs $\langle N \rangle = \frac{\Delta E}{W}$. The average energy to create an electron-ion-pair in hydrogen is 37 eV. This value is taken from [44, p.2 table 1]. The actual number of primary electrons follows a certain probability distribution that specifies the probability to create a certain number of primary electrons at a given energy-loss. In the TGeant-simulation the number of electrons k is drawn from a *Poisson*-distribution with mean $\langle N \rangle$:

$$\frac{\langle N \rangle^k}{k!} \exp\left(-\langle N \rangle\right) .$$

The positions of the primary electrons are uniformly distributed along the Geant4-step. This description is not quite correct but a good approximation. This can be justified by the help of figure 8.3. The mean free path of ionisation λ in 20 bar hydrogen gas is in the order of 50 µm. For pad sizes that are in the order of cm one is not able to see distinct clusters. So the microscopic, spatial distribution of the primary electrons is of no huge concern.

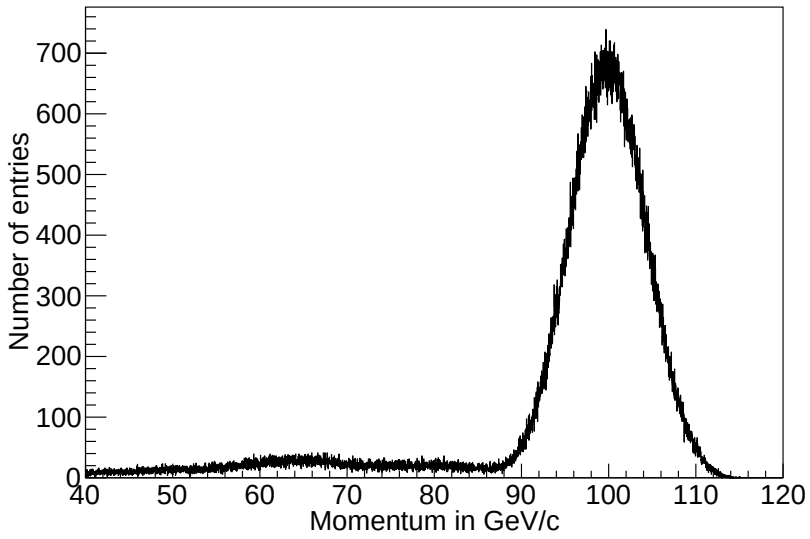

Figure 8.2: Here, the beam momentum distribution is plotted which is read by TGeant. The low momentum tail originates from the halo. The nominal momentum of the muon beam is 100 GeV c^{-1}.

All electrons then drift towards the *Frisch*-grid that is at z_{grid}. The transverse coordinates are drawn from a *Gauss*-distribution with a mean that is equal to the start point the actual electron and a standard deviation that depends on the drift distance $|z - z_{\text{grid}}|$ and can be calculated by multiplying $\tilde{D}_{\text{T}}$ from table 5.1 with $\sqrt{|z - z_{\text{grid}}|}$. After the drift the z-coordinate of the electron corresponds to the z-position of the *Frisch*-grid. The drift time is drawn from a *Gauss*-distribution, too. Here, the mean is calculated by

$$t_{\text{drift}} = \frac{\left|z - z_{\text{grid}}\right|}{v_{\text{drift}}},$$

and the standard deviation due to longitudinal diffusion by

$$\sigma_{t_{\text{drift}}} = \frac{\tilde{D}_{\text{L}}}{v_{\text{drift}}} \sqrt{\left|z - z_{\text{grid}}\right|},$$

where $\tilde{D}_{\text{L}}$ is the reduced longitudinal diffusion coefficient and can be again taken from table 5.1. The time that is drawn is then added to the creation time of the charge.
After reaching the *Frisch*-grid the signal induction of the electrons starts. To calculate the actual signals, one first needs to know at which electrode a certain electron arrives. For that two classes are introduced: the T4TpcPad- and T4TpcPadPlane-class. A pad has the following properties:

- Channel number or pad-ID
- Minimal and maximal radius
- Minimal and maximal azimuthal angle

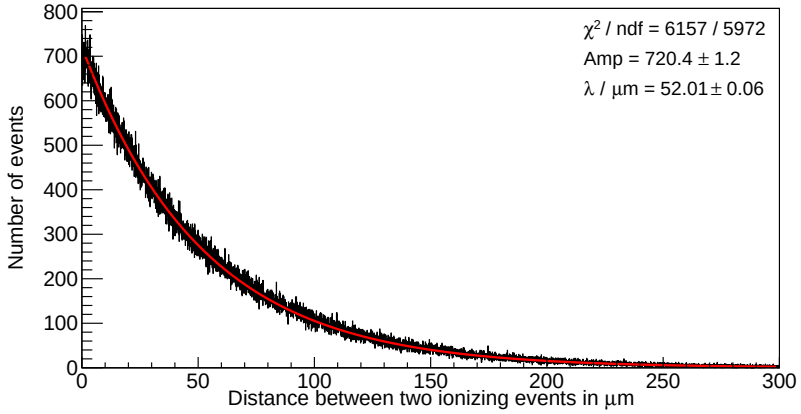

Figure 8.3: Garfield++-simulation of the passage of muons with 100 GeV c^{-1} in 20 bar hydrogen gas. Here, the distance between two ionizing collisions is plotted. The distribution is fitted with a single-exponential; that yields an average distance between two collisions, which is the mean free path of ionization and excitation, of $(52.01 \pm 0.06)\,\mu m$. As Garfield++ is doing a linear-pressure scaling, the mean free path of muons in 4 bar is a factor of 5 larger related to the density.

These properties are defined for every pad in the pad plane. All implemented pad planes can be found in the appendix B.
With these classes one is able to transform the x- and y-positions of the electrons into pad-IDs. For every pad the number of electrons collected by it as well as the corresponding start time (time at which the electron is at z_{grid}) is saved.
The pad response described in chapter 7 is also included in a separate class. Because of the rotational symmetry of the pad plane, the pad response functions are connected to the different rings and defined as ROOT TF1-functions.
For every pad, the pad response functions are then evaluated. By taking the start time of each collected electron the signals from all electrons are summed up in the relevant signal time between 0 and 100 µs. A single electron only contributes in the range $[t_{\text{start}},\, t_{\text{start}} + \Delta t]$ with Δt being the drift time in the induction gap of approximately 1.19 µs. The resulting overall signal is sampled with a 25 MHz-clock which corresponds to the expected sampling time of the experiment. The starting time of the sampling is drawn randomly out of the first 40 ns of the signal. In addition to the signal induced by all collected electrons, electronic noise is added.
After calculating all signals and adding the electronic noise, the output of every pad is shaped by the read-out electronics. The used shaping function is depicted in figure 8.4.

The shaping is done numerically by a ROOT TF1Convolution. It adds 10 µs to the overall signal. This time corresponds to the time it takes until the shaping goes back to zero.

As described above the whole signal is calculated over $\approx 100\,\mu s$. This time can be explained by the following:
In the simulation, pile-up is generated in a range from −100 to 100 µs. These ±100 µs are motivated by the drift time of electrons that are created at the cathode and need to drift 40 cm. The muons generate signals in a time range from 0 to 100 µs due to the drift time (the muons create electron-ion pairs

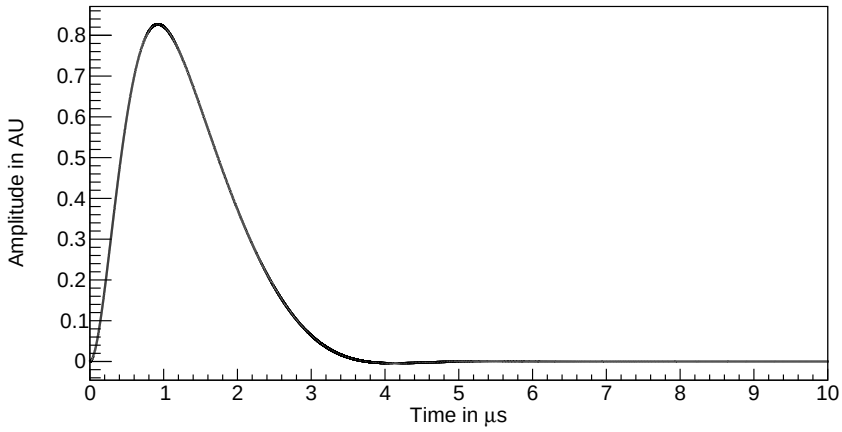

Figure 8.4: This is the function with which the pad signals from the TPC are convoluted. This function represents the behaviour of the read-out electronics [45].

nearly instantly over the whole volume). The convolution of these two rectangles, i.e. the first one from −100 to 100 µs and the second from 0 to 100 µs, leads to a trapezoid. The leading edge of this trapezoid is between −100 µs and 0 and the trailing edge from 100 to 200 µs. Between 0 and 100 µs one has a constant signal from the pile-up muons. Taking into account the beam rate of 2 MHz this pile-up signal is created by approximately 400 muons. This background needs to be taken into account in the simulation as the muons loose energy in the hydrogen gas and create electron-ion pairs that smear out the real signal as it can be seen for example in the figures 8.12. A trigger signal is assumed on the beam to locate the proton signal.
The TPC response is finally simulated taking into account the realistic beam description in terms of position and momentum spread and the beam rate of 2 MHz. The protons are generated with a fixed momentum transfer in each simulation, but with different Q^2-values to analyze for example the dependence of the energy resolution on the momentum transfer.
A summary of the simualtion is depicted in figure 8.5.

8.2 Electronic noise

During a test run at CERN in 2018, extensively described in the Master thesis of Martin Hoffmann [46], an energy calibration of the prototype-TPC was conducted. This was done by placing an ^{241}Am α-source with an energy of 5.486 MeV in front of a certain pad while there was no beam. That means that pads that were located far away from the source have recorded pure noise events originating from their own capacities and the electronics that were reading out the pad signals. The layout of the segmented anode can be seen in figure 8.6. The α-source was located at the cathode directly above pad 7.
The data has been analyzed for different pads that have not measured any of the α-signal with a tool provided by A. Dzyuba [45]. An example of the recorded noise values is depicted in figure 8.8. This is the data for anode 66.
If one does the projection for different anodes, one can evaluate the noise behaviour for varying pad sizes. This is shown in figure 8.9. For a fixed pad size the extracted noise values are plotted as well as

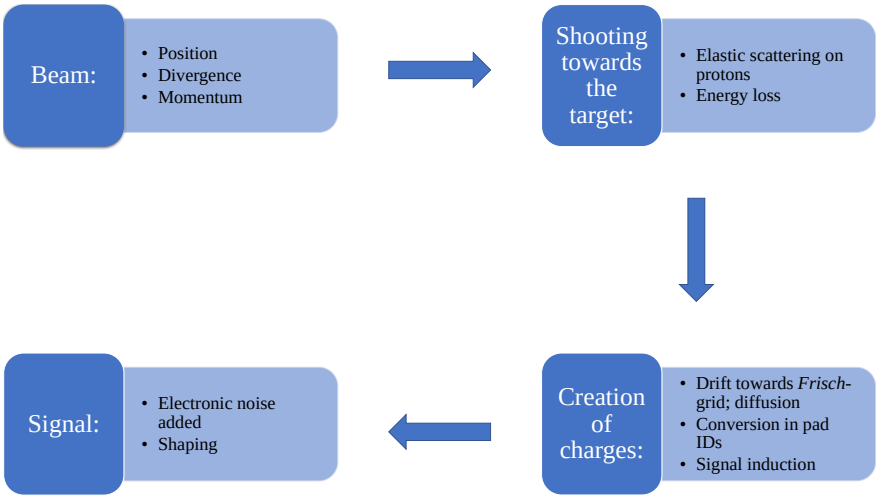

Figure 8.5: Summary of the simulation chain as it is in the TGEANT-framework.

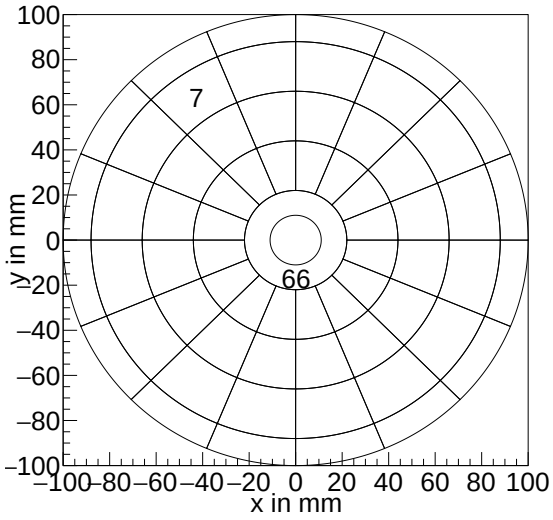

Figure 8.6: Layout of the anode used in the test run at CERN in 2018. Modified after [46].

the mean one gets from all of these.

Figure 8.9 does not show any dependence on the pad area as one would expect as the capacitance of the electrode increases with increasing size. A higher capacity leads to a higher noise; i.e. $C \propto A$. But this effect seems to be small here. This can be explained if the overwhelming contribution to the noise comes from the read-out electronics. That the electronics are responsible for the main part of the noise can be shown with the help of figure 8.10. In the proposal it is stated that one deals with low-noise amplifiers with a noise in the order of 20 keV [11]. This value can be checked by integrating different noise events over a typical time of 6 µs (this is also the typical length of a proton signal as shown in the analysis). The mean value should be close to 0 and the width should be close to 20 keV. The starting

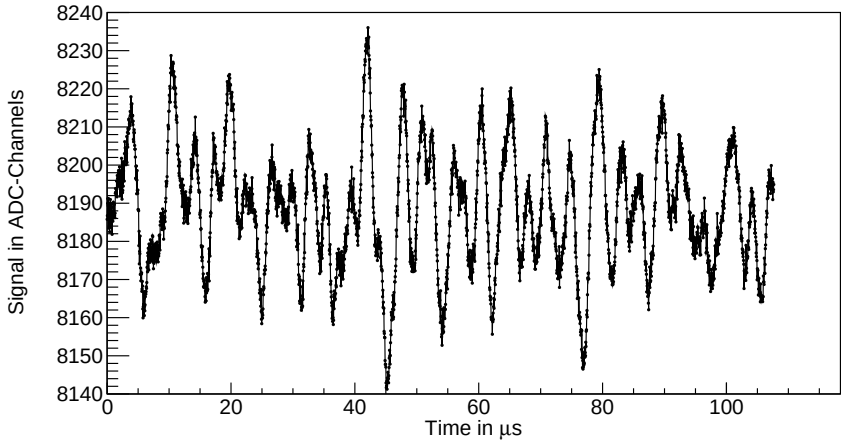

Figure 8.7: Recorded noise signal of anode 66 from the test setup. The signal is measured over 2 692 time bins, one bin corresponds to 40 ns and 1 ADC−channel corresponds to 3.2 pA. Because of the short integration time one measures directly the current [34]. The data points are simply connected by a spline to make it easier to follow the signal. Here, one can clearly see a micro-structure in the signal.

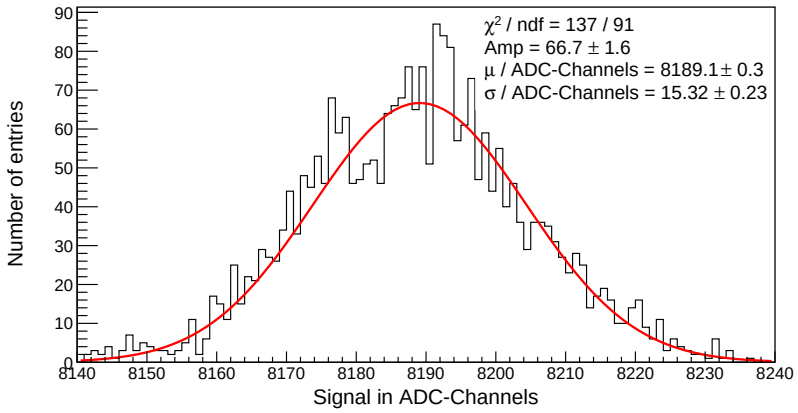

Figure 8.8: Projection of the noise values from the shown signal 8.7. The standard deviation is taken as the noise value which is then plotted in figure 8.9 for different anodes.

time of the integration is uniformly distributed over the whole signal. These signals look like the one shown in figure 8.7. With the help of the extracted calibration factor[1] of 3.2 pA ADC−channel^{-1} to transform the channel numbers of the ADC into physical currents and therefore integral results into energies, one measures a mean agreeing with 0 (after a baseline shift) and a standard deviation of (23.68 ± 0.08) keV. That value is slightly larger than the proposed one of 20 keV showing that there are other noise contributions as well as capacitive coupling of the different anodes. Besides other noise sources the electronic noise is determined with a shorter integration time [34, 45]. Additionally, the used read-out from the test run might be replaced by newer electronics.

[1] The way how this value is calculated is explained in section 9.

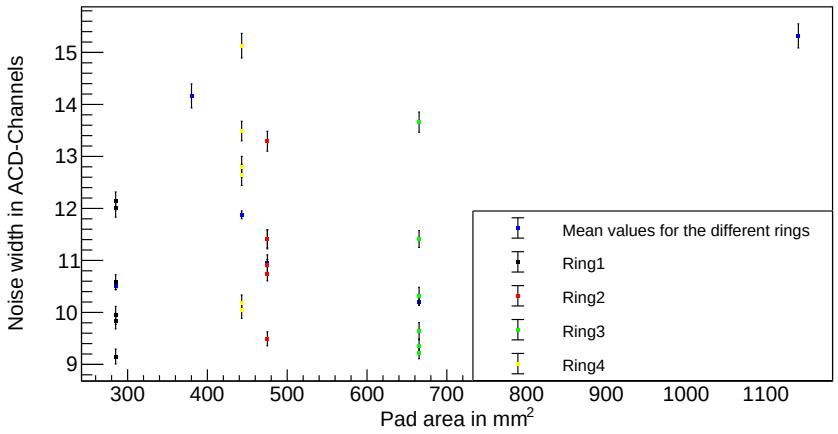

Figure 8.9: Recorded noise of different pads in the test setup. The standard deviation is plotted for different pads in a ring, as well as the average for every ring. One cannot see a dependence on the pad area which would be expected if the electronic noise originates mainly from the capacity of the pad as the capacity increases with the area. This implies that the main contribution of the noise originates from the read-out electronics.

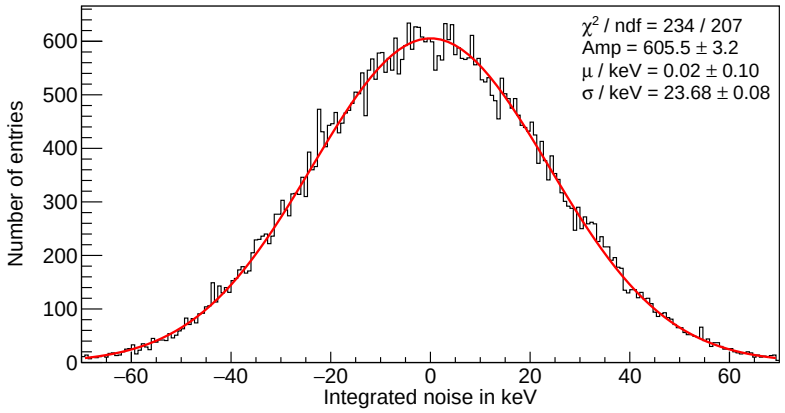

Figure 8.10: Contribution of the noise originated by the read-out electronics. This is estimated by integrating different noise signals over 6 µs where the starting point of the integration is uniformly distributed in the time interval of the signal one is looking at. The resulting noise value of (23.68 ± 0.08) keV is compatible with the stated value of 20 keV [11] as the electronics are not the only source of noise.

8.3 Pad signals from TGEANT

In this section the result of the TGEANT-simulation will be presented shortly.
In figure 8.11 one can see a pure noise event in the first sensitive volume in pad 1. On the y-axis the induced energy is plotted. This is just a quantity that is proportional to the induced current. The conversion is shown in equation (8.1),

$$E_{\text{ind}} = \frac{I_{\text{ind}} \cdot W \cdot t_{\text{sample}}}{e}, \tag{8.1}$$

where W denotes the work function of hydrogen with 37 eV and t_{sample} the sampling time of the readout with 40 ns. This does not change the way to extract the energy of a certain event. One still needs to integrate over the whole signal one is interested in.

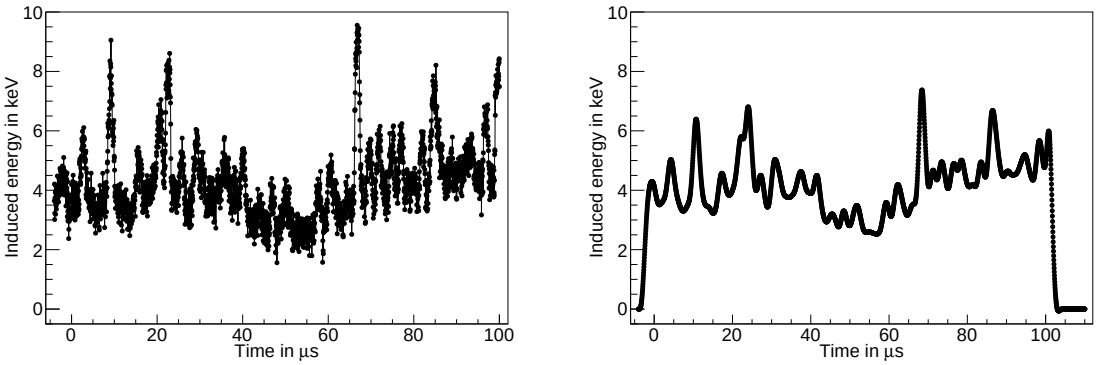

(a) The signal is not shaped by the electronics.

(b) This signal is shaped.

Figure 8.11: A noise signal of the first pad in the first sensitive volume of the TPC at 20 bar. The induced energy that is plotted, is proportional to the induced current and just scaled by the work function of hydrogen (37 eV) and the width of a time bin (40 ns).

The noise consists of a part originated by the read-out electronics[2]. The main contribution is coming from the so-called beam noise that is responsible for the baseline to be at around 1 keV in each time bin. In figure 8.11 the difference between the not-shaped and the shaped signal is shown, too. One can see that the amplitude of the signal is different, but the shaping does not change the normalization, i.e. the integral over the signal that corresponds to the energy of a certain event.

In figure 8.12 the signal (at 90 µs) of a 5.33 MeV-proton[3] (corresponding to a momentum transfer of 0.01 GeV^2 c^{-2}) crossing pad 11 in the first sensitive volume in the TPC is depicted. Also here the shaped and the not-shaped ones are shown just for comparison purposes. One can only see a part of the proton signal as it crosses other pads too along its track. This means that one needs to integrate over the signals of the pads belonging to the proton track to extract the full kinetic energy of the particle. Here, one can as well see the 10 µs that are added to the signal because of the shaping.

[2] The part coming from the pad capacitance is neglected as its contribution is small compared to the noise of the read-out.

[3] This is the kinetic energy of the proton.

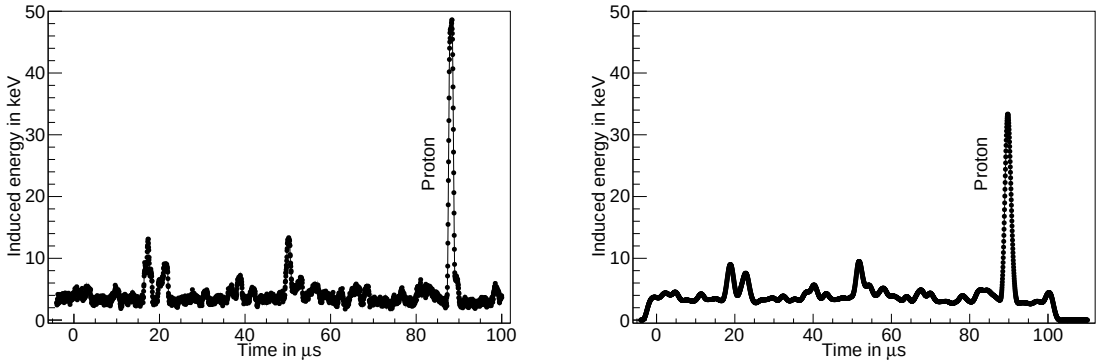

(a) The signal is not shaped by the electronics.

(b) This signal is shaped.

Figure 8.12: A proton signal in pad 11 in the first sensitive volume of the TPC at 20 bar. The proton has a kinetic energy corresponding to a momentum transfer of 0.01 $\mathrm{GeV}^2\,c^{-2}$. This is only a part of the full proton signal as it crosses other pads as well. The induced energy that is plotted, is proportional to the induced current and just scaled by the work function of hydrogen (37 eV) and the width of a time bin (40 ns).

CHAPTER 9

Analysis and results of the data from TGEANT

This chapter deals with the analysis of the output of the TGEANT-simulations described in chapter 8. First, the applied cuts are described as well as the reconstruction of the proton. Finally, different criteria like energy and angular resolution are used to determine the performance of the different implemented geometries.

9.1 Applied cuts and reconstruction

9.1.1 Cuts

Generally, the output-file of a simulation is a **.tgeant**-file[1] that can be read afterwards by the **CO**MPASS **r**econstruction **al**gorithm CORAL [47] based on ROOT. It takes information of the used detector setup given in an external so-called **detectors.dat**-file to process the raw data. The output of CORAL is a **m**ini **D**ata **S**ummary **Tree** mDST-file containing information of the detectors like tracks and vertices. With this information the program is able to reconstruct clusters, vertices and especially tracks for events that are handed over.
The output can be read by the framework called **PH**ysics **A**nalysis **S**oftware **T**ools PHAST. The first step in PHAST is to load all the events and to apply corresponding cuts to filter out good events. Here, several cuts on the Monte-Carlo values are applied. First of all, it is looked on the z-coordinate of the Monte-Carlo vertex z_{MC}. This value needs to be between the cathode and the anode of the corresponding sensitive volume of the TPC. Therefore, a cut of

$$z_{\mathrm{min}} + 1\,\mathrm{mm} < z_{\mathrm{MC}} < z_{\mathrm{max}} - 25\,\mathrm{mm}$$

is chosen. This is done to filter out the cases in which a proton created in the gas passes through the anode or cathode. Another reason is that there are protons generated in the copper electrodes flying into the sensitive volume. Even if it would be physically possible that such low energetic protons pass through the copper or are ejected out of it they have already lost so much energy that cannot be retrieved. So these are events one should exclude. The second criterion is the radial position of the incoming and the scattered beam at the beam windows of the TPC. Such a cut is applied to reduce the effect of multiple scattering of the beam muons in massive material. Because of that one chooses

[1] It is a compressed text-based file that contains information about the simulated events like detector hits.

$$r_{\mathrm{MC}} < 35\,\mathrm{mm}\,,$$

what corresponds to the radii of the beam windows of the TPC. During the analysis further cuts on the reconstructed data are used, for example on the duration of a proton signal. These are explained during the following analysis. After these cuts have been applied to the data a fraction of ca. 90 % has survived as shown exemplary in figure 9.1. As stated before, an event where the beam does not hit the target, is not written out. Therefore, approximately 25 out of 1 000 events are lost in TGEANT.

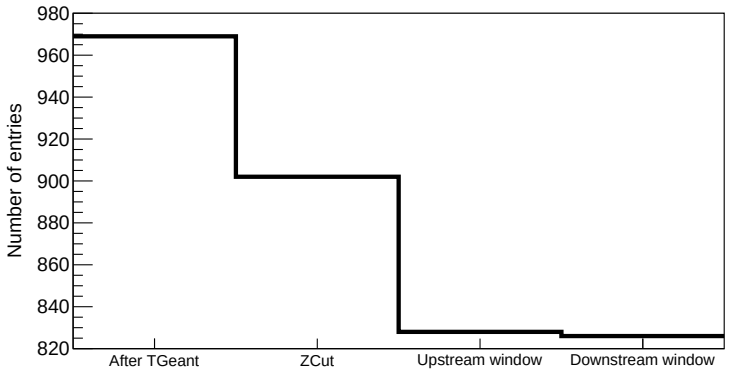

Figure 9.1: Number of events that survived the different cuts.

9.1.2 Signal reconstruction

The signals of the single pads are analyzed if the event passes the above mentioned cuts. After getting the proton signal in the shown 100 µs the baseline is calculated. The determined baseline is subtracted from the pad signal. After that two first order polynomials are fitted at the leading and trailing edge of the signal between 30 to 80 % of the maximum. Extrapolating these linear functions down to the baseline give the start and end time for the integration to extract the overall induced charge and deposited energy at the position of the analyzed pad. As the shaped signal has long tails and an undershoot coming from the read-out electronics the start time for the integration is 1.3 µs before the calculated intercept of the linear function with the baseline, and the end time is 2.7 µs after the estimated end. By summing up the entries of the time bins between start and end one can then calculate the deposited energy. All this is depicted in figure 9.2. With the integrated signals another cut is applied. It is required that signals have a duration between ca. 6 µs and 8 µs (cf. table 9.1).

Because of the segmented pad planes one needs to extract the track of the proton in order to get its full kinetic energy. The tracking algorithm is explained in [46] and will only be discussed shortly. An exemplary track is depicted in figure 9.3.

As the energy loss of a charged particle increases with decreasing momentum the energy deposition is maximal at the end of the particle's track according to BETHE-BLOCH. This is known as the *Bragg*-peak.

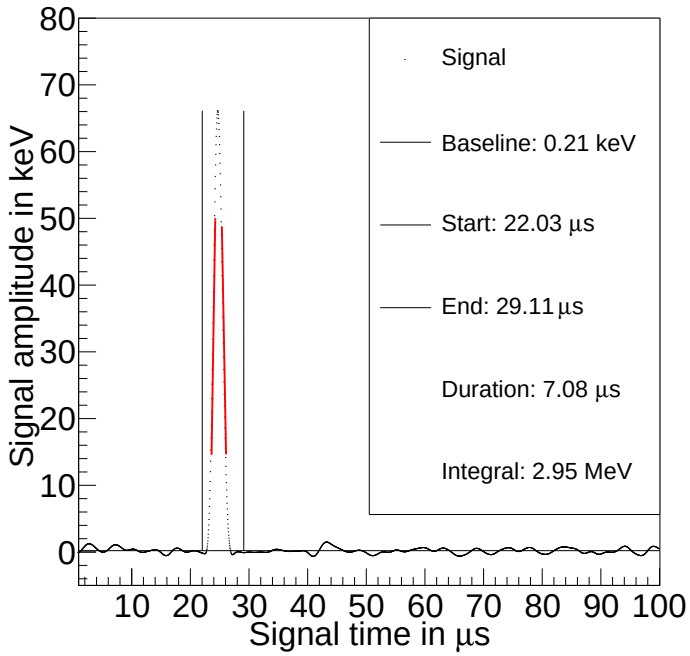

Figure 9.2: Integration of a recorded event in pad 29 of pad plane PRM6 in the second sensitive volume of the TPC. The momentum transfer in this case was $0.016\,\mathrm{GeV}^2\,c^{-2}$.

Therefore, the pad with the highest energy in an event should be the point where the proton is stopped. This pad is taken as a start point for the track finding. From there its neighbours are checked. Now, another cut comes into play. It is necessary that hit pads need to have similar times as they record the same proton. So one should require time coincidence of neighbouring pads if they are both hit. Therefore, it is needed that hit pads have a start time of their signal within the stated range in table 9.1 relative to the start time of the pad that recorded the highest energy.

p in bar	Duration in µs	Relative start time in µs
4	6.6 to 7.6	−2.0 to 2.0
20	6.6 to 7.6	−2.0 to 2.0

Table 9.1: Cuts on the duration of a proton signal as well as the start time of signals in other pads relative to the start time of the one with the highest energy. The relative start time takes into account the distance between the pads and therefore the time the proton takes to reach the other one. These cuts are applied if the proton is confined in the TPC. The motivation for these cuts is depicted in the appendix D.

As one only knows the position of the proton in terms of pad coordinates it is worked with the mean radius and angle, so the central position of the pad[2]. In the case that more pads on a ring are added to the cluster the angular information of this ring is calculated by a weighted mean $\bar{\varphi}$, i.e.

[2] If a pad is hit, the real position is smeared out by uniform distributions from the minimal radius and angle to the maximal ones of the pad.

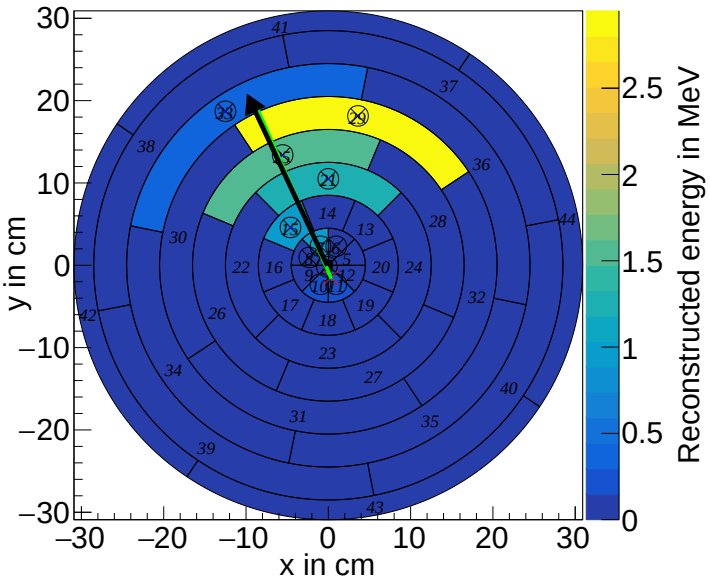

Figure 9.3: Example of a reconstructed proton track with pad plane PRM6 at 20 bar and a momentum transfer of 0.016 GeV^2 c^{-2}. The signal of pad 29 is depicted in figure 9.2. The red cross represents the simulated interaction between. The green crosses are the simulated steps of the proton, while the black arrow indicates the reconstructed track of the proton. The pads that are added to the proton track are marked with a cross around the pad-IDs. A circle around the pad number marks a pad which passes the applied cuts but is not added to the track due to the continuity requirement.

$$\bar{\varphi} = \frac{\sum_i E_i \varphi_i}{\sum_i E_i},$$

with E_i being the calculated deposited energy of pad i and φ_i its mean angle[3]. This center of gravity consists in most cases of two pads as the protons fly radially out from the center of the TPC more or less perpendicular to its symmetry axis. After all hit pads are clustered, the proton track is fitted if at least three different rings are in the cluster.
To estimate the azimuthal angle φ of the proton all mean values of the pads belonging to the proton track are used, i.e. $\bar{r}$ and $\bar{\varphi}$. The angle φ is extracted from a fit in polar coordinates, i.e.

$$\Delta\varphi\,(r) = \varphi\,(r) - \alpha = \begin{cases} \arccos\left(\frac{d}{r}\right), & \text{for } 0 < \Delta\varphi < \pi \\ -\arccos\left(\frac{d}{r}\right), & \text{for } -\pi < \Delta\varphi < 0 \end{cases},$$

with d being the minimal distance to the center of the read-out geometry and α the angle with respect

[3] The azimuthal angle φ indicates the transferred momentum in the xy-plane for the muon beam going in the z-direction.

to the normal vector as shown in figure 9.4.

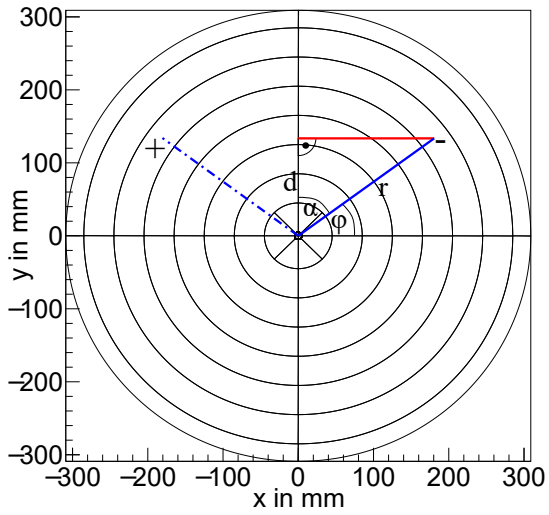

Figure 9.4: Reconstruction of the azimuthal angle φ of the proton. Based on [46].

9.2 Results

In TGeant different momentum transfers have been simulated. These are 0.001, 0.0025, 0.004, 0.008, 0.01 and 0.016 GeV^2 c^{-2} for 20 bar and 0.001, 0.0025, 0.004, 0.006 and 0.008 GeV^2 c^{-2} for 4 bar. These values correspond to the ranges in which it is planned to extract the elastic scattering cross-section.
The implemented and tested pad planes are shown in the appendix B. As described in chapter 7 different options are tested while keeping the proposed circular form of the anodes. Besides the proposed geometry, four other options are tested. Two of these options have a finer angular segmentation of the third (called PRM2[4]; left figure of B.2) and of the third and fourth ring (called PRM3; left figure of B.2) compared to the standard geometry in figure 7.1. The fourth option is characterized by a reduced radial size (2 cm instead of 4 cm) of the second to fourth ring (option PRM4; left figure of B.4). The missing radial size to have an overall radius of 309 mm is added to the two outer rings 3 cm each. The fifth option (PRM9; left figure of B.5) has also smaller radii of the rings two to four. But here the radial size of the second ring is chosen to match the radial cut done in the data analysis of 3.5 cm. The third and fourth ring have a radius of 2 cm again. The missing 7 cm are now added to the same amount to the seventh and eighth ring. In addition, the third ring is divided into eight angular segments. For all these pad planes similar ones are implemented. Here the rings are rotated with respect to each other. These rotations are characterized by the fact that a certain ring halves the segments of another inner or outer one having as less overlap as possible. With aligned rings one would expect a angular resolution in the order of

[4] It is called PRM just because of the abbreviation for proton radius measurement.

$$\frac{90°}{\sqrt{12}} \approx 26°\,.$$

coming from the fact that the angle is uniformly distributed over a pad when it is hit[5].

Following these geometries one can conclude a few expectations for recorded proton tracks going radially out from the center of the TPC:

- A finer angular segmentation should lead to less beam noise as the same amount of muons is distributed over more pads. It should also have an effect on the overall angular resolution of the TPC. One should keep in mind that an increase of the number of pads leads to an increase of the electronic noise.
- A reduction of the radial size of a ring does not affect the beam noise as the proton crosses more pads compared to the situation with larger radii. All in all the number of beam muons is again distributed over more pads but one sums up the contributions from all these pads. The reduction of the radius in the center should be advantageous for the track fitting of the proton. As more than three rings are crossed with smaller momentum transfer (again compared to the case of no reduction) the extraction of the track angle of the proton is already possible at smaller Q^2.
- A rotation of the rings with respect to each other should improve the angular resolution of the TPC without having more read-out channels.

For all these settings the energy as well as the azimuthal track angle is reconstructed. The differences to the MC-truth values is fitted with *Gaussian*-distributions giving mean differences and standard deviations which correspond to the energy or angular resolution. Two of these histograms are depicted exemplary in figure 9.5 and 9.6.

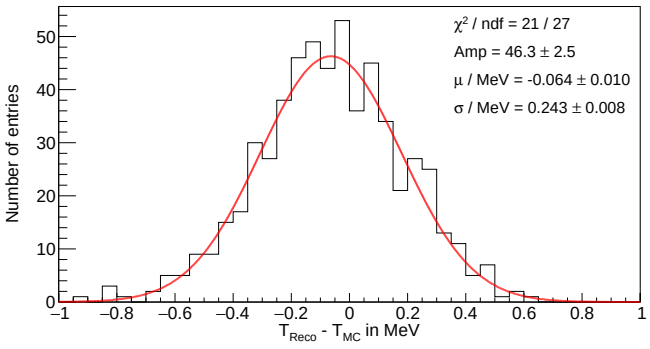

Figure 9.5: Reconstructed energy for pad plane PRM6 at 20 bar and 0.0160 $\mathrm{GeV}^2\,c^{-2}$. Only tracks, where the most outer ring was not included, were considered. This is done to avoid events, where the proton might escape the TPC. For such events this method would not be valid anymore.

[5] The factor $\sqrt{12}$ is explained in the appendix F.

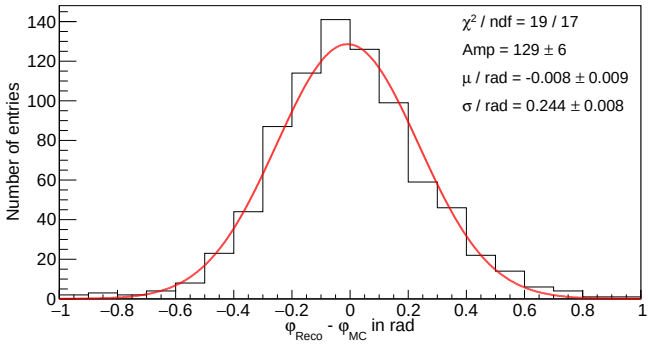

Figure 9.6: Reconstructed azimuthal angle for pad plane PRM6 at 20 bar and 0.0160 GeV^2 c^{-2}.

In figure 9.7 the difference between reconstructed proton energy and MC-truth value is shown for 20 bar. The left side shows the results from the standard pad planes[6] and the rotated ones.

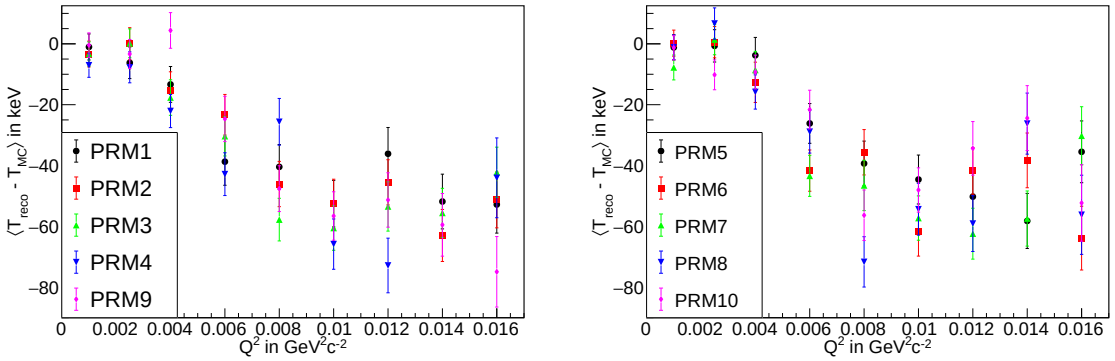

(a) Not rotated pad planes.

(b) Rotated pad planes.

Figure 9.7: Mean difference between the reconstructed energy and the MC-truth value for all implemented pad planes as shown in the appendix B at 20 bar.

All pad planes have the same behaviour according to the reconstructed energy. No geometry seems to have an advantage compared to the others. Striking is that one can see a negative slope in the reconstructed energy with increasing momentum transfer. It cannot be explained by leaving protons, as only events are taken into account in which it is recognized that the proton has not left the TPC. This is evaluated by checking if the most outer ring is hit. If this is the case one cannot be sure anymore if the proton stayed inside the TPC or left it. A possible explanation is that the signals from outer pads are too small to be integrated or too tight time cuts leading to missing reconstructed energy.

In figure 9.8 the fraction of events is shown in which the proton has not left the TPC at 20 bar. As described this is done by looking if the most outer ring measured a proton signal.

[6] The standard pad planes are the ones having no rotations.

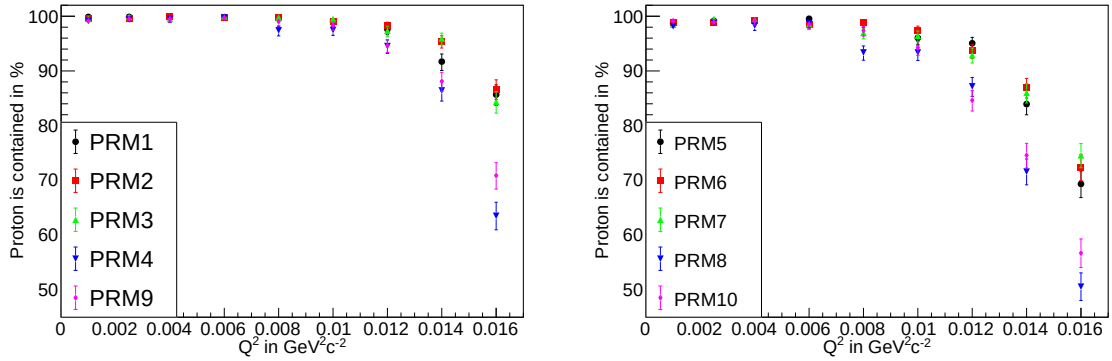

(a) Not rotated pad planes.

(b) Rotated pad planes.

Figure 9.8: Fraction of events in which it is recognized that the proton has not left the TPC (no signal on the most outer ring) for all implemented pad planes as shown in the appendix B at 20 bar.

Here one can see a clear distinction between the pad planes having no change in the radial size of the rings and the ones for which the radii are varied. When having a bigger outer ring one already starts to reject events with smaller ranges and therefore smaller momentum transfers. That explains the drop for smaller values of Q^2 for these pad plane geometries.

The standard deviations of the distributions of the energy difference are shown in figure 9.9.

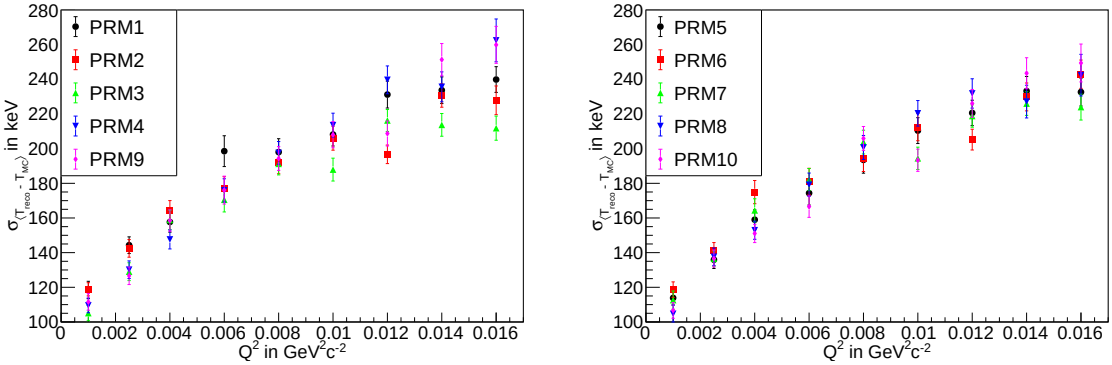

(a) Not rotated pad planes.

(b) Rotated pad planes.

Figure 9.9: Standard deviation of the distributions of the difference between the reconstructed energy and the MC-truth value for all implemented pad planes as shown in the appendix B at 20 bar.

One cannot observe any advantage of a tested pad plane geometry either. The plotted standard deviations can be identified with the energy and therefore Q^2-resolution of the TPC. Taking just the limits of the graphs in figure 9.9 one can determine a resolution of the momentum transfer between 1.9×10^{-4} to 5.3×10^{-4} GeV^2 c^{-2} when using

$$Q^2 = 2m_\mathrm{p}T_\mathrm{p} \qquad \text{and therefore} \qquad \Delta Q^2 = 2m_\mathrm{p}\Delta T_\mathrm{p}\,.$$

This resolution is as figure 9.9 implies depending on the momentum transfer itself. This dependence originates in the fact that with increasing Q^2 the number of pads that are crossed by the proton is increasing. With a higher number of pads one picks up more noise generated on the one hand by the electronics and on the other hand by the beam itself. Assuming an energy resolution of 20 keV per channel from the read-out electronics this part can vary between

$$20\,\mathrm{keV} \qquad \text{and} \qquad \sqrt{9}\cdot 20\,\mathrm{keV} = 60\,\mathrm{keV}\,,$$

depending on the range of the proton (which is Q^2-dependent as figure 6.6 shows). This calculation is true under the assumption that the protons go radially out from the center of the TPC. As this assumption is not fulfilled in every case as there are protons that also may hit two pads of a ring more electronics noise is added. Beside the pick-up of the electronic noise with more pads the beam noise in each pad adds up as well leading to another momentum transfer dependent source of noise.
This estimated Q^2-resolution is coming from the TPC alone. This should not be taken as the Q^2-resolution of the whole experiment. To extract the latter one needs to do a kinematic matching of the recoil proton and the beam muon detected by the silicon trackers. Then one can calculate the resolution of the silicon telescopes and combine it with the result of the TPC to finally extract the Q^2-resolution of the whole apparatus.
As described above one would expect that a finer angular segmentation leads to less beam noise. This behaviour cannot be observed here. This might come from the fact that the beam noise only contributes in the first two rings. As shown in the appendix B the difference between the central region of the read-out of the TPC and the outer regions is about two orders of magnitude. The second ring has the highest amount of beam noise as the area of these pads is larger. As the segmentation of the second ring has not been changed all pad planes have a similar energy resolution as the main noise component of the beam is originated by the second ring.
Segmenting the second ring further would lead to less statistics when reconstructing low energetic protons. To detect the protons at low-Q^2 for 20 bar too[7] one selects the pad corresponding to the scattering vertex with the help of the silicon trackers. At these low energies it is necessary that the proton is stopped really within a range corresponding to this pad otherwise the signal would be lost in the noise because of charge sharing with neighbouring pads. Therefore, one applies a cut that the vertex is at least 2 mm away from the borders of the pad. Reducing the size of the anodes of the second ring would lead to insufficient statistics. The problem is shown in figure 9.10.

The second parameter for the pad plane optimization is the evaluation of the azimuthal angle of the proton. First the fraction of events for which a proton track has been fitted is calculated. The results are depicted in figure 9.11.
One can observe a clear advantage of the pad planes having smaller radii for the central anode rings. By reducing the radial size of the center of the read-out, tracks with smaller Q^2 cross at least three rings earlier compared to no reduction. Therefore, the fraction shown in figure 9.11 starts to increase for smaller values of the momentum transfer for the options with reduced radii in the center.
Up to now there has been no significant difference between the standard and the rotated pad planes. The

[7] These protons have only a short range corresponding to a single pad of about 1 to 2 mm.

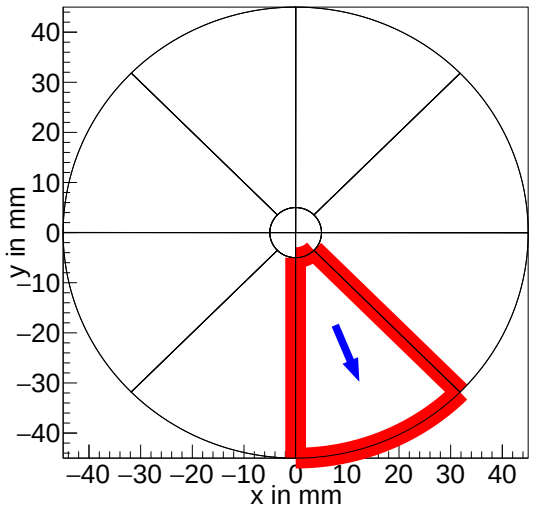

Figure 9.10: Here, it is shown, why the second ring has not been segmented into more pads. The red lines correspond to the stated 2 mm. The proton track (in blue) needs to be at least 2 mm away from the borders of the pad guaranteeing that the proton is stopped within the range corresponding to the pad. Otherwise one would have charge sharing with neighbouring pads leading to too small events.

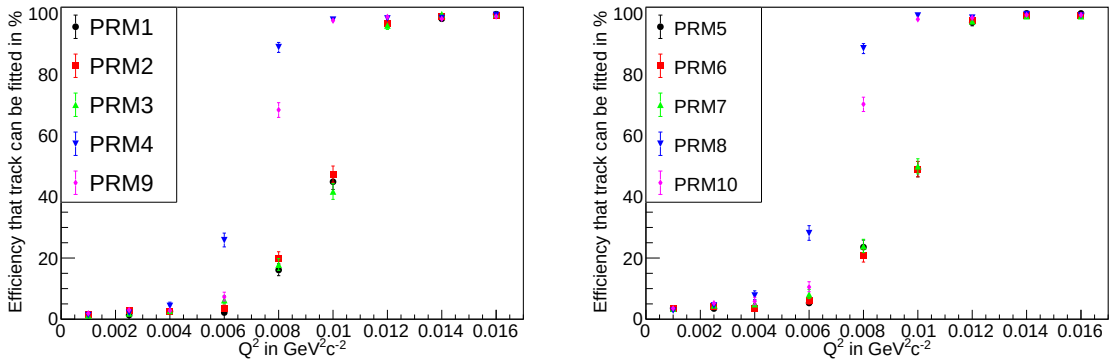

(a) Not rotated pad planes

(b) Rotated pad planes

Figure 9.11: Fraction of events where at least three pads are included in the track and the track has been fitted for all implemented pad planes as shown in the appendix B at 20 bar.

advantage of misaligning the rings by rotating them comes into play when looking at the reconstructed azimuthal angle of the proton tracks. The mean difference between the reconstructed direction of the proton and the MC-value is depicted in figure 9.12.
The Q^2-range shown in figure 9.12 is chosen so that the proton range is high enough and hence, the tracks can be fitted. With lower Q^2-values in the graph the small differences here would not be visible as the tracking fails. The mean difference is in nearly all cases compatible with zero for the rotated pad planes as the angular resolution is better compared to the not rotated ones which is shown in

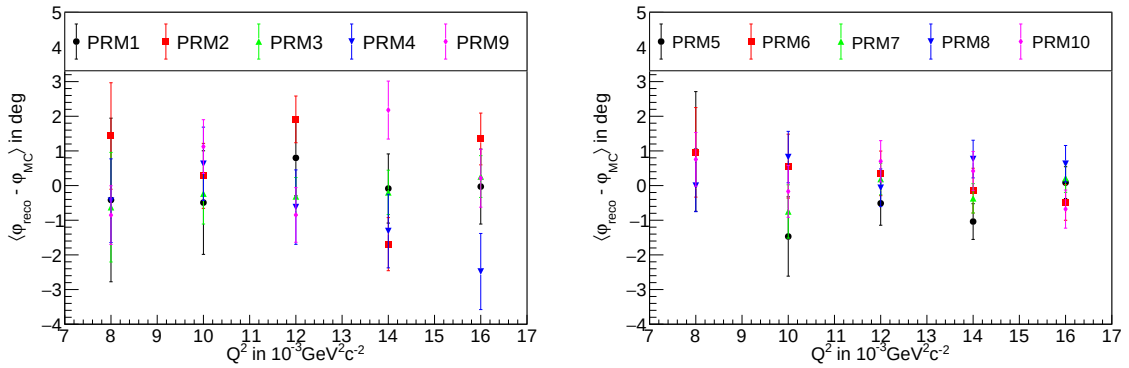

(a) Not rotated pad planes.

(b) Rotated pad planes.

Figure 9.12: Mean difference between the reconstructed azimuthal angle of the proton and the MC-truth value for all implemented pad planes as shown in the appendix B at 20 bar.

figure 9.13.

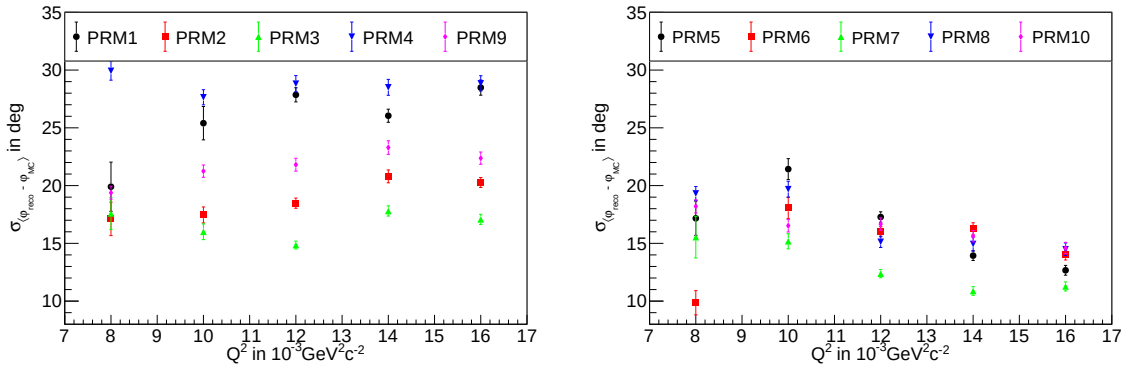

(a) Not rotated pad planes.

(b) Rotated pad planes.

Figure 9.13: Standard deviation of the distributions of the difference between the reconstructed azimuthal angle of the proton and the MC-truth value for all implemented pad planes as shown in the appendix B at 20 bar.

In figure 9.13 one can see the biggest difference between the rotated pad planes and the standard geometries. While the aligned anode planes have an angular resolution of about 20° to 25° nicely fitting the stated $\frac{90°}{\sqrt{12}}$ [8] the misaligned ones have a resolution in the order of 15°. One would definitely profit from having a finer φ-segmentation as the resolution implies especially for shorter tracks. This geometric effect cancels out partially at least for larger momentum transfers coming from averaging over more rings as long as the other rings are still segmented into four pads.

The results for simulations at 4 bar are shown in the appendix C. These plots show the same behaviour as for 20 bar. The only difference is that the energy resolution is better. This can be explained by the

[8] The resolution is a bit better coming from the finer segmentation of the second ring.

lower hydrogen density leading to less energy loss of the pile-up muons in the TPC. Therefore, the beam noise is less leading to a better energy resolution.

Following these discussions one can judge about the different pad planes.
In terms of energy reconstruction and resolution no pad plane has any advantage compared to the others. There is also no difference between the rotated and not rotated case for the tested geometries. An observed disadvantage of the pad planes with reduced radii of the central rings is that a higher fraction of events is excluded as one cannot be sure whether the measured protons are contained within the TPC or not. As in the cases of PRM4 and PRM8 the most outer ring has been enlarged, the drop is already significant for smaller values of Q^2 of around $0.012\,\mathrm{GeV}^2\,c^{-2}$. Looking at PRM9 and PRM10 there is also a drop compared to the other planes even though the most outer ring has the same size. This can be explained by the fact that if a pad of the second outer ring is added to the proton track its neighbours are analyzed. If there is a (wrongly as proton identified) signal on the ninth ring even though the proton is stopped at the eighth it is recognized as a leaving one. This can happen at smaller momentum transfers as the inner radius of the eighth ring is at smaller values.
The similarity to the Mainz-experiment presented in the introduction 1 makes a comparison between both approaches possible as well as the usage of the energy-range calibration of the TPC[9]. But to follow the same calibration the radial segmentation of the read-out anodes need to be the same. Therefore, the reduction of the radial size in the center to extract proton tracks already at small Q^2-values as shown in figure 9.11 would need a strong advantage in terms of energy resolution which is not the case. Therefore, this option will be excluded.

It is definitely favourable to use one of the rotated pad planes in the experiment because of the better φ-resolution coming from the misaligned rings. The better resolution can be very helpful when connecting the measured proton events from the TPC with muons detected in the silicon telescopes. As the beam rate is planned to be 2 MHz and the drift time for electrons from the cathode to the grid is about 100 µs there will be on average 200 muons measured by the silicon trackers for one proton event in the TPC. By comparing the scattering events in the xy-plane what is indicated by the azimuthal angle φ one can reject false events measured by the silicon detectors. Beside the rotation a finer angular segmentation is also helpful in terms of φ-resolution. But already going from PRM6 (44 pads) to PRM7 (48 pads) needs four read-out channels per anode plane in addition. The gain in resolution is in the order of 5°. To judge if this better resolution is necessary a dedicated study on the matching between the proton and muon tracks needs to be performed. It only makes sense to equip the read-out with more channels if the matching works much better with the better angular resolution of the TPC.

9.3 Beam noise

In the previous section 9.2 the energy resolution and from that the Q^2 have been determined. A crucial contribution to the overall energy resolution is the described beam noise originating from the pile-up in the TPC. The evaluation of its magnitude is done in the following.
The beam noise is defined and can be determined as described in the following way:
One generates a short electronic signal (the duration of it should be much less than the shaping time of the electronics from section 8.2 which is 1.4 µs) with an integral of 1.5 MeV [34, 45]. Here, a

[9] The energy-range-calibration is explained in [48].

rectangular test pulse with a duration of 100 ns and an amplitude of 15 MeV μs^{-1} has been generated as shown in figure 9.14[10].

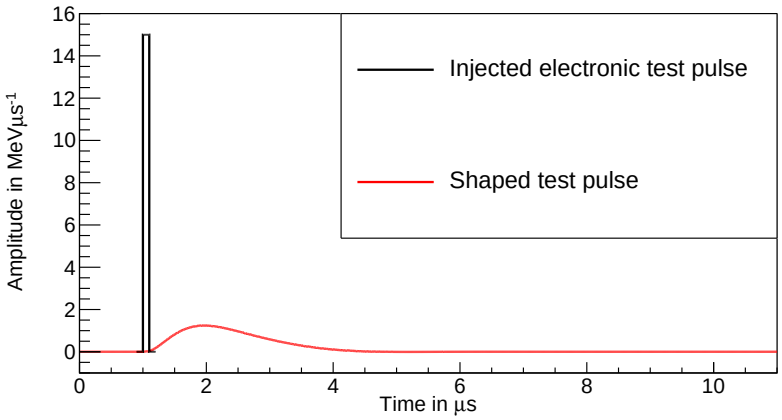

Figure 9.14: Here, the injected electronic pulse to determine the beam noise is shown in black. The red signal corresponds to the shaped test pulse. One can see that the duration of the shaped signal is overwhelmingly determined by the shaping time of the read-out electronics one not by the test pulse itself.

The test pulse shown in figure 9.14 is added on top of the electronic noise and background from the beam as described in section 8.3. It is induced in every pad so that the noise contribution from the beam can be determined for every ring. The only difference is that no protons are generated so that only noise events are considered. The start time of the pulse is uniformly distributed along the signal between 10 and 90 µs so that it is guaranteed that the pulse is contained in the full signal and that it is during the constant part of the beam noise (cf. discussion about the length of the signal in section 8.1). The signal integration is done in the same way as described in section 9.1.2, but here obviously no proton track exists that needs to be fitted. The simulation is done in TGeant in the same way as shown in section 8.1 for every pad plane that is implemented at 4 and 20 bar[11]. Now, only 500 events are simulated, but the results from every sensitive volume for every pad can be used. Therefore, one has 2 000 events for every pad of all geometries. The width of the distribution one gets when integrating the test signal corresponding to the 1.5 MeV-proton gives the combined electronic and beam noise.

In figure 9.15 the reconstructed energy of the 1.5 MeV-test pulse is exemplary shown for pad 39 (most outer ring) of pad plane PRM1. The standard deviations of all these distributions, i.e. for every pad and pad plane, are now used to calculate the beam noise contribution. The mean values of the standard deviations of all pads of every ring will be determined. Here, one needs to be aware that the beam is neither symmetric in x- and y-direction nor centered. This leads to different magnitudes of the pads in a certain ring and hence leads to larger standard deviations for the first and second ring, as the whole beam is nearly focused onto these rings.
The results are depicted in the tables 9.2 to 9.6. Taking a resolution of the electronics of $\sigma_{\text{electronics}} = (23.68 \pm 0.08)$ keV (cf. section 8.2) that is present in every pad one can finally calculate the fraction

[10] The amplitude is calculated by dividing the integral of the signal, which is 1.5 MeV by its duration of 100 ns.

[11] The results are only calculated for the not rotated pad planes. There is no difference in noise when the rings are rotated with respect to each other

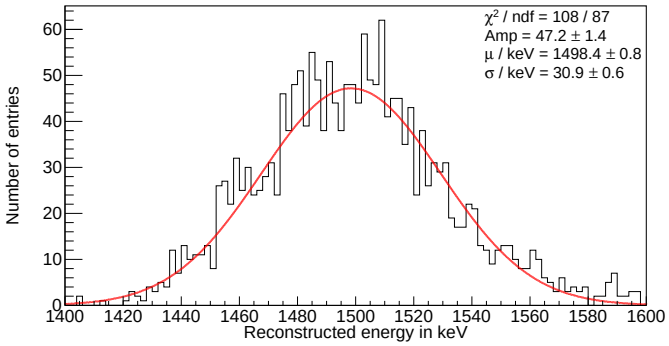

Figure 9.15: Reconstructed energy of an electronic signal corresponding to a 1.5 MeV-proton. The standard deviation is used to extract the contribution of the beam noise.

originated by the beam when assuming that both contributions are uncorrelated, i.e.

$$\sigma = \sqrt{\sigma^2_{\text{beam}} + \sigma^2_{\text{electronics}}}\,.$$

	4 bar		20 bar	
Ring	σ in keV	σ_{beam} in keV	σ in keV	σ_{beam} in keV
1	25.4 ± 0.4	9.1 ± 2.1	47.3 ± 1.0	40.9 ± 2.3
2	28.4 ± 1.1	16 ± 4	68 ± 5	63 ± 11
3	24.4 ± 0.5	6 ± 4	48.0 ± 1.0	41.8 ± 2.2
4	24.45 ± 0.28	6.1 ± 2.3	50.1 ± 0.7	44.2 ± 1.7
5	24.31 ± 0.12	5.5 ± 1.3	46.2 ± 0.4	39.7 ± 1.0
6	24.0 ± 0.4	4 ± 5	42.0 ± 0.7	34.7 ± 1.7
7	23.73 ± 0.26	2 ± 8	39.2 ± 0.4	31.2 ± 1.0
8	23.41 ± 0.34		36.5 ± 3.8	27.8 ± 1.0
9	23.67 ± 0.16		30.1 ± 0.4	18.5 ± 1.2

Table 9.2: Total noise and beam noise extracted for the pad plane PRM1 at 4 and 20 bar. If the extracted noise on a ring is smaller than the electronic noise, the beam noise is not given.

For a pressure of 4 bar the contribution of the beam noise is negligible. At this setting one is purely dominated by the resolution of the read-out electronics. The missing entries in the tables 9.2 to 9.6 are those where the total noise is smaller than the electronic noise itself. This is physically not reasonable, nevertheless it occurs sporadically. In those cases, the total noise is virtually the same as the electronic noise stating that the beam does not increase the resolution for the outer read-out channels.
At 20 bar this is not the case. Here, the noise is mostly determined by its beam contribution. In the tables 9.2 to 9.6 one can nicely see the difference of the beam noise when changing the segmentation or size of a ring. As described in section 9.2 in the second ring the most beam noise is induced what can be explained by its size and the beam profile. This can be verified with the analysed noise simulations. Taking into account the extracted resolutions for the reconstructed proton energies from section 9.2 these noise values cannot explain energy resolutions in the order of 200 keV depending on

	4 bar		20 bar	
Ring	σ in keV	σ_{beam} in keV	σ in keV	σ_{beam} in keV
1	25.34 ± 0.12	9.0 ± 0.8	47.0 ± 0.9	40.6 ± 2.0
2	28.6 ± 1.1	16 ± 4	68 ± 6	63 ± 12
3	23.59 ± 0.19		36.6 ± 0.7	27.9 ± 1.8
4	24.26 ± 0.17	5.3 ± 1.7	50.8 ± 0.5	44.9 ± 1.1
5	24.06 ± 0.25	4.2 ± 3.0	46.8 ± 1.3	40.3 ± 3.1
6	24.23 ± 0.18	5.1 ± 1.9	41.3 ± 1.0	33.8 ± 2.3
7	24.3 ± 0.4	5.3 ± 3.3	40.0 ± 0.5	32.3 ± 1.2
8	23.68 ± 0.34		36.3 ± 0.8	27.5 ± 2.1
9	23.58 ± 0.11		29.7 ± 0.5	17.9 ± 1.6

Table 9.3: Total noise and beam noise extracted for the pad plane PRM2 at 4 and 20 bar. If the extracted noise on a ring is smaller than the electronic noise, the beam noise is not given.

	4 bar		20 bar	
Ring	σ in keV	σ_{beam} in keV	σ in keV	σ_{beam} in keV
1	25.51 ± 0.19	9.5 ± 1.1	45.74 ± 0.24	39.1 ± 0.6
2	28.4 ± 1.1	16 ± 4	68 ± 5	64 ± 12
3	23.61 ± 0.27		36.38 ± 0.21	27.6 ± 0.6
4	23.78 ± 0.17	2 ± 4	37.4 ± 0.4	29.0 ± 1.1
5	24.10 ± 0.30	4 ± 3	46.7 ± 1.1	40.2 ± 2.5
6	23.70 ± 0.31	1 ± 16	41.4 ± 0.4	34.0 ± 1.0
7	23.57 ± 0.10		39.8 ± 0.7	32.0 ± 1.8
8	24.49 ± 0.22	6.3 ± 1.8	37.75 ± 0.19	29.4 ± 0.5
9	23.6 ± 0.5		31.2 ± 0.7	20.3 ± 2.2

Table 9.4: Total noise and beam noise extracted for the pad plane PRM3 at 4 and 20 bar. If the extracted noise on a ring is smaller than the electronic noise, the beam noise is not given.

Q^2 and therefore depending on the range alone. Summing up the noise at 20 bar for pad plane PRM1 in quadrature one gets approximately 140 keV. This means that the reconstruction algorithm induces a resolution in the same order as the beam and the electronics. This might be explained as before in section 9.2 by signals being in the same order of magnitude as the noise so that they are too small to be integrated.
In the proposal it is stated that the beam induces a resolution of approximately 35 keV per pad for the geometry PRM1. This number can only be verified partially. At the outer rings, i.e. from ring six on, the beam noise is in the order of 30 keV going down to 20 keV for the most outer ring. For the inner rings, all except for the second, 40 keV have been extracted. These results are in good agreement with the stated value from the proposal. The largest difference occurs for the second ring with a beam noise of about 60 keV. These differences might be explained by the fact that one has dealt with a circular beam profile with a diameter of 1 cm corresponding to the diameter of the first ring. From these results the noise of the other rings has been estimated. Here, the realistic beam profile of the

	4 bar		20 bar	
Ring	σ in keV	σ_{beam} in keV	σ in keV	σ_{beam} in keV
1	26.11 ± 0.32	11.0 ± 1.5	48.1 ± 0.6	41.8 ± 1.3
2	28.1 ± 0.9	15.1 ± 3.2	63 ± 6	59 ± 12
3	23.98 ± 0.16	3.8 ± 2.3	37.9 ± 1.3	29.6 ± 3.3
4	23.87 ± 0.21	3 ± 4	37.7 ± 0.9	25.4 ± 2.6
5	24.60 ± 0.15	6.7 ± 1.3	51.2 ± 1.0	45.4 ± 2.2
6	23.95 ± 0.17	3.6 ± 2.5	50.8 ± 0.6	45.0 ± 1.3
7	24.09 ± 0.25	4.4 ± 2.9	44.1 ± 0.6	37.16 ± 0.13
8	24.40 ± 0.30	5.9 ± 2.6	52.6 ± 0.7	46.9 ± 1.5
9	24.3 ± 0.5	5 ± 4	40.2 ± 1.2	32.5 ± 2.9

Table 9.5: Total noise and beam noise extracted for the pad plane PRM4 at 4 and 20 bar.

	4 bar		20 bar	
Ring	σ in keV	σ_{beam} in keV	σ in keV	σ_{beam} in keV
1	25.54 ± 0.34	9.6 ± 1.8	46.9 ± 0.5	40.5 ± 1.2
2	28.1 ± 1.0	15 ± 4	68 ± 6	63 ± 12
3	24.5 ± 0.5	6 ± 4	49.7 ± 1.6	44 ± 4
4	23.71 ± 0.31	1 ± 13	50.5 ± 0.5	44.6 ± 1.1
5	24.2 ± 0.7	5 ± 6	46.5 ± 1.3	40.0 ± 3.0
6	24.49 ± 0.26	6.2 ± 2.1	42.3 ± 0.8	35.1 ± 2.0
7	23.3 ± 0.4		39.6 ± 0.4	31.7 ± 1.0
8	23.48 ± 0.31		35.7 ± 0.5	26.8 ± 1.4
9	23.78 ± 0.33	2 ± 9	30.54 ± 0.20	19.3 ± 0.7

Table 9.6: Total noise and beam noise extracted for the pad plane PRM9 at 4 and 20 bar. If the extracted noise on a ring is smaller than the electronic noise, the beam noise is not given.

muon beam in the M2 beam line has been used.

CHAPTER 10

Summary and outlook

During this thesis several aspects of the simulation of the active-target TPC for the COMPASS++/AMBER proton charge-radius experiment have been studied.
First of all, the energy loss simulated in the TGeant-framework has been analyzed and compared to the PAI-model. With high-energy corrections, for example bremsstrahlung, the energy deposition of the muons in the TPC is accurately described in the simulations. One can extract a mean energy loss of about 290 keV in a single sensitive volume, i.e. 40 cm of hydrogen gas at 20 bar. This energy deposition will be distributed according to the muon beam profile in the M2 beam line and will lead to a large background in the TPC. This background needs to be taken into account when dealing with energy resolutions of the pad read-out of the TPC. The protons, analyzed during this thesis, are anyhow stopped in the sensitive volume of the TPC most of the time. So, their energy-loss distributions are of minor interest. It is relevant, of course, as soon as the protons leave the TPC. In the case of a leaving proton, the specific energy loss will be used to determine the kinetic energy of the escaping proton.

The analysis of the pad response functions shows the influence of the overall pad geometry. Here, different outlines have been studied while keeping the overall circular form of the pad plane. The induced signals of all pads, except for the ones from first ring, could be qualitatively described by a second order polynomial together with a step-function that accounts for the drift time of the electrons. The pad response functions of the first ring are more complicated leading to an empirical fit of a sixth order polynomial. At this point one can say that the majority of the electric signal induced in the first ring is originated within the last 200 ns even though the overall drift time from *Frisch*-grid to the anode plane takes about 1.18 µs. This can be explained by the geometry of the pad leading to such a form of the weighting field.
The rotation of rings with respect to each other has been tested, as well as a finer angular segmentation of those and the influence of their radial size. For pads of such a size, i.e. several cm^2 it has not been expected that a rotation influences the induced signals of the read-out electrodes. This assumption has been validated. Such a behaviour can be explained by the rotational symmetry of the ring and the fact that most of the field lines connect the pad that is read out with the cathode. In this case the cathode corresponds to the *Frisch*-grid of the TPC. The division into more angular segments changes the pad response function only slightly. This can be explained in the same way as before. The behaviour, i.e. the weighting field, might change if the sizes of the pads get in the order of magnitude of the gap between those.

The reduction of the radial size of the inner rings showed a change of the induced signals. When comparing the pad response functions of the second ring for the initially proposed geometry with the results for smaller radii of the second and third ring, one can explain this change by the change of the radial position of the pads.
As there will be systematic studies during the COMPASS++/AMBER proton charge-radius experiment with a lower pressure of 4 bar as well, the influence of the different electric field and pressure on the induced signals has been studied. As the weighting fields are not influenced by a change of the real electric field and the drift velocity is the same because of the reduced electric field, the pad response functions do not change when lowering the pressure. The only difference one can see, is the larger longitudinal diffusion that leads to a larger smearing of the step at the end of the electron drift, as well as the overall variation at 4 bar compared to 20 bar of the pad response functions. These larger variations can be explained by the overall larger diffusion in 4 bar originated by a smaller interaction probability leading to a hotter gas compared to 20 bar.

For the pad plane studies several new objects have been implemented in the TGeant-framework. The first step after the energy deposition simulated by Geant4 is the electron drift. The values used there are based on results using Magboltz inside Garfield++. The electrons drift down towards the *Frisch*-grid and once they arrive there, they start to induce a signal in the electrodes of the pad plane. Therefore, the overall anode and pad geometry have been implemented in TGeant as well as the pad response functions for the different outlines. These are used to calculate the overall signal for a whole event that consists out of the beam muon that scatters elastically with a proton in the gas, the recoil proton and a large background generated by all other beam muons. With data from a test run performed in 2018 electronic noise has been taken into account as well.
The performance of different pad plane geometries in terms of energy and angular resolution has been analyzed. In terms of energy and therefore Q^2-resolution no pad plane seems to have an advantage compared to the others. This originates from the fact that most of the beam noise is induced in the second ring. As its angular segmentation has not been changed the overall noise is not reduced. The reduction of its radial size does not affect the resolution coming from the beam noise as one needs to sum up the energies measured by different rings to extract the total energy of the proton. By reducing the radial size of the second ring the third ring is now more influenced by the beam than before. Therefore, the beam noise does not change.
The Q^2-resolution of the TPC itself is between 1.9×10^{-4} and $5.3 \times 10^{-4}\,\mathrm{GeV}^2\,c^{-2}$ and depends on the proton range itself. Here, one has to be aware that this is really the resolution of the TPC without having a kinematic matching between the proton and beam muon. The matching will definitively improve these results, especially when combining the TPC and the silicon data.
The resolution when measuring the azimuthal angle can be drastically improved when rotating the anode rings with respect to each other without equipping the read-out with more electronic channels. For the not rotated pad planes the best angular resolution, that has been reached, is about 20°. Here, four angular segments more have been used on the third and fourth ring respectively. With a rotation such a result was already reached with having the same number of read-out channels as for the initially proposed geometry. For momentum transfers larger than $0.014\,\mathrm{GeV}^2\,c^{-2}$ an angular resolution of 10° has been achieved.
The positive influence of a reduction of the radial size of the rings in the center on the proton track fitting has been examined. But this option is excluded as the energy-to-range calibration of the TPC will be adopted from the Mainz-experiment. This option has been excluded as the energy resolution is

not better compared to the other options.

A study of the beam noise in the TPC has been performed as well for the different pad planes. Here, one can see the effect of the different geometries on the beam noise itself. For a pressure of 20 bar one can extract a contribution coming from the muon beam in the order of 20 to 40 keV which is in agreement with the stated value of 35 keV in the proposal which has been an estimation. For the second ring there is a discrepancy as here one gets a beam noise of about 60 keV explained by the pad size itself and the muon beam profile which has not been taken into account in the estimations in the proposal.

In further studies one needs to analyze the generated Monte-Carlo data of the silicon telescopes and the TPC in combination. Here, one needs to do a kinematic matching of the proton track predicted by the TPC leading to a prediction for the beam muon, and the reconstructed muon track coming from the silicon trackers. Based on this, one can do a dedicated analysis which pad plane geometry can reject most of the muon candidates while having a comparable Q^2-resolution. A very powerful criterion for the rejection of pile-up muons is the reconstruction of the azimuthal angle of the proton track in the TPC.
The scattering in the direction of the beam, i.e. the z-axis, can be determined with the TPC as well and needs to be investigated. The angle with respect to the beam axis can be measured in the following way: If the proton receives a finite momentum in the z-direction, it does not fly perpendicular to the TPC axis and normal vector of the read-out plane. Because of this finite component, the electron-ion pairs, that are created through the energy-loss of the proton in the gas, have different z-coordinates. Therefore the electrons need to drift different distances to the *Frisch*-grid and anode. Having a constant drift velocity of the electrons in the TPC these different distances can be converted into different arrival times of the signal in the read-out electrodes that are crossed by the proton. Together with the overall track length of the proton one is able to calculate then the scattering angle with respect to the beam axis. With this scattering angle the transferred momentum in the z-direction can be determined.
With the implemented pad planes one can now do a dedicated study on the energy reconstruction of the protons with the help of the specific energy loss $\frac{\mathrm{d}E}{\mathrm{d}x}$. For squared momentum transfers larger than approximately $0.02\,\mathrm{GeV}^2\,c^{-2}$ the protons can leave the TPC. Therefore, one cannot reconstruct the kinetic energies of the protons by summing up the energies measured by the read-out electrodes. But, by looking at the specific energy loss one is able to extract the momentum itself, as the energy-loss distributions look different for different proton momenta.
Another aspect, one should investigate, is the resolution of the reconstructed z-position of the scattering vertex. With the help of an external trigger and external time information generated by the scintillating fibers described in chapter 4, one is able to determine the z-position of the scattering vertex. As the beam muons traverse the fibers and the whole TPC virtually at the same time one can calculate the z-coordinate of the vertex from the time difference between the signals generated in the fibers and the TPC. Together with the drift velocity of the electrons liberated by the recoil proton in the TPC this time difference can be converted into the z-position of the scattering vertex.
The reconstruction algorithm might be examined as well. As it has been shown the energy resolution is not only determined by the read-out electronics and the beam noise, but there is another contribution

of the same order of magnitude, i.e. about 140 keV. This contribution might be explained by the reconstruction. Here, especially the integration time influences the total noise. The beam noise can be reduced by shortening the integration time window.

In 2021 there will be a dedicated pilot run with a smaller TPC. It is a modified version of the so-called IKAR-TPC [37]. It consists of two sensitive volumes and a read-out plane with a radius of 200 mm. With this thesis the geometry of the anodes has been selected, which is shown in figure 10.1. It is similar to the pad plane PRM6 B.2 with rings being 1 mm smaller compared to the implemented and simulated ones.

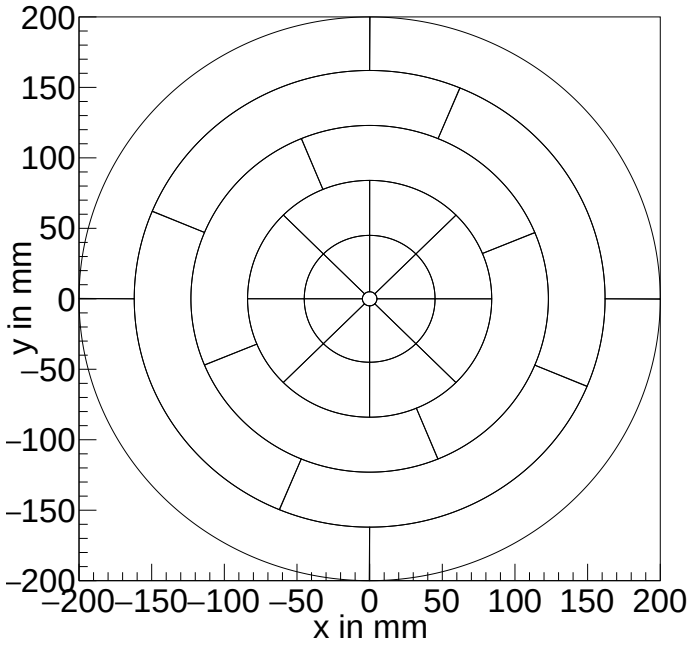

Figure 10.1: Geometry of the read-out for the tes run in 2021. The IKAR-TPC will be equipped with anodes looking like this one.

With this pad plane one can reconstructed protons up to squared momentum transfers of about 0.01 to $0.015\,\mathrm{GeV}^2\,c^{-2}$ with the reconstruction method presented in this thesis. For higher energies one can study the performance of the energy determination via the $\frac{\mathrm{d}E}{\mathrm{d}x}$-method. One may also investigate the different noise contributions, i.e. the resolution of the electronics and the influence of the muon beam in the M2 beam line as virtually the entire beam is contained within this area. If the silicon telescopes and scintillating fibers are in an operational state until the start of the test run, the kinematic matching of the proton and beam muon can be checked as this is as well a crucial aspect of the behaviour of the TPC read-out geometry.

Bibliography

[1] E. Rutherford,
LIV. Collision of α particles with light atoms. IV. An anomalous effect in nitrogen, The London, Edinburgh, and Dublin Philosophical Magazine and Journal of Science **37** (1919) 581, URL: https://doi.org/10.1080/14786440608635919 (cit. on p. 1).

[2] R. Frisch and O. Stern, *Über die magnetische Ablenkung von Wasserstoffmolekülen und das magnetische Moment des Protons. I*, Zeitschrift für Physik **85** (1933) 4, URL: https://doi.org/10.1007/BF01330773 (cit. on p. 1).

[3] R. Hofstadter and R. McAllister, *Electron Scattering From the Proton*, Phys. Rev. **98** (1955) 217 (cit. on p. 1).

[4] P. J. Mohr, B. N. Taylor and D. B. Newell,
CODATA recommended values of the fundamental physical constants: 2014,
Rev. Mod. Phys. **88** (3 2016) 035009,
URL: https://link.aps.org/doi/10.1103/RevModPhys.88.035009 (cit. on p. 2).

[5] A. Antognini et al.,
Proton Structure from the Measurement of 2S-2P Transition Frequencies of Muonic Hydrogen,
Science **339** (2013) 417, ISSN: 0036-8075,
URL: https://science.sciencemag.org/content/339/6118/417 (cit. on p. 2).

[6] R. Pohl et al., *The size of the proton*, Nature **466** (2010) 213,
URL: https://www.nature.com/articles/nature09250 (cit. on p. 2).

[7] I. T. Lorenz et al.,
Theoretical constraints and systematic effects in the determination of the proton form factors,
Phys. Rev. D **91** (1 2015) 014023,
URL: https://link.aps.org/doi/10.1103/PhysRevD.91.014023 (cit. on p. 2).

[8] H.-W. Hammer and U.-G. Meißner, *The proton radius: From a puzzle to precision*,
Sci. Bull. **65** (2020) 257, arXiv: 1912.03881 [hep-ph] (cit. on p. 2).

[9] W. Xiong et al., *A small proton charge radius from an electron–proton scattering experiment*,
Nature **575** (2019) 147 (cit. on p. 2).

[10] C. Peng and H. Gao, *Proton Charge Radius (PRad) Experiment at Jefferson Lab*,
EPJ Web of Conferences **11** (2016) 03007,
URL: https://doi.org/10.1051/epjconf/201611303007 (cit. on p. 3).

[11] B. Adams et al., *COMPASS++/AMBER: Proposal for Measurements at the M2 beam line of the CERN SPS Phase-1: 2022-2024*, (2019), URL: http://cds.cern.ch/record/2676885
(cit. on pp. 3, 6, 17, 18, 21, 34, 52, 54).

[12] A. Vorobyev and A. Denig, *Proposal to perform an experiment at the A2 hall, MAMI:"High Precision Measurement of the ep elastic cross section at small Q^2"*, (2017) (cit. on pp. 3, 20).

[13] R. Gilman et al., *Technical Design Report for the Paul Scherrer Institute Experiment R-12-01.1: Studying the Proton "Radius" Puzzle with μp Elastic Scattering*, (2017), arXiv: 1709.09753 [physics.ins-det] (cit. on p. 3).

[14] M. N. Rosenbluth, *High Energy Elastic Scattering of Electrons on Protons*, Phys. Rev. **79** (4 1950) 615, URL: https://link.aps.org/doi/10.1103/PhysRev.79.615 (cit. on p. 5).

[15] B. Povh et al., *Particles and nuclei: An Introduction to the physical concepts*, 7th ed., Springer, 2015, ISBN: 978-3-662-46320-8, URL: https://doi.org/10.1007/978-3-662-46321-5 (cit. on p. 5).

[16] J. C. Bernauer et al., *High-Precision Determination of the Electric and Magnetic Form Factors of the Proton*, Phys. Rev. Lett. **105** (24 2010) 242001, arXiv: 1007.5076, URL: https://link.aps.org/doi/10.1103/PhysRevLett.105.242001 (cit. on p. 5).

[17] S. Agostinelli et al., *Geant4—a simulation toolkit*, Nuclear Instruments and Methods in Physics Research Section A: Accelerators, Spectrometers, Detectors and Associated Equipment **506** (2003) 250, ISSN: 0168-9002, URL: http://www.sciencedirect.com/science/article/pii/S0168900203013688 (cit. on p. 7).

[18] W. W. M. Allison and J. H. Cobb, *Relativistic Charged Particle Identification by Energy Loss*, Annual Review of Nuclear and Particle Science **30** (1980) 253, URL: https://doi.org/10.1146/annurev.ns.30.120180.001345 (cit. on pp. 7, 10).

[19] *Garfield++*, URL: http://garfieldpp.web.cern.ch/garfieldpp/ (visited on 12/04/2020) (cit. on p. 7).

[20] I. B. Smirnov, *Modeling of ionization produced by fast charged particles in gases*, Nuclear Instruments and Methods in Physics Research Section A: Accelerators, Spectrometers, Detectors and Associated Equipment **554** (2005) 474, ISSN: 0168-9002, URL: http://www.sciencedirect.com/science/article/pii/S0168900205016724 (cit. on p. 7).

[21] H. Kolanoski and N. Wermes, *Teilchendetektoren, Grundlagen und Anwendungen*, 1st ed., Springer, 2016, ISBN: 978-3-662-45349-0, URL: https://doi.org/10.1007/978-3-662-45350-6 (cit. on pp. 8, 12, 14).

[22] M. Tanabashi et al., *Review of Particle Physics*, Phys. Rev. D **98** (2018) 030001, URL: https://link.aps.org/doi/10.1103/PhysRevD.98.030001 (cit. on pp. 8, 10).

[23] *PSTAR: Stopping Power and Range Tables for Protons HYDROGEN*, URL: https://physics.nist.gov/PhysRefData/Star/Text/PSTAR.html (visited on 14/09/2020) (cit. on pp. 9, 27, 30).

[24] *Composition of HYDROGEN*, URL: https://physics.nist.gov/cgi-bin/Star/compos.pl?ap001 (visited on 07/06/2020) (cit. on pp. 9, 25, 30).

[25] H. Bichsel, *A method to improve tracking and particle identification in TPCs and silicon detectors*, Nuclear Instruments and Methods in Physics Research Section A: Accelerators, Spectrometers, Detectors and Associated Equipment **562** (2006) 154, ISSN: 0168-9002, URL: http://www.sciencedirect.com/science/article/pii/S0168900206005353 (cit. on pp. 11, 25, 28).

[26] W. Blum, L. Rolandi and W. Riegler, *Particle detection with drift chambers*, 2nd ed., Particle Acceleration and Detection, 2008, ISBN: 978-3-540-76683-4, URL: https://doi.org/10.1007/978-3-540-76684-1 (cit. on pp. 10, 12).

[27] W. Shockley, *Currents to Conductors Induced by a Moving Point Charge*, Journal of Applied Physics **9** (1938) 635, URL: https://doi.org/10.1063/1.1710367 (cit. on p. 14).

[28] S. Ramo, *Currents Induced by Electron Motion*, Proceedings of the IRE **27** (1939) 584, URL: https://doi.org/10.1109/JRPROC.1939.228757 (cit. on p. 14).

[29] C. Dreisbach, *COMPASS++/AMBER - Proton-Charge Radius Measurement*, Seminar talk at the COMPASS Collaboration Meeting, 10/09/2020 (cit. on p. 17).

[30] K. J. Flöthner, *Investigations of the Triple-GEM-Tracking Detector for COMPASS++/AMBER*, M. Sc. thesis (in progress): Rheinische Friedrich-Wilhelms-Universität Bonn, 2020 (cit. on p. 18).

[31] D. R. Nygren et al., *The Time Projection Chamber*, Phys. Today **31** (1978) 46, URL: https://doi.org/10.1063/1.2994775 (cit. on p. 19).

[32] F. Sauli, *Gaseous Radiation Detectors Fundamentals and Applications*, 1st ed., vol. 36, Cambridge Monographs on Particle Physics, Nuclear Physics and Cosmology, Cambridge University Press, 2014, ISBN: 978-1-107-04301-5, URL: https://doi.org/10.1017/CBO9781107337701 (cit. on p. 20).

[33] B. Ketzer, *Advanced Gaseous Detectors - Theory and Practice*, Lecture script, Summer term 2019 (cit. on p. 21).

[34] A. Inglessi, private communication (cit. on pp. 21, 33, 53, 68).

[35] S. Biagi, *Magboltz-transport of electrons gas mixtures*, CERN program library, 2011, URL: https://magboltz.web.cern.ch/magboltz/ (visited on 23/04/2020) (cit. on p. 22).

[36] J. L. Pack and A. V. Phelps, *Drift Velocities of Slow Electrons in Helium, Neon, Argon, Hydrogen, and Nitrogen*, Phys. Rev. **121** (3 1961) 798, URL: https://link.aps.org/doi/10.1103/PhysRev.121.798 (cit. on p. 22).

[37] A. A. Vorobyov et al., *A method for studies of small-angle hadron-proton elastic scattering in the coulomb interference region*, Nuclear Instruments and Methods **119** (1974) 509, ISSN: 0029-554X, URL: http://www.sciencedirect.com/science/article/pii/0029554X74908015 (cit. on pp. 22, 76).

[38] H. Schindler, *Garfield++ User Guide*, URL: http://garfieldpp.web.cern.ch/garfieldpp/documentation/UserGuide.pdf (visited on 12/04/2020) (cit. on pp. 23, 35, 102).

[39] *Geant4—a simulation toolkit, Physics Reference Manual, Release 10.6*, (2019), URL: http://geant4-userdoc.web.cern.ch/geant4-userdoc/UsersGuides/PhysicsReferenceManual/BackupVersions/V10.6/fo/PhysicsReferenceManual.pdf (cit. on pp. 24, 26, 27, 29).

[40] D. E. Groom, N. V. Mokhov and S. I. Striganov, *Muon stopping power and range tables 10 MeV - 100 TeV*, Atomic Data and Nuclear Data Tables **78** (2001) 183, ISSN: 0092-640X, URL: http://www.sciencedirect.com/science/article/pii/S0092640X01908617 (cit. on pp. 25, 31).

[41] *ANSYS*, URL: https://www.ansys.com/ (visited on 21/01/2020) (cit. on p. 33).

[42] *Mechanical APDL Documentation – Command Reference*, URL: https://www.mm.bme.hu/~gyebro/files/ans_help_v182/ans_cmd/Hlp_C_CmdTOC.html (visited on 21/01/2020) (cit. on p. 33).

[43] L. Gatignon et al., *Report from the Conventional Beams Working Group to the Physics beyond Collider Study and to the European Strategy for Particle Physics*, tech. rep. CERN-PBC-REPORT-2018-002, CERN, 2018, URL: https://cds.cern.ch/record/2650989 (cit. on p. 47).

[44] F. Sauli, *Principles of Operation of Multiwire Proportional and Drift Chambers*, (1977), URL: https://dx.doi.org/10.5170/CERN-1977-009 (cit. on p. 48).

[45] A. Dzyuba, private communication (cit. on pp. 51, 53, 68).

[46] M. Hoffmann, *A feasibility test for measuring the proton charge radius in high-energy muon-proton elastic scattering*, M. Sc. thesis: Rheinische Friedrich-Wilhelms-Universität Bonn, 2019 (cit. on pp. 51, 52, 58, 61).

[47] P. Abbon et al., *The COMPASS experiment at CERN*, Nuclear Instruments and Methods in Physics Research Section A: Accelerators, Spectrometers, Detectors and Associated Equipment **577** (2007) 455, ISSN: 0168-9002, URL: http://www.sciencedirect.com/science/article/pii/S0168900207005001 (cit. on p. 57).

[48] A. A. Vorobyov and N. Sagidova, *Method for precision measurement of the Range – Energy relation for protons in pure hydrogen gas*, (2019), arXiv: 1912.06065 [physics.ins-det] (cit. on p. 68).

[49] R. Fruehwirth, H. Pernegger and M. Friedl, *Convoluted Landau and Gaussian Fitting example*, URL: https://root.cern.ch/root/html404/examples/langaus.C.html (visited on 23/01/2020) (cit. on p. 97).

Appendix

APPENDIX A

Own contributions

- Mounting and dismounting of a GEM-detector at the COMPASS-experiment
- Development of a framework to extract the response functions of the pad read-out of the TPC that is planned to be deployed in the COMPASS++/AMBER proton charge-radius measurement; it is based on ANSYS ®, GARFIELD++ and MAGBOLTZ
- Implementing different new classes int the TGEANT-framework:
  - Drift and diffusion of electrons
  - Signal induction in the TPC
  - Different pad plane geometries
  - Electronic noise
- Analysis of the data presented in this thesis:
  - Extraction of the pad response functions for the read-out of the TPC
  - Estimation of the electronic noise in the TPC based on data taken during a test run in 2018
  - Determination of the energy and angular resolution for different pad plane geometries
  - Estimation of the beam noise that contributes to the total noise in the TPC

APPENDIX B

Implemented pad planes

Here, all pad planes are shown that can be used in TGEANT. The numeration is from the inside to the outside, going from 0° to 360° in the mathematical positive direction.

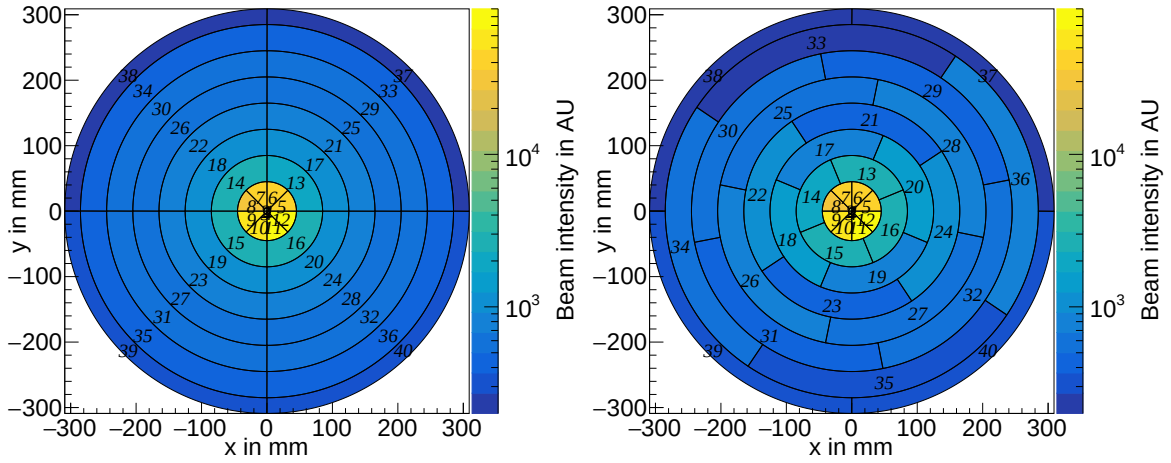

(a) Not rotated; PRM1.

(b) Rotated; PRM5.

Figure B.1: First pad plane option.

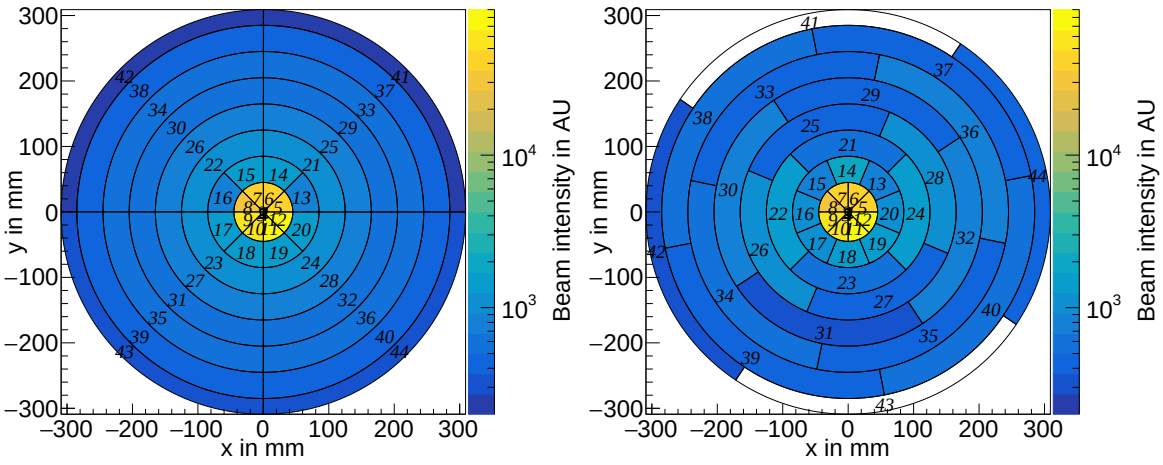

(a) Not rotated; PRM2.

(b) Rotated; PRM6.

Figure B.2: Second pad plane option.

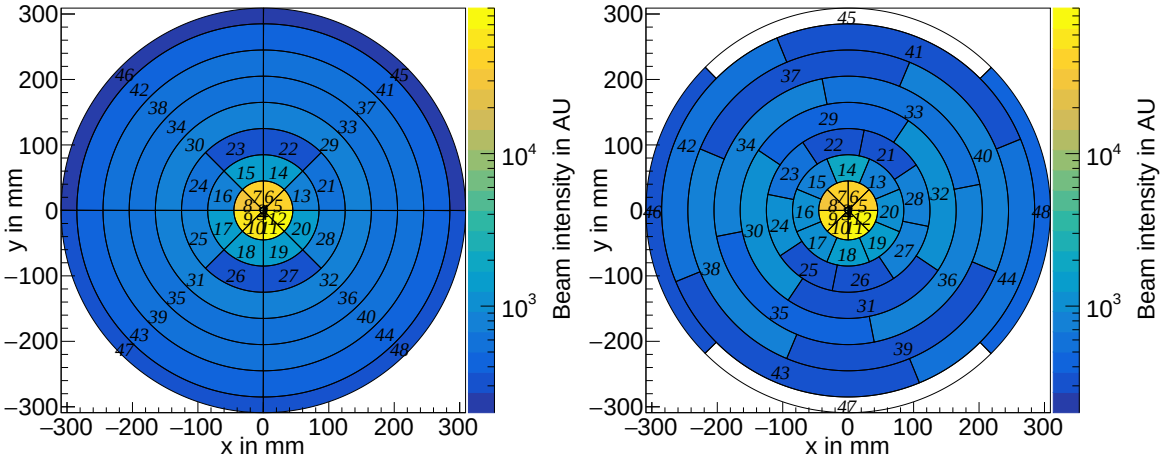

(a) Not rotated; PRM3.

(b) Rotated; PRM7.

Figure B.3: Third pad plane option.

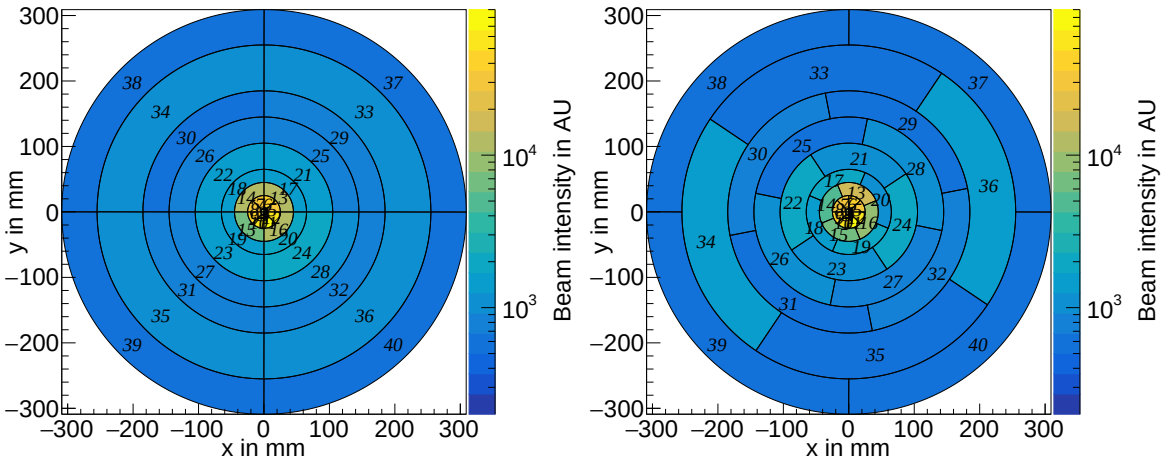

(a) Not rotated; PRM4.

(b) Rotated; PRM8.

Figure B.4: Fourth pad plane option.

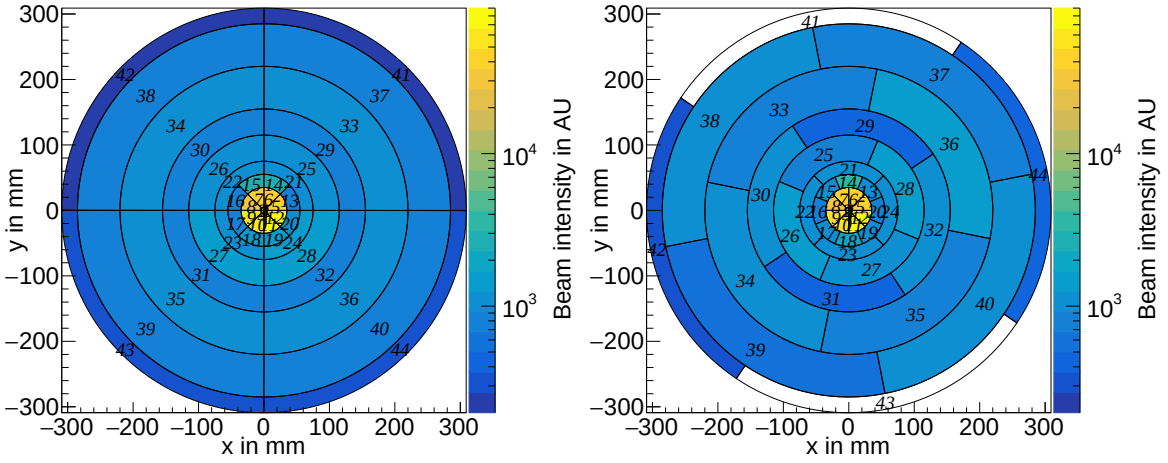

(a) Not rotated; PRM9.

(b) Rotated; PRM10.

Figure B.5: Fifth pad plane option.

APPENDIX C

Results at 4 bar

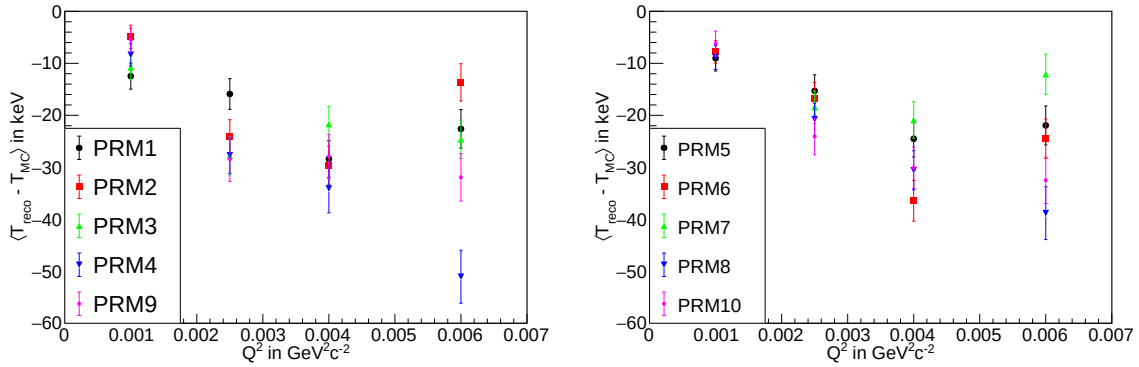

(a) Not rotated pad planes.

(b) Rotated pad planes.

Figure C.1: Mean difference between the reconstructed energy and the MC-truth value for all implemented pad planes as shown in the appendix B at 4 bar.

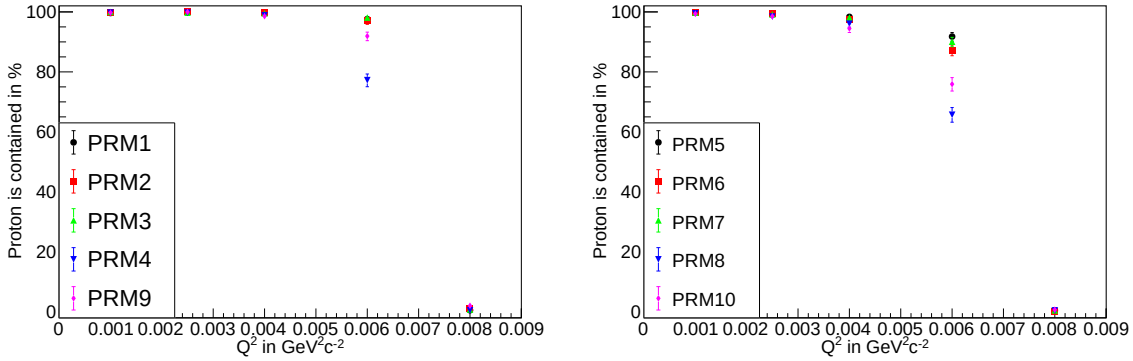

(a) Not rotated pad planes.

(b) Rotated pad planes.

Figure C.2: Fraction of events in which it is recognized that the proton has not left the TPC (no signal on the most outer ring) for all implemented pad planes as shown in the appendix B at 4 bar.

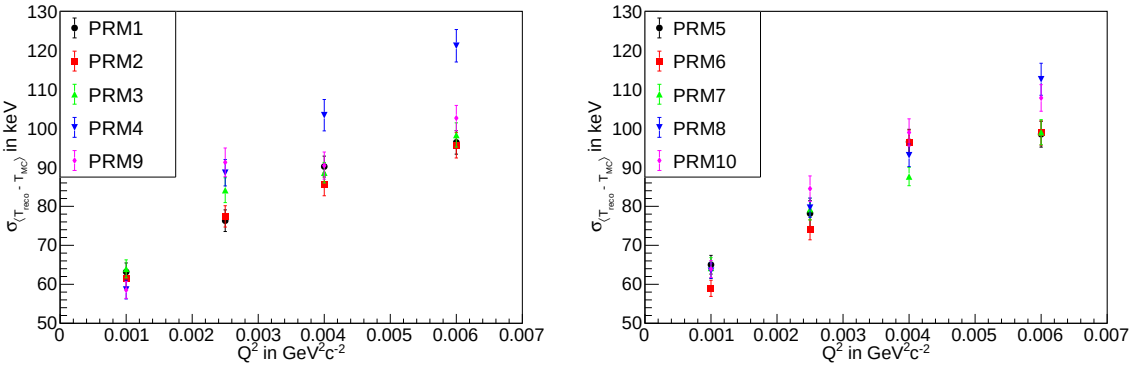

(a) Not rotated pad planes.

(b) Rotated pad planes.

Figure C.3: Standard deviation of the distributions of the difference between the reconstructed energy and the MC-truth value for all implemented pad planes as shown in the appendix B at 4 bar.

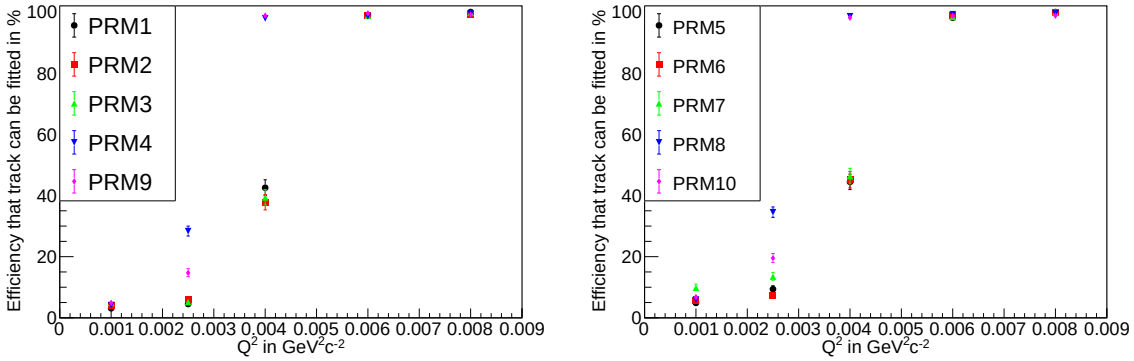

(a) Not rotated pad planes.

(b) Rotated pad planes.

Figure C.4: Fraction of events where at least three pads are included in the track and the track has been fitted for all implemented pad planes as shown in the appendix B at 4 bar.

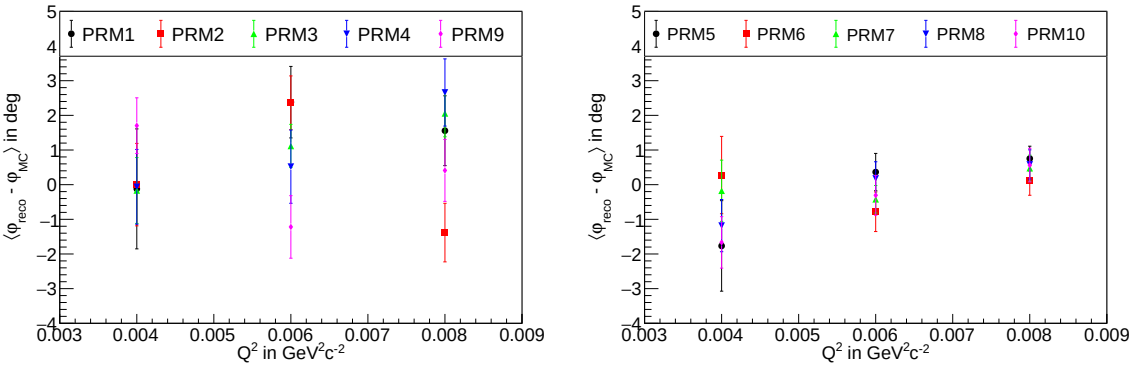

(a) Not rotated pad planes.

(b) Rotated pad planes.

Figure C.5: Mean difference between the reconstructed azimuthal angle of the proton and the MC-truth value for all implemented pad planes as shown in the appendix B at 4 bar.

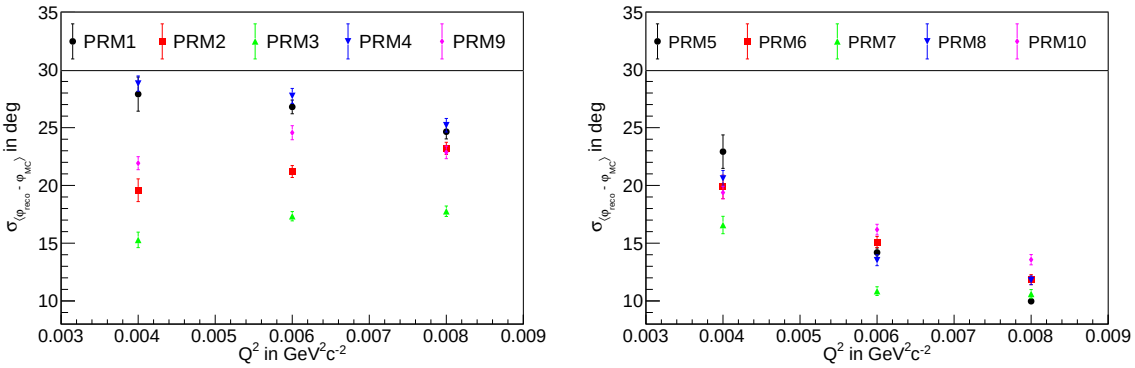

(a) Not rotated pad planes.

(b) Rotated pad planes.

Figure C.6: Standard deviation of the distributions of the difference between the reconstructed azimuthal angle of the proton and the MC-truth value for all implemented pad planes as shown in the appendix B at 4 bar.

APPENDIX D

Time cuts

Here, the time cuts are shown. The signal duration is plotted against the pad IDs of the pads that are hit by a proton in figure D.1. The corrected time difference is as well plotted against the pad IDs of the hit pads in figure D.2. The correction takes into account the distance between the different pads and therefore the time the proton travels to get to the other pad. The plots are exemplary taken for the pad plane PRM1 at 20 bar and $Q^2 = 0.01\,\mathrm{GeV}^2\,c^{-2}$. Additionally, it is required that the protons stayed inside the TPC, i.e. that no pad on the most outer ring is hit.

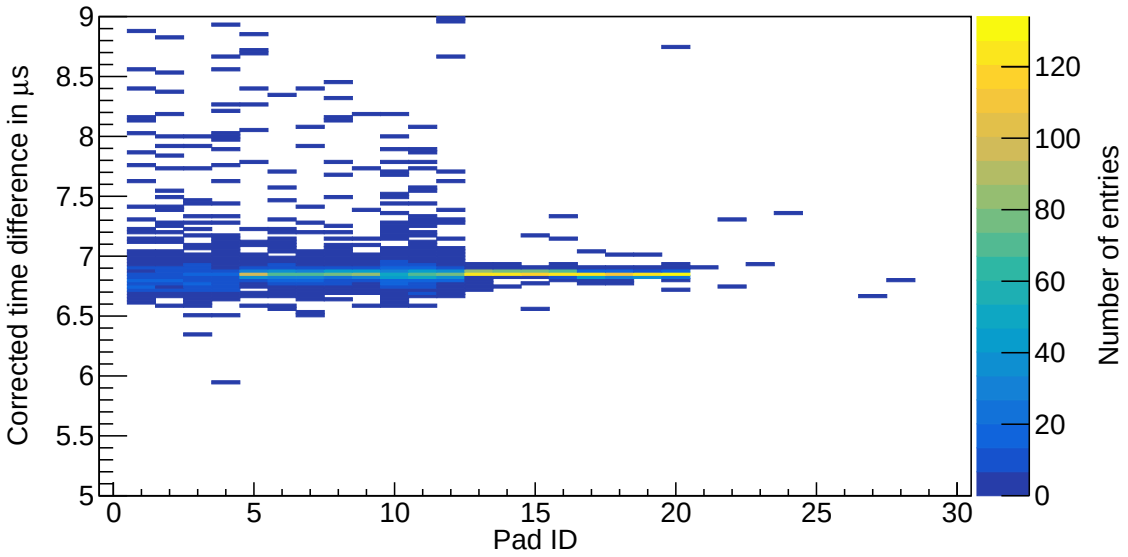

Figure D.1: Cut on the signal duration plotted against the pad ID. The duration contains the 4 µs added during the integration.

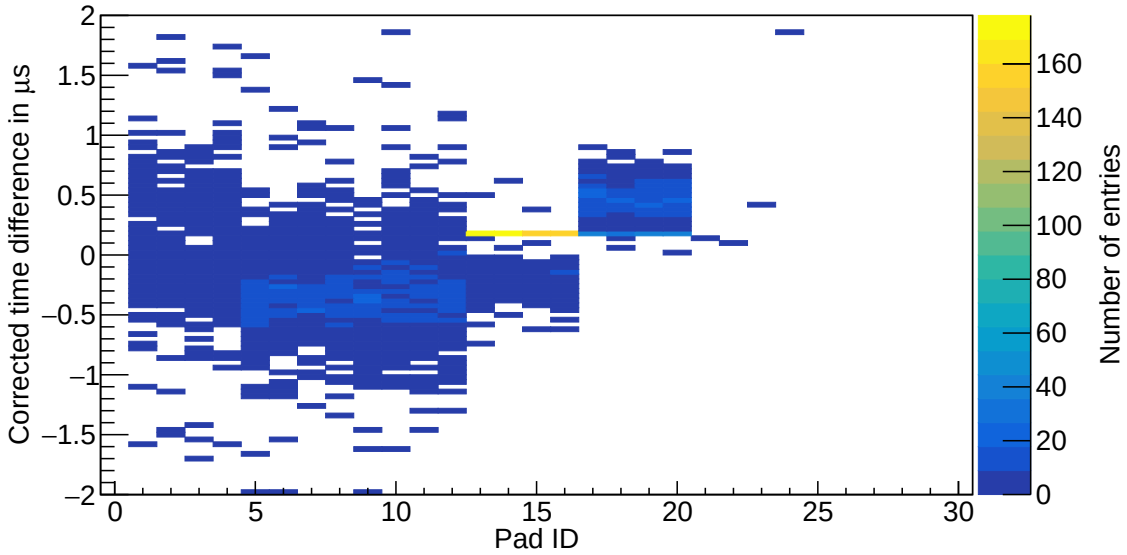

Figure D.2: Cut on the corrected time difference plotted against the pad ID.

APPENDIX E

Fit of energy-loss distributions

The energy-loss distributions of charged particles are very asymmetric as explained in section 3.1.2. A widely used model to fit these distributions is a convolution of *Landau*- and *Gauss*-distributions. The used algorithm is based on [49].

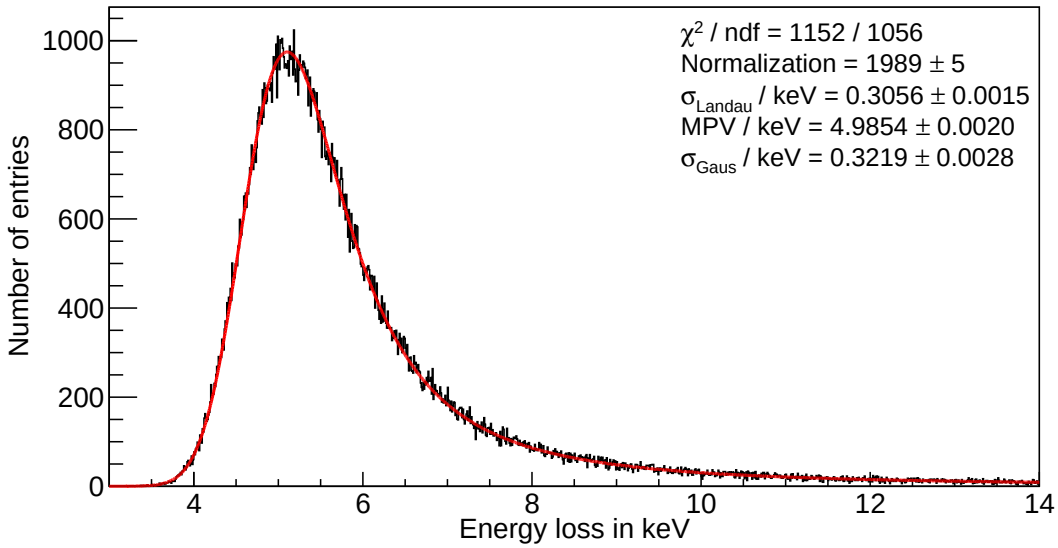

Figure E.1: Fit of the simulated energy-loss distribution for 5 GeV protons in 12 mm hydrogen gas at 20 bar. The simulation is done in GARFIELD++ based on the PAI-model.

APPENDIX F

Uniform distribution

In this chapter the standard deviation of a uniform deviation is calculated.
Such a distribution is characterized by

$$p\left(x\right) = \begin{cases} \dfrac{1}{\Delta x_0}, & \text{for } x_0 \leq x \leq x_0 + \Delta x_0 \\ 0, & \text{otherwise} \end{cases} .$$

The first central moment is calculated by

$$\left\langle x \right\rangle = \bar{x} = \int_{-\infty}^{\infty} x p\left(x\right)\, \mathrm{d}x = \int_{x_0}^{x_0+\Delta x_0} \frac{x}{x_0}\, \mathrm{d}x = x_0 + \frac{\Delta x_0}{2} .$$

The variance Var is defined as the second central moment with respect to the mean, i.e.

$$\mathrm{Var} = \left\langle \left(x - \bar{x}\right)^2 \right\rangle = \left\langle x^2 \right\rangle - \bar{x}^2 .$$

The mean for x^2 is in this case

$$\left\langle x^2 \right\rangle = \int_{-\infty}^{\infty} x^2 p\left(x\right)\, \mathrm{d}x = \int_{x_0}^{x_0+\Delta x_0} \frac{x^2}{x_0}\, \mathrm{d}x = x_0^2 + x_0 \Delta x_0 + \frac{\left(\Delta x_0\right)^2}{3} .$$

Therefore one has

$$\mathrm{Var} = \frac{\left(\Delta x_0\right)^2}{12} ,$$

and with $\sigma = \sqrt{\mathrm{Var}}$ one can finally deduce

$$\sigma = \frac{\Delta x_0}{\sqrt{12}} .$$

APPENDIX G

GARFIELD++ drift simulation

For the simulation in GARFIELD++ one needs to define the used geometry first. To extract only a few drift and diffusion parameters it is sufficient to implement a gas-based parallel plate capacitor. In the code it is written as follows:

```
SolidBox *box = new SolidBox(x0, y0, z0,
                             Lx/2.0, Ly/2.0, Lz/2.0); // in cm
```

The first three entries define the center of the box at (x_0, y_0, z_0) and the last three parameters are the lengths in the corresponding directions. There one has to be aware that the dimensions are interpreted as the half dimension. In the simulation it is chosen that the center of the box is in the origin. The lengths in x- and y-direction are $L_x = L_y = 10\,\text{cm}$. The length in z-direction is varied to extract the dependence of the parameters on the overall drifted distance.
Next, the gas needs to be defined. This is done with the MEDIUMMAGBOLTZ-class:

```
MediumMagboltz *gas = new MediumMagboltz();
gas->SetComposition("H2", 100.0);
gas->SetTemperature(temperature); // in K
gas->SetTemperature(pressure); // in Torr
gas->Initialise();
```

The temperature of the hydrogen gas is always 293.15 K and the pressure is 4 bar or 20 bar. The next step is to combine the geometry and the gas. This is done via the GEOMETRYSIMPLE-class:

```
GeometrySimple *geo = new GeometrySimple();
geo->AddSolid(box, gas);
```

With the class COMPONENTCONSTANT one is able to implement homogeneous electric and magnetic fields for the already defined geometry. The implementation looks as follows:

```
ComponentConstant *field = new ComponentConstant();
field->SetGeometry(geo);
field->SetElectricField(Ex, Ey, Ez); // in V/cm
```

Here the electric field has only a component in z-direction and depends on the pressure as can be seen in section 5.2.2 table 5.1 and section 7.2 figures 7.6 and 7.7. This field is handed over to the SENSOR which takes control of the drift later on.

```
Sensor *sensor = new Sensor();
sensor->AddComponent(field);
```

Now the implementation of the detector is finished.

To extract electron transport properties one can simply use the interface to MAGBOLTZ as shown in the following:

```
MediumMagboltz *gas = new MediumMagboltz();
gas->SetComposition(gas, 100.0);
gas->SetTemperature(temperature); // in K
gas->SetTemperature(pressure); // in Torr
gas->EnableThermalMotion(true);
gas->RunMagboltz(E, B, Lorentz_angle,
        ncoll, verbose,
        vx, vy, vz,
        longitudinal_diff, transverse_diff,
        alpha, eta, lor,
        vx_err, vy_err, vz_err,
        longitudinal_diffusion_err, transverse_diffusion_err,
        alpha_err, eta_err, lor_err,
        alphtof, difftens);
```

E is the absolute value of the electric field, B the absolute value of the magnetic field and the *Lorentz_angle* is the angle between these fields. *ncoll* is the number of collision that should be simulated to extract all properties in terms of 10^7 (with more collisions one can reach a better statistical precision). With the variable *verbose* one can activate the full output of MAGBOLTZ. *vx*, *vy* and *vz* are the velocity components of the electrons. Their longitudinal and transverse diffusion coefficients are described by *longitudinal_diff* and *transverse_diff*. *alpha* and *eta* describe the Townsend and attachment coefficient and *lor* the Lorentz angle calculated from the drift velocity components. The variables ending with *_err* are the statistical errors of all determined properties. *alphatof* is the result of a determination of the effective Townsend coefficient $\alpha - \eta$. Finally, *difftens* describes all the components of the diffusion tensor [38]. All values but the first fifth are results from the simulations from MAGBOLTZ.

APPENDIX H

ANSYS ®-script

In this chapter an ANSYS ®-script is shown to reproduce the field files needed for the calculations of the proposed anode geometry in figure 7.1 in section 7.1.

```
FINISH
/CLEAR,START
yes
/PREP7
! No polynomial elements
/PMETH,OFF,1

! Set electric preferences
KEYW,PR_ELMAG,1
KEYW,MAGELC,1

! Select element
ET,1,SOLID123

! Material properties
MP,PERX,1,1e10  ! Metal
MP,RSVX,1,0.0   !
MP,PERX,2,1.0   ! Gas
MP,PERX,3,4.0   ! Permittivity of FR4

! Define some variables
inner_pad_radius = 0.5
inner_rings_width = 4.0
outer_ring_width = 2.4
gap = 0.1
pad_thickness = 0.1
pcb_thickness = 0.5
readout_length = 1.0
wall_thickness = 0.2
gap_between_pads_and_wall = 0.1
pressure = 4.0
readout_potential = 0.0
grid_potential = -500.*readout_length*pressure+readout_potential
grid_wire_diameter = 0.1

first_ring_inner_radius = 0.0
first_ring_outer_radius = inner_pad_radius-gap
second_ring_inner_radius=first_ring_outer_radius+gap-0.5*gap
second_ring_outer_radius=second_ring_inner_radius+inner_rings_width-gap
third_ring_inner_radius=second_ring_outer_radius+gap+0.5*gap
third_ring_outer_radius=third_ring_inner_radius+inner_rings_width-gap
fourth_ring_inner_radius=third_ring_outer_radius+gap
```

```
fourth_ring_outer_radius=fourth_ring_inner_radius+inner_rings_width-gap
fifth_ring_inner_radius=fourth_ring_outer_radius+gap
fifth_ring_outer_radius=fifth_ring_inner_radius+inner_rings_width-gap
sixth_ring_inner_radius=fifth_ring_outer_radius+gap
sixth_ring_outer_radius=sixth_ring_inner_radius+inner_rings_width-gap
seventh_ring_inner_radius=sixth_ring_outer_radius+gap
seventh_ring_outer_radius=seventh_ring_inner_radius+inner_rings_width-gap
eighth_ring_inner_radius=seventh_ring_outer_radius+gap
eighth_ring_outer_radius=eighth_ring_inner_radius+inner_rings_width-gap
ninth_ring_inner_radius=eighth_ring_outer_radius+gap
ninth_ring_outer_radius=ninth_ring_inner_radius+outer_ring_width-gap

! Make the gas
WPOFFS,0,0,-readout_length/2.0-pad_thickness
CYL4,0,0,0,0,ninth_ring_outer_radius+gap_between_pads_and_wall+gap,
        90,pad_thickness+readout_length+grid_wire_diameter

! Make the grid and define it as copper
WPOFFS,0,0,readout_length+pad_thickness
CYL4,0,0,0,0,ninth_ring_outer_radius+gap,90,grid_wire_diameter
VSEL,S,,,2
VATT,1,,1
VSEL,ALL
WPOFFS,0,0,-readout_length-pad_thickness

offset=0.25*SQRT(2)*gap

! Make the pad plane (3-12)
CYL4,offset,offset,first_ring_inner_radius,0.0,first_ring_outer_radius,90.0,pad_thickness
CYL4,offset*(1.0+SQRT(2)),offset,second_ring_inner_radius,0.0,second_ring_outer_radius,
        45.0,pad_thickness
CYL4,offset,offset*(1.0+SQRT(2)),second_ring_inner_radius,45.0,second_ring_outer_radius,
        90.0,pad_thickness
CYL4,offset,offset,third_ring_inner_radius,0.0,third_ring_outer_radius,90.0,pad_thickness
CYL4,offset,offset,fourth_ring_inner_radius,0.0,fourth_ring_outer_radius,90.0,pad_thickness
CYL4,offset,offset,fifth_ring_inner_radius,0.0,fifth_ring_outer_radius,90.0,pad_thickness
CYL4,offset,offset,sixth_ring_inner_radius,0.0,sixth_ring_outer_radius,90.0,pad_thickness
CYL4,offset,offset,seventh_ring_inner_radius,0.0,seventh_ring_outer_radius,90.0,pad_thickness
CYL4,offset,offset,eighth_ring_inner_radius,0.0,eighth_ring_outer_radius,90.0,pad_thickness
CYL4,offset,offset,ninth_ring_inner_radius,0.0,ninth_ring_outer_radius,90.0,pad_thickness

! All these volumes are made out of copper
VSEL,S,,,3,12
VATT,1,,1
VSEL,ALL

! Subtract everything from the gas
VSBV,1,2,,DELETE,KEEP
VSBV,13,3,,DELETE,KEEP
VSBV,1,4,,DELETE,KEEP
VSBV,13,5,,DELETE,KEEP
VSBV,1,6,,DELETE,KEEP
VSBV,13,7,,DELETE,KEEP
VSBV,1,8,,DELETE,KEEP
VSBV,13,9,,DELETE,KEEP
VSBV,1,10,,DELETE,KEEP
VSBV,13,11,,DELETE,KEEP
VSBV,1,12,,DELETE,KEEP

! Gas is volume 13
VSEL,S,,,13
VATT,2,,1
VSEL,ALL
```

```
VGLUE,ALL

! Define the potentials of the elements
VSEL,S,,,2
ASLV,S
DA,ALL,VOLT,grid_potential
VSEL,S,,,3,12
ASLV,S
DA,ALL,VOLT,readout_potential

! Define symmetries
VSEL,S,,,13
ASLV,S
ASEL,R,LOC,X,0
DA,ALL,SYMM
VSEL,S,,,13
ASLV,S
ASEL,R,LOC,Y,0
DA,ALL,SYMM

VSEL,S,,,2,13
ASLV,S
MSHKEY,0
SMRT,1
VSEL,S,,,13
VMESH,ALL

/SOLU
SOLVE
yes
FINISH

! Write the solution to files
/OUTPUT, PRNSOL, lis
PRNSOL
/OUTPUT
/OUTPUT, NLIST, lis
NLIST,,,,COORD
/OUTPUT
/OUTPUT, ELIST, lis
ELIST
/OUTPUT
/OUTPUT, MPLIST, lis
MPLIST
/OUTPUT
```

List of Figures

List of Tables